Technical Assistance for the validation of the ENVISAT MGVI geophysical product

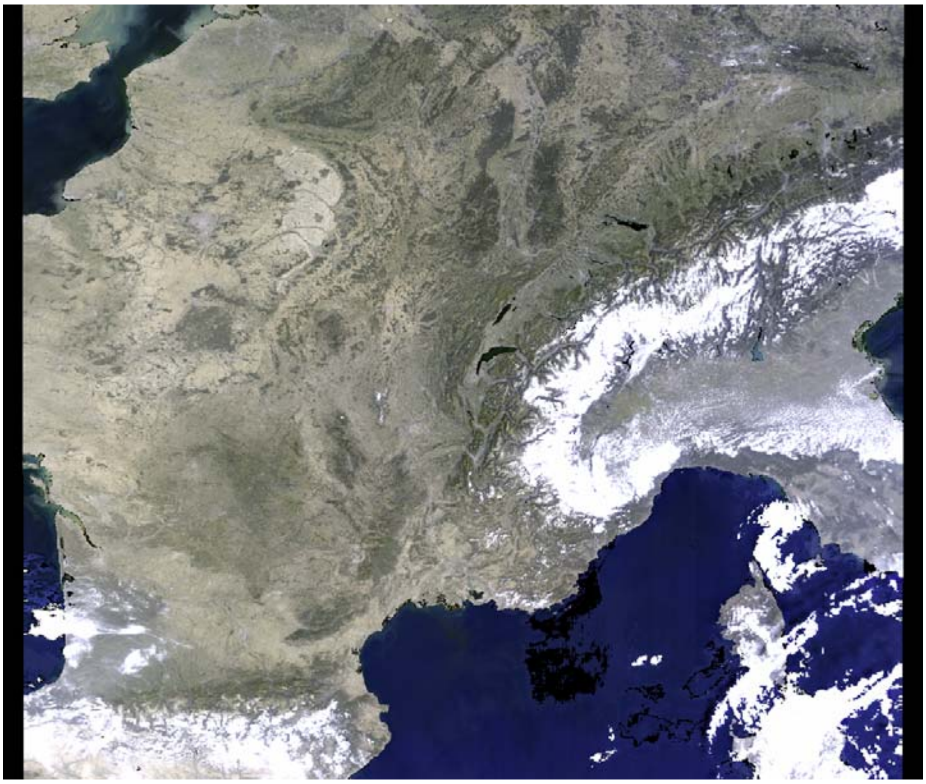

Work Package 6300 'ESTEC Contract 18446/04/NL/CB'

N. Gobron, O. Aussedat, B. Pinty, M. Robustelli, M. Taberner and T. Lavergne

European Commission – DG Joint Research Centre,
Institute for Environment and Sustainability, Global Environment Monitoring Unit
TP 440 via E. Fermi, 1
I-21020 Ispra (VA), Italy

June 2006 **EUR 22246 EN**

The mission of the Institute for Environment and Sustainability is to provide scientific and technical support to the European Union’s policies for protecting the environment and the EU Strategy for Sustainable Development.

European Commission Directorate-General Joint Research Centre
Institute for Environment and Sustainability

http://ies.jrc.cec.eu.int
http://www.jrc.cec.eu.int

EUR 22246 EN Luxembourg: Office for Official Publications of the European Communities

Printed in Italy

This document presents the final results of the 'ESTEC Contract 18446/04/NL/CB' entitled '**Technical Assistance for the validation of the ENVISAT MGVI geophysical product**' and constitutes the deliverable of Work Package (WP) 6300.

1. Outline of the project

The Medium Resolution Imaging Spectrometer (MERIS) Global Vegetation Index (MGVI) has been optimized to generate numerical values between 0 and 1 representative of the Fraction of Absorbed Photosynthetically Active Radiation (FAPAR) of the vegetation over terrestrial surfaces [1][2]. This bio-geophysical variable plays a critical role in the photosynthetic process and is regularly used in diagnostic and predictive models to compute the primary productivity of the plant cover.

This project aims to assess the accuracy and the quality of the MGVI product by comparing this operational Level-2 geophysical product to similar ones generated by other independent sensors co-located and quasi simultaneously acquired data. These comparisons mainly concerns the MERIS Level-2 products generated at reduced spatial resolution,
(http://envisat.esa.int/dataproducts/meris/CNTR6-1-3.htm#eph.meris.merisdf.2p.MER_RR__2P).

2. Introduction

MGVI values can be compared to similar products derived from other sensors [3], using similar but independent algorithms to derive the same FAPAR information.

This document constitutes the final report to overview the results of FAPAR comparison between a set of instruments which includes MERIS, SeaWiFS, MODIS, MISR and MOS:

- Sea-viewing Wide Field-of-view Sensor (SeaWiFS)/NASA on board the OrbView platform, operational since October 1997, with a nominal spatial resolution at nadir of 1100 m (http://oceancolor.gsfc.nasa.gov/SeaWiFS/).

- MODerate resolution Imaging Spectro-radiometer (MODIS)/NASA on board both the Terra and Aqua platforms, operational since February 2000 for Terra and since July 2002 for Aqua, with a nominal spatial resolution at nadir of 250 m, 500 m and 1100 m depending on spectral bands (http://modis.gsfc.nasa.gov/).

- Multi-angle Imaging Spectro-Radiometer (MISR)/JPL on board the Terra platform, operational since February 2000, with a nominal spatial resolution at nadir of 275 m and 1100 m depending on spectral bands (http://www-misr.jpl.nasa.gov/).

- Modular Optoelectronic Scanner (MOS)/DLR on board IRS-P3 platform, operational from 1996 to 2000 with a nominal spatial resolution at nadir of 500 m (http://earth.esa.int/services/pg/pgip3mosl1b.xml).

The following instruments were not used in this project but may be added in further analysis:

- The GLobal Imager (GLI)/JAXA instrument could not be considered at this stage because the top of atmosphere data are not publicly available (http://suzaku.eorc.jaxa.jp/GLI/).

- The VEGETATION P-products, i.e. the top of atmosphere data, were not available in due time, i.e. before the end of this project (http://www.spot-vegetation.com/).

Similar to MERIS, FAPAR algorithms have been optimized for SeaWiFS [4], MISR [5][6] and GLI [7] and in the context of this project we designed a specific one for MODIS (WP 3000) [8].

Section 3 overviews the status of each work package defining specific steps to achieve the deliverables.

Section 4 presents a summary of the generic methodology and the results of JRC-FAPAR optimization for various optical instruments used in this document. We also present a theoretical analysis of the propagation of errors, i.e. the absolute accuracy of FAPAR as function of the various uncertainties of the three spectral reflectances used in the algorithm.

A processing chain has also been designed and developed in order to read, remap various remote sensing data to derive FAPAR products. In the context of comparison of long time-series, we develop time-composite software codes for MERIS and MODIS instruments based on the technique described in [9] (see section 5 p. 23). (The outputs of MERIS Level 3 based on the Reduce Resolution Level 2 data are described in [10]).

In order to carry out the comparison, it is critical to acquire cloud-free remote sensing observations for the same place and (at least approximately) for the same time from different space-borne instruments. Section 6 and 7 summarize the data which have been used. They have been classified into various components from daily data over small regions (instantaneous) to 10-day or monthly composite over Europe. We also initiated to compare the products against ground-estimations over a few Earth Observing System (EOS) validation sites.

The figures of results are mainly presented in Annexes and the analysis is summarized in section 8.

3. Work Packages

The following Work Packages (WP) describe the different steps that have been made to achieve the deliverables.

- **Data acquisition**
  - WP 1100- Extraction of common geographical zone between MERIS and SeaWiFS products.
    - New reprocessed MERIS Level-2 products have been downloaded from the MERCI system (http://www.brockmann-consult.de/MERCI/index.htm) developed by Brockmann's Consult.
    - Grid On-demand service (http://eogrid.esrin.esa.int/) has been used to produce monthly composite over Europe.
  - WP 1200- Data survey for identification of quasi-simultaneous cloud free data over same regions from MODIS and MISR sensors.

  - WP 1300- Data acquisition MODIS and MISR
    - The Terra/MODIS data have been downloaded from Earth Observing System (EOS) data gateway (http://edg.larc.nasa.gov/~imswww/imswelcome/). The version 5 of MODIS radiances has been used when available.
    - The Terra/MISR data have been downloaded from Earth Observing System (EOS) data gateway (http://edg.larc.nasa.gov/~imswww/imswelcome/) only over one particular site (Bondville, USA) because the large amount of space disk associated to MISR data was a technical issue.

  - WP 1400: Data survey for identification of quasi-simultaneous cloud free data over same regions from VEGETATION/SPOT, GLobal Imager (GLI) and Modular Optoelectronic Scanner (MOS)-B/IRS-P3.
    - The GLI data could not be considered at this stage because the top of atmosphere data are not publicly available.
    - The VEGETATION P-products can not be available in due time, i.e. before end of this project.

  - WP 1500: Data acquisition (MOS)
    - Various MOS-B data have been downloaded via ftp from the Deutschen Zentrum für Luft- und Raumfahrt (DLR) portal: http://eoweb.dlr.de:8080/servlets/template/welcome/entryPage.vm over few particular regions.

- **Development of software codes for reading data**
  - WP 2100
    - A routine has been added in the JRC remap software for daily Level 1 MERIS RR and FR.
    - A processing chain to operationally read and remap MODIS Level 1 data and compute the FAPAR has been designed and developed.
    - A routine has been added in the JRC remap software for daily Level 2 MERIS RR and FR and JRC-FAPAR MODIS Level 2.

  - WP 2200
    - A processing chain to operationally read and remap MOS-B data and compute the FAPAR has been designed and developed.
    - An IDL code for R&D has been updated for reading the new version of MISR Level 1 data (radiances) to process the data and compute FAPAR products.

- **Development of software code for the optimal FAPAR index**
  - WP 3100- Implementation of spectral characteristics of MODIS in the FACOSI tool.
  - WP 3200- Generation of Lookup Table.
  - WP 3300-
    - Optimization of the MODIS FAPAR index
    - Code for producing FAPAR products
    - Algorithm Theoretical Basis document (ATBd) is published in [8]
  - WP 3400: Update of the IDL FAPAR code for MISR

- **Data Processing**: Apply JRC-FAPAR algorithm to the Level 1 data (other than MERIS) to generate comparable Level 2 products (including re-projection on a common grid).

    - WP 4100-4200 and 4300: Data over the case studies described in the Table 7, Table 8 and Table 9 have been processed at the JRC for various instruments.

- **WP 5000: Statistical analysis** for comparing the products over the same areas and time periods (Perl scripts and IDL codes have been developed to perform this task).
    - WP 5100- The scatter plots and histograms for comparison between FAPAR derived from **MERIS using the first (MEGS-PC/6.1) and newly reprocessed (MEGS-PC/7.4) data** and SeaWiFS have been updated by remapping all data in a rectangular projection at about 1.2 km.
    - The scatter plots and histograms for comparison between monthly FAPAR derived from MERIS and SeaWiFS were produced after remapping or aggregating in the Lambert Azimuth Equal Area projection over European continent for the entire year 2003 and against MODIS product for April.
    - WP 5200-5300 Comparisons using MERIS, SeaWiFS, MODIS, MOS and MISR data and products have been achieved against ground-based estimations of FAPAR over various EOS validation sites.

- **WP 6000: Deliverables**
    - WP 6100- First report within two months of contract signature.
    - WP 6200- A mid report on the methodology and results of all comparisons between MERIS and Sensor Group 1 for which appropriate data have been collected.
    - WP 6300- A final report on the methodology and results of all comparisons between MERIS and other sensors for which appropriate data will have been collected by the end of the proposal.
    - WP 6400 – Prepare a short document suitable for publication on the ESA web site to outline the aims, approach and outcome of the project.

4. JRC-FAPAR algorithm

a. Overview of Design

The generic JRC-FAPAR algorithm aims to derive biophysical indicator from spectral space data, without *any a priori knowledge on the land cover*, in order to assess the state and health of vegetation surfaces. The products are derived using a physically-based algorithm which has been developed for various optical sensors. This section summarizes the methodology which has been used to derive the FAPAR values from various optical sensor data.

MGVI-type algorithm can be adapted to any sensor acquiring at least three spectral bands in the blue, red and near-infrared regions of the solar spectrum. This algorithm capitalizes on the physics of remote sensing measurements and its development copes with the many operational constraints associated with the systematic processing and analysis of a large amount of data. Basically, the useful information on the presence and state of vegetation is derived from the red and the near-infrared spectral band measurements. The information contained in the blue spectral band, which is very sensitive to aerosol load, is ingested in order to account for atmospheric effects on these measurements. Our original approach thus consists in analyzing the relationships between measurements in the blue spectral band and those available in the red and near-infrared regions [1][2][3]. Such relationships can indeed be simulated for a variety of environmental conditions with radiation transfer models of the coupled vegetation-atmosphere system. The former are then exploited with polynomial expressions optimized in such a way that top of atmosphere Bidirectional Reflectance Factor (BRF) measurements in the blue are related to those taken at other spectral bands, located at longer wavelengths e.g., in the red and near-infrared regions. This approach aims at decontaminating the BRF from atmospheric effects without performing an explicit retrieval of the ambient atmospheric properties. The polynomial expressions are also built to simultaneously account for the bulk of the anisotropy effects. The latter are themselves approximated from an extensive set of radiation transfer simulations of the coupled surface-atmosphere system designed for mimicking typical vegetation canopy conditions. This same training data set is then used to relate the spectral measurements from each typical vegetation canopy condition to their corresponding FAPAR values. In practice, the generic FAPAR algorithm thus implements a two-step procedure where the spectral BRFs measured in the red and near-infrared bands are, first, rectified in order to ensure their optimal decontamination from atmospheric and angular effects and, second, combined together to estimate at best the instantaneous FAPAR value at the time of acquisition. The most recent versions of the appropriate formulae and coefficients derived from the mathematical optimization are published in [12] for SeaWiFS, [13] for MERIS and [5][6] for MISR, respectively and are summarized below.

The Figure 1 shows the spectral characteristic in the blue, red and near-infrared domains for MERIS (full color), SeaWiFS (\\\), MODIS (///) and MISR (light color) for which the comparisons have been conducted. MOS spectral bands (Blue: 0.4405-0.4455 nm; Red: 0.6825-0.6875 nm; NIR: 0.8675-0.8725 nm) are close enough to the MERIS ones (Blue: 0.442 nm; Red: 0.684 nm; NIR: 0.865 nm) for that we assume that the MGVI can be applied directly to this instrument.

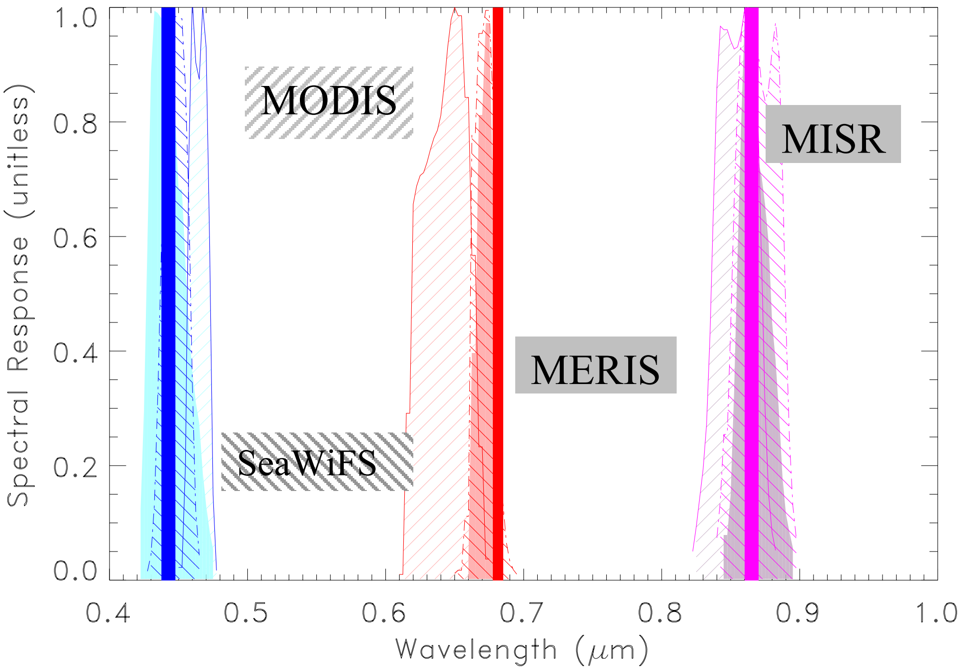

Figure 1 Spectral Response in blue, red and near-infrared bands for SeaWiFS; MODIS/Terra; MERIS and MISR

b. Results for MODIS

The MODIS data have been simulated using the spectral response of ‘land spectral bands’, i.e. (Band 1, Band 2 and Band 3). (Note: The actual red and near-infrared data correspond to a resolution at 250 m whereas the blue band one is at 500 m. In the following, we used the MOD21km radiance data which contain spectral values, illumination and observation geometries aggregated at 1 km.)

Figure 2 illustrates the impact of the ‘rectification’ procedure, which combines Top Of Atmosphere (TOA) reflectances in the blue band with TOA reflectances in the red and near-infrared bands, respectively. The left panels show the relationships between the spectral BRFs Top Of Canopy (TOC) normalized by the anisotropic function F (x-axis), and BRFs TOA for all geophysical and angular scenarios used in the training datasets (y-axis). The scatter of the points is caused by changes in the atmospheric conditions and by the relative geometry of illumination and observation. The right panels show the effect of the ‘rectification’ process, which reduces this dispersion. A perfect ‘rectification’ would collapse all points on the 1:1 line for each of the surface types considered. It can be seen that this process is particularly efficient over dense vegetation (blue to green points), and that it reduces the systematic bias due to atmospheric and angular effects in both bands.

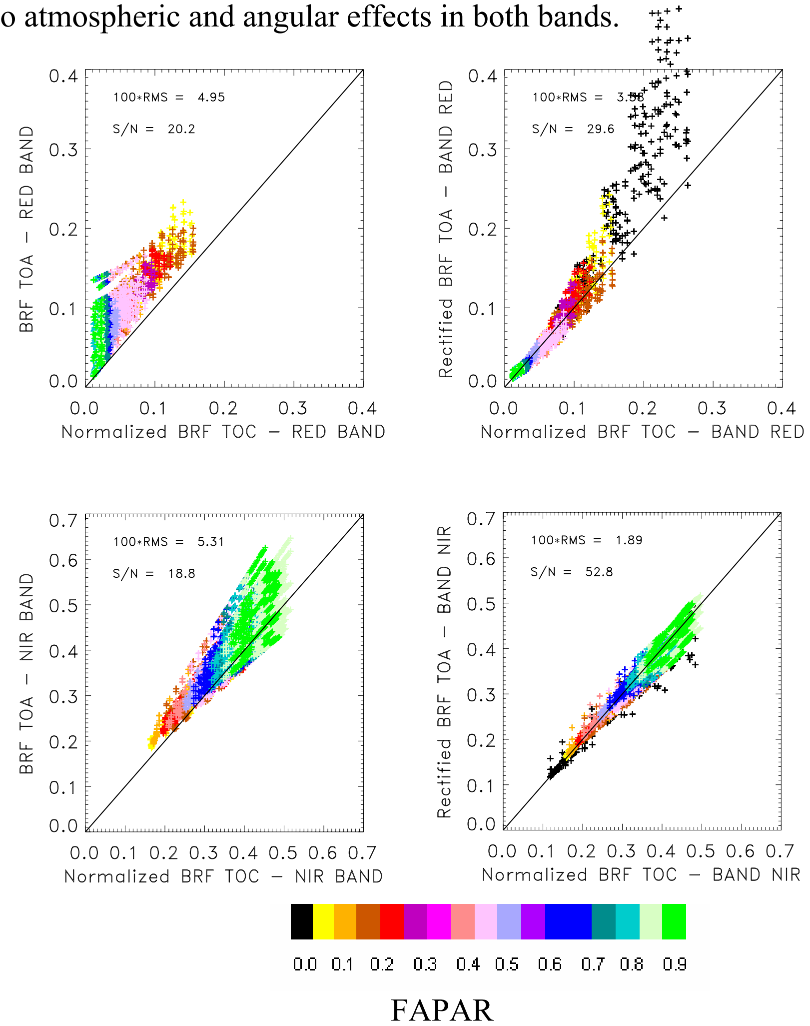

Figure 2: Left panels: relationship between the BRFs TOC normalized by the anisotropic function F, and BRFs TOA, for all conditions of the LUT, in the red (top) and near-infrared (bottom) band. Right panels: relationship between the ‘rectified’ reflectances and the corresponding BRFs TOC normalized by the anisotropic function F. The various colors represent different values of FAPAR for the plant canopies.

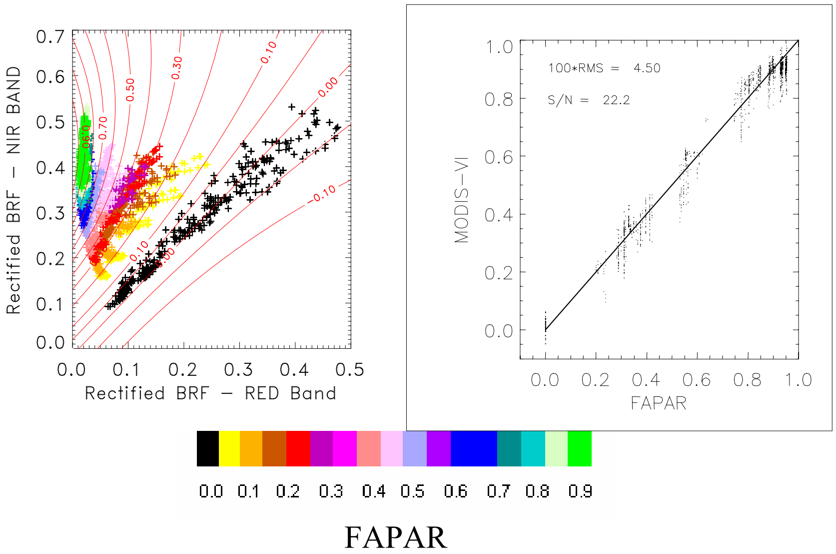

Figure 3: The left panel shows the iso-lines of polynomial g_0 in the red-NIR spectral space together with the rectified channels. The right panel shows the relationship between the simulated (using RT model) and derived FAPAR values.

Figure 3 provides information on the performance of JRC-FAPAR MODIS: The left panel shows the isolines of the polynomial formulae of FAPAR in the spectral space of the red and near-infrared rectified bands. It can be seen that the FAPAR derived from our algorithm varies between 0 and 1 over partially and fully vegetated surfaces and takes negative values out of the spectral domain of interest. Operationally, a mask is applied using spectral thresholds for computing the algorithm over only the vegetated pixels. The right panel of the same figure shows that the product is close to the simulated FAPAR with a root mean square deviation equal to 0.045. Most of the remaining variability between simulated and derived JRC-FAPAR MODIS is probably caused by the various conditions that were considered in the geophysical scenarios. In fact, this variability results from conflicting requirements on the insensitivity of the algorithm to soil, atmospheric and geometrical effects in the MODIS spectral bands.

c. JRC-FAPAR Formulae

The top of atmosphere (TOA) channel values are first normalized by the anisotropy function F to take into account the angular effects using "related band sensor" coefficients given in Table 1.

$$\tilde{\rho}(\lambda_i) = \frac{\rho^{toa}(\Omega_0, \Omega_v, \lambda_i)}{F(\Omega_0, \Omega_v, k_{\lambda i}, \Theta^{HG}_{\lambda i}, \rho_{\lambda ic})}$$

The rectification process of the red and near-infrared bands is performed as follows:

$$\rho_{Rred} = g_1[\tilde{\rho}(\lambda_{blu}), \tilde{\rho}(\lambda_{red})] \qquad \rho_{Rnir} = g_2[\tilde{\rho}(\lambda_{blu}), \tilde{\rho}(\lambda_{nir})]$$

where

$$g_n[\tilde{\rho}(\lambda_i),\tilde{\rho}(\lambda_j)] = P(\lambda_i,\lambda_j)/Q(\lambda_i,\lambda_j)$$

$$P(\lambda_i,\lambda_j) = l_{n1}(\tilde{\rho}(\lambda_i)+l_{n2})^2 + l_{n3}(\tilde{\rho}(\lambda_j)+l_{n4})^2 + l_{n5}\,\tilde{\rho}(\lambda_i)\tilde{\rho}(\lambda_j)$$

$$Q(\lambda_i,\lambda_j) = l_{n6}(\tilde{\rho}(\lambda_i)+l_{n7})^2 + l_{n8}(\tilde{\rho}(\lambda_j)+l_{n9})^2 + l_{n10}\,\tilde{\rho}(\lambda_i)\tilde{\rho}(\lambda_j) + l_{n11}$$

using the optimized coefficients reported in Table 2.

JRC- FAPAR is computed by the following formulae with coefficients reported in Table 3.

$$\text{FAPAR} = g_0(\rho_{Rred},\rho_{Rnir}) = \frac{l_{01}\rho_{Rnir} - l_{02}\rho_{Rred} - l_{03}}{(l_{04}-\rho_{Rred})^2 + (l_{05}-\rho_{Rnir})^2 + l_{06}}$$

Table 1: Optimized Values of the anisotropic function F of RPV model at TOA [14]

Spectral Domain	Sensor	**Bandwidth/ central wavelength**	$\rho_{\lambda ic}$	$k_{\lambda i}$	$\Theta^{HG}_{\lambda i}$
BLUE	**MODIS**	459-479 nm	**0.13704**	**0.56177**	**-0.03204**
	MERIS	442 nm	**0.24012**	**0.56192**	**-0.04203**
	SeaWiFS	443 nm	**0.23265**	**0.56184**	**-0.04125**
	MISR(*)	446 nm	**0.35908**	**0.47372**	**-0.03596**
RED	**MODIS**	620-670 nm	**-0.39924**	**0.70116**	**0.03376**
	MERIS	681 nm	**-0.46273**	**0.70879**	**0.037**
	SeaWiFS	678 nm	**-0.44444**	**0.70535**	**0.03576**
	MISR(*)	672 nm	**0.26840**	**0.82270**	**0.03350**
NIR	**MODIS**	841-876 nm	**0.63537**	**0.70116**	**0.03376**
	MERIS	865 nm	**0.63841**	**0.86523**	**-0.00123**
	SeaWiFS	865 nm	**0.63149**	**0.86523**	**-0.00102**
	MISR(*)	867 nm	**0.71588**	**0.88483**	**-0.01556**

(*) Using only the camera at nadir view.

Table 2: Optimized coefficients for the rectification polynomial formulae.

Optimized coefficients for g_1					
Sensor	l_{10}	l_{11}	l_{12}	l_{13}	l_{14}
MODIS	-13.860	-0.018273	1.5824	0.081450	17.092
MERIS	-9.2315	-0.029011	3.2545	0.055845	9.8268
SeaWiFS	-9.8725	-0.027458	2.9144	0.059376	10.904
MISR	0.59579	4.4888	-20.902	0.75360	95.944
	l_{15}	l_{16}	l_{17}	l_{18}	l_{19}
MISR	-0.25525	14.319	191.81	-0.45995	1081.6

Optimized coefficients for g_2					
Sensor	l_{20}	l_{21}	l_{22}	l_{23}	l_{24}
MODIS	-0.036557	-3.5399	8.3076	0.18702	-13.294
MERIS	-0.47131	-0.21018	-0.045159	0.076505	-0.80707
SeaWiFS	-0.66956	-0.16930	-0.072156	-0.090485	-0.81353
MISR	11.724	-0.11896	0.74257	0.16564	4.6009
Sensor	l_{25}	l_{26}	l_{27}	l_{28}	l_{29}
MODIS	0.77034	-4.9048	-2.3630	-2.6733	-37.297
MERIS	-1.2471	-0.54507	-0.47602	-1.1027	0.0
SeaWiFS	-0.035440	-1.3438	-0.41673	-0.45123	-0.99648

Table 3: Optimized coefficients for the FAPAR polynomial formulae

Optimized Coefficients for g_0						
Sensor	l_{00}	l_{01}	l_{02}	l_{03}	l_{04}	l_{05}
MODIS	0.26130709	0.33489629	-0.0038298022	-0.32136740	0.31415914	-0.010744180
MERIS	0.255	0.306	-0.0045	-0.32	0.32	-0.005
SeaWiFS	0.25130709	0.30589629	-0.0048298022	-0.3213674	0.31415914	-0.01074418
MISR	0.33729	0.32529	0.0064192	-0.18673	0.28355	0.078834

d. Assessment of the accuracy from FAPAR formulae from uncertainties in the inputs (NEW)

The JRC-FAPAR products are computed from three spectral bands in the blue, red and near-infrared domains. The FAPAR uncertainty can be assessed by mathematically differentiate the formulae with respect to theoretical calibration accuracies.

$$\Delta \mathrm{FAPAR} = \frac{\partial \mathrm{FAPAR}}{\partial \rho_{\mathrm{BLUE}}} \Delta \rho_{\mathrm{BLUE}} + \frac{\partial \mathrm{FAPAR}}{\partial \rho_{\mathrm{RED}}} \Delta \rho_{\mathrm{RED}} + \frac{\partial \mathrm{FAPAR}}{\partial \rho_{\mathrm{NIR}}} \Delta \rho_{\mathrm{NIR}}$$

where $\Delta\rho_{\lambda}$ is the absolute accuracy of the bidirectional reflectances (BRF) at the top of the atmosphere for each band λ

An IDL code has been developed to compute $\Delta \mathrm{FAPAR}$ as function of the BRF triplet

$$(\rho_{\mathrm{BLUE}} \pm \Delta\rho_{\mathrm{BLUE},} \rho_{\mathrm{RED}} \pm \Delta\rho_{\mathrm{RED},} \rho_{\mathrm{NIR}} \pm \Delta\rho_{\mathrm{NIR}})$$

The derivative of FAPAR formulae can be re-written as follow:

$$\Delta \mathrm{FAPAR} = \Delta g_0 = \frac{\partial g_0}{\partial \rho_{\mathrm{RectRED}}} \Delta\rho_{\mathrm{RectRED}} + \frac{\partial g_o}{\partial \rho_{\mathrm{RectNIR}}} \Delta\rho_{\mathrm{RectNIR}}$$

where the uncertainties of each rectified channel are:

$$\Delta\rho_{\mathrm{RectRED}} = \frac{\partial g_1}{\partial \rho_{\mathrm{BLUE}}} \Delta\rho_{\mathrm{BLUE}} + \frac{\partial g_1}{\partial \rho_{\mathrm{RED}}} \Delta\rho_{\mathrm{RED}}$$
$$\Delta\rho_{\mathrm{RectNIR}} = \frac{\partial g_2}{\partial \rho_{\mathrm{BLUE}}} \Delta\rho_{\mathrm{BLUE}} + \frac{\partial g_2}{\partial \rho_{\mathrm{RED}}} \Delta\rho_{\mathrm{RED}}$$

The formula for the derivative of g_0 with respect to the rectified red channel is given by the following equation:

$$\frac{\partial g_0}{\partial \rho_{\mathrm{RectRED}}} = \frac{2(l_{04} - \rho_{\mathrm{RectRed}})(-l_{02}\rho_{\mathrm{RectRed}} + l_{01}\rho_{\mathrm{RectNIR}} - l_{03})}{((l_{04} - \rho_{\mathrm{RectRed}})^2 + (l_{05} - \rho_{\mathrm{RectNIR}})^2 + l_{06})^2} - \frac{l_{02}}{(l_{04} - \rho_{\mathrm{RectRed}})^2 + (l_{05} - \rho_{\mathrm{RectNIR}})^2 + l_{06}}$$

and the formula for the derivative of g0 with respect to the rectified NIR channel by this one:

$$\frac{\partial g_0}{\partial \rho_{\mathrm{RectNIR}}} = \frac{2(l_{05} - \rho_{\mathrm{RectNIR}})(-l_{02}\rho_{\mathrm{RectRed}} + l_{01}\rho_{\mathrm{RectNIR}} - l_{03})}{((l_{04} - \rho_{\mathrm{RectRed}})^2 + (l_{05} - \rho_{\mathrm{RectNIR}})^2 + l_{06})^2} - \frac{l_{01}}{(l_{04} - \rho_{\mathrm{RectRed}})^2 + (l_{05} - \rho_{\mathrm{RectNIR}})^2 + l_{06}}$$

The derivatives formulae of g_1 and g_2 are the following:

$$\frac{\partial g_n}{\partial \rho_1} = \frac{\rho_2 l_{n5} + 2l_{n1}(l_{n2} + \rho_1)}{l_{n8}(l_{n9} + \rho_2)^2 + l_{n6}(l_{n7} + \rho_1)^2 + l_{n11} + \rho_1\rho_2 l_{n10}} - \frac{\left(\rho_1\rho_2 l_{n5} + l_{n3}(l_{n4} + \rho_2)^2 + l_{n1}(l_{n2} + \rho_1)^2\right)\left(2l_{n6}(l_{n7} + \rho_1) + \rho_2 l_{n10}\right)}{\left(l_{n8}(l_{n9} + \rho_2)^2 + l_{n6}(l_{n7} + \rho_1)^2 + l_{n11} + \rho_1\rho_2 l_{n10}\right)^2}$$

$$\frac{\partial g_n}{\partial \rho_2} = \frac{\rho_1 l_{n5} + 2 l_{n3}(l_{n4} + \rho_2)}{l_{n8}(l_{n9} + \rho_2)^2 + l_{n6}(l_{n7} + \rho_1)^2 + l_{n11} + \rho_1\rho_2 l_{n10}} - \frac{\left(\rho_1\rho_2 l_{n5} + l_{n3}(l_{n4} + \rho_2)^2 + l_{n1}(l_{n2} + \rho_1)^2\right)\left(2 l_{n8}(l_{n9} + \rho_2) + \rho_1 l_{n10}\right)}{\left(l_{n8}(l_{n9} + \rho_2)^2 + l_{n6}(l_{n7} + \rho_1)^2 + l_{n11} + \rho_1\rho_2 l_{n10}\right)^2}$$

The **BRFs TOA simulated by the radiative transfer models**, which have been used in the optimization itself, permit us to estimate the uncertainties of FAPAR using the equations above, as well as the differences between two JRC-FAPAR products derived from two sensors as function of each spectral band calibration error. The following summarizes the analysis which has been made for MERIS:

- ***Absolute accuracy of FAPAR as a function of spectral calibration in the three MERIS bands***.

Figure 4 illustrates how the absolute deviations of FAPAR, ΔFAPAR vary in the 3D spectral space of band uncertainties. Each panel corresponds to one uncertainty value in the blue band. The values which are mapped in the space ($\Delta\rho_{RED}$, $\Delta\rho_{NIR}$) correspond to the ΔFAPAR averaged over all simulated MERIS like data. Among all the results, however, large differences occur in the results depending on both atmospheric and angular situations. The panels in Figure 5 show this range of ΔFAPAR when the uncertainties of at least two bands of MERIS, $\Delta\rho_\lambda$, increase from 0 % to 10 % as a function of a third band uncertainty (6 panels correspond to 6 values of %). The top left panel, for example, illustrates how, on average, ΔFAPAR varies as function of the uncertainties of the blue band (blue color), the red band (red) and the near-infrared band (purple) when the two others are 'perfect'. The error bar indicates the minimum and maximum values obtained with the training data set we used. The largest uncertainties of the three spectral bands are, the largest the uncertainties in FAPAR are: this theoretically demonstrates how the calibration issues are important to assess the quality of the product.

The results assess that the averaged value, **ΔFAPAR, can be higher than 0.1 when 2 bands have uncertainty values of about 4-5 % (as example of maximum value that can be operationally expected in the spectral uncertainties)**. The blue band has more impact than the red and near-infrared bands for low values of uncertainties (i.e., ΔFAPAR ≈ 0.1 if $\Delta\rho_{BLUE} > 6$ % and $\Delta\rho_{RED} = \Delta\rho_{NIR} =$ 2 %). This result is easily explained by the fact that we used the blue bands twice in our algorithm to remove the atmospheric effects.

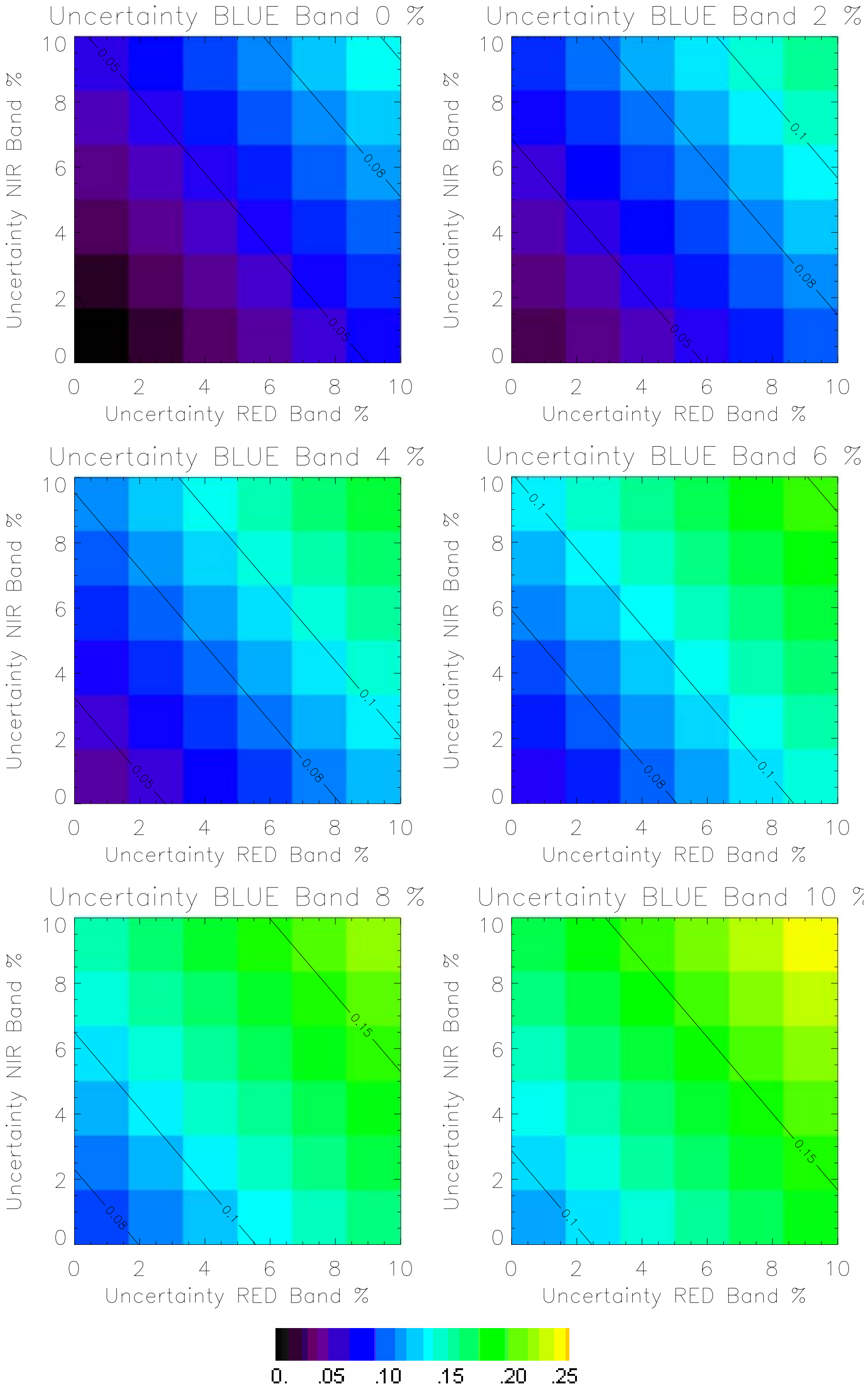

Figure 4: Average of ΔFAPAR values as function as ($\Delta\rho_{RED}$, $\Delta\rho_{NIR}$) for 6 values of $\Delta\rho_{BLUE}$.

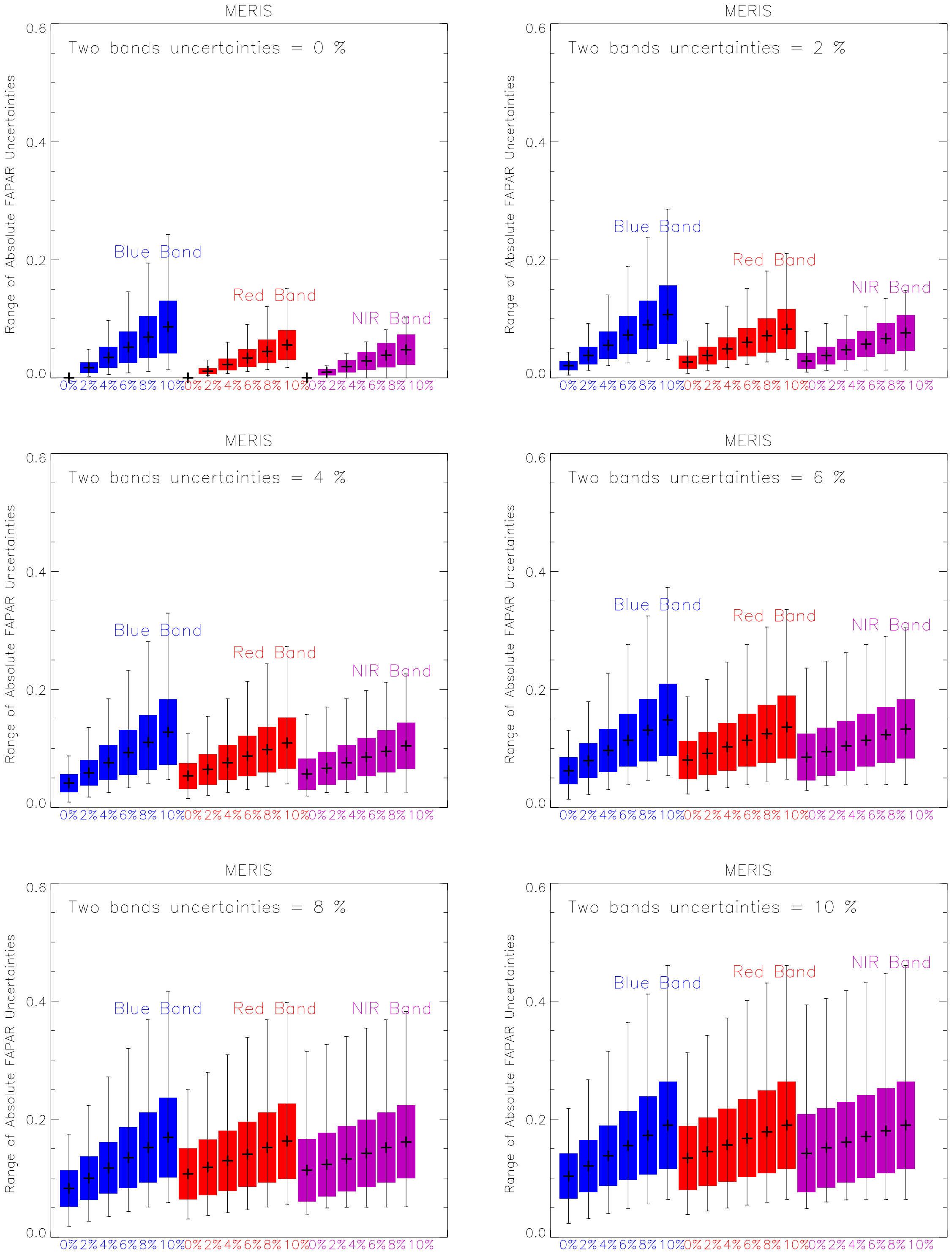

Figure 5: The 6 panels illustrate how the range of absolute deviation of FAPAR, ΔFAPAR, varies when the uncertainties of at least two bands of MERIS increase from 0% to 10 % as function of the third uncertainty band in x-axis. The cross symbol correspond to averaged value of ΔFAPAR over all simulations with the standard deviation ±σ in full column. Error bars indicate the minimum and maximum values in the ensemble.

- ***Expected differences in FAPAR as function of spectral calibration in the SeaWiFS and MERIS bands.***

Figure 6, Figure 7 and Figure 8 show the scatter-plots when comparing the two JRC-FAPAR products derived from MERIS-like data and SeaWiFS like-data with various level of uncertainties in blue, red and near-infrared spectral band, respectively, associated to each sensor. The data used in the plots correspond to the MERIS simulated top of atmosphere data. The different colors indicate the level of uncertainties from 0 % (dark blue), 2 % (blue), 4% (light purple), 6% (orange) and 8 % (pink) in the spectral band indicated in the title. The scattered points around the 1:1 line indicate large differences between the two FAPAR derived from the two instruments. The averaged values over all the synthetic cases are reported in Tables 4, 5 and 6, respectively. The red color (bold) numbers correspond to the value of the absolute difference of FAPAR between two instruments when larger than 0.05 (0.10). In these exercises, only one spectral band uncertainty in both instruments is taken into account. Note also that both the geometries of illumination and observation are the same with the simulated data when comparing the results.

The results in the blue band illustrate first that the differences between the FAPAR derived from the two instruments increase 1) when both FAPAR values are high and 2) with the uncertainties in blue bands are larger that 4 %.

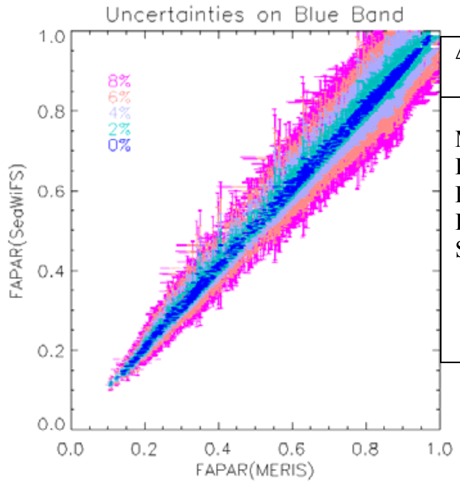

ΔFAPAR		SeaWiFS								
		-8	-6	-4	-2	0	2	4	6	8
MERIS	-8	0.0045	0.0184	0.0377	0.0377	0.0771	**0.1165**	**0.1165**	**0.1362**	**0.1559**
	-6	0.0189	0.0046	0.0207	0.0402	0.0598	0.0796	0.0993	**0.1190**	**0.1386**
	-4	0.0361	0.0164	0.0057	0.0230	0.0426	0.0623	0.0819	**0.1017**	**0.1213**
	-2	0.0534	0.0337	0.0141	0.0073	0.0254	0.0450	0.0647	0.0844	**0.1041**
	0	0.0706	0.0510	0.0313	0.0120	0.0093	0.0278	0.0475	0.0672	0.0868
	2	0.0879	0.0682	0.0485	0.0288	0.0123	0.0114	0.0303	0.0499	0.0696
	4	**0.1051**	0.0855	0.0657	0.0461	0.0264	0.0089	0.0136	0.0327	0.0523
	6	**0.1224**	**0.1027**	0.0831	0.0634	0.0437	0.0241	0.0079	0.0160	0.0352
	8	**0.1397**	**0.1200**	**0.1003**	**0.1003**	0.0771	0.0218	0.0218	0.0075	0.0183

Figure 6 and Table 4: Comparison between FAPAR derived from SeaWiFS (y-axis) and MERIS (x-axis) in case of same geometries of illumination and observations as function of $\Delta\rho_{BLUE}$ values from 0 % to 10 %.

The values reported in the Table 4 indicate that, when the uncertainties of the two instruments in blue band are of the same order of value (diagonal), the differences between the two FAPAR is in general less than 0.01. This difference increases up to 0.05 when the difference between the two spectral bands uncertainties in the blue domain is at about 6 %, i.e. $|\Delta\rho_{BLUE}(\text{MERIS})-\Delta\rho_{BLUE}(\text{SeaWiFS})| \approx 6$ %, and reach a value higher than 0.1 for 10 %.

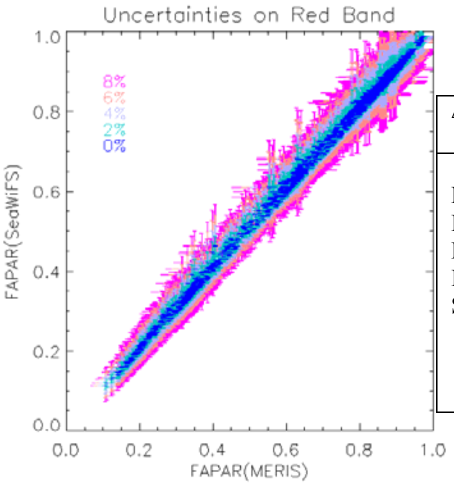

ΔFAPAR		SeaWiFS								
		-8	-6	-4	-2	0	2	4	6	8
MERIS	-8	0.0056	0.0281	0.0281	0.0404	0.0527	0.0650	0.0773	0.0897	**0.1020**
	-6	0.0082	0.0064	0.0172	0.0293	0.0415	0.0538	0.0662	0.0785	0.0908
	-4	0.0188	0.0073	0.0073	0.0184	0.0304	0.0427	0.0551	0.0674	0.0796
	-2	0.0300	0.0177	0.0065	0.0083	0.0195	0.0316	0.0438	0.0562	0.0685
	0	0.0412	0.0288	0.0166	0.0057	0.0093	0.0206	0.0327	0.0450	0.0574
	2	0.0523	0.0399	0.0277	0.0154	0.0053	0.0103	0.0217	0.0339	0.0462
	4	0.0634	0.0512	0.0388	0.0265	0.0142	0.0049	0.0113	0.0228	0.0351
	6	0.0746	0.0623	0.0499	0.0377	0.0254	0.0131	0.0048	0.0123	0.0240
	8	0.0858	0.0734	0.0611	0.0488	0.0365	0.0242	0.0120	0.0050	0.0133

Figure 7 and Table 5: Comparison between FAPAR derived from SeaWiFS (y-axis) and MERIS (x-axis) in case of same geometries of illumination and observations as function of ΔρRED values from 0 % to 10 %.

The scatter-plot on Figure 7 corresponds to the results in the red band. The differences between the FAPAR derived from the two instruments does less depend on the FAPAR value itself (scatter-plot 'comet' shape is less pronounced) than in the blue band. The values reported in the Table 5 indicate also that, when the uncertainties of the two instruments in the red band are on the same order of value (diagonal), the difference between the two FAPAR increases to 0.0133 when the bidirectional reflectance are over-estimated. This difference in general increases up to 0.05 when the difference between the two red bands uncertainties is at about 10 %, i.e. $|\Delta\rho_{RED}(\text{MERIS})-\Delta\rho_{RED}(\text{SeaWiFS})| \approx 10$ %.

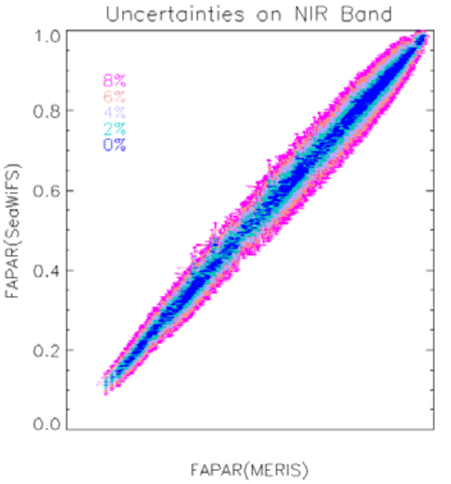

ΔFAPAR		SeaWiFS								
		-8	-6	-4	-2	0	2	4	6	8
MERIS	-8	0.0094	0.0173	0.0269	0.0366	0.0463	0.0559	0.0656	0.0752	0.0849
	-6	0.0081	0.0093	0.0174	0.0271	0.0367	0.0464	0.0561	0.0657	0.0754
	-4	0.0136	0.0078	0.0092	0.0175	0.0272	0.0368	0.0465	0.0562	0.0658
	-2	0.0222	0.0134	0.0075	0.0092	0.0177	0.0273	0.0369	0.0466	0.0563
	0	0.0312	0.0219	0.0131	0.0074	0.0093	0.0178	0.0275	0.0371	0.0467
	2	0.0405	0.0309	0.0218	0.0123	0.0072	0.0094	0.0179	0.0276	0.0372
	4	0.0499	0.0403	0.0308	0.0215	0.0126	0.0069	0.0094	0.0180	0.0277
	6	0.0594	0.0498	0.0402	0.0307	0.0213	0.0124	0.0069	0.0097	0.0181
	8	0.0688	0.0593	0.0497	0.0401	0.0305	0.0212	0.0124	0.0067	0.0099

Figure 8 and Table 6: Comparison between FAPAR derived from SeaWiFS (y-axis) and MERIS (x-axis) in case of same geometries of illumination and observations as function of $\Delta\rho_{NIR}$ values from 0 % to 10 %.

The plot on Figure 8 corresponds to the results in the near-infrared band. The differences between the FAPAR derived from the two instruments is like the red band except that for the low and high values of FAPAR the differences seem to be less sensitive to the NIR uncertainties. The values reported in the Table 6 show that when the uncertainties of the two instruments in the NIR band are on the same order of value (diagonal), the differences between the two FAPAR is constant at about 0.0095 and that this difference does not depend on the level and sign of the uncertainties. The difference in general increases until 0.05 when the difference between the two NIR bands uncertainties is at about 12 %, i.e. $|\Delta\rho_{NIR}(MERIS)-\Delta\rho_{NIR}(SeaWiFS)| \approx 12$ %.

- ***Calibration Impacts using actual data***

The following examples are made using two sets of SeaWiFS data over Europe for the first half of 2004. The calibration values corresponding to the two products have been changed with the following SeaWiFS calibration Table.

SeaWiFS calibration:

Calibration Table Number	200401	200404	200501
Version 0002	January to December	na	na
Version 0003	na	January to July	August to December

(Source : http://oceancolor.gsfc.nasa.gov/seadas/versions.html)

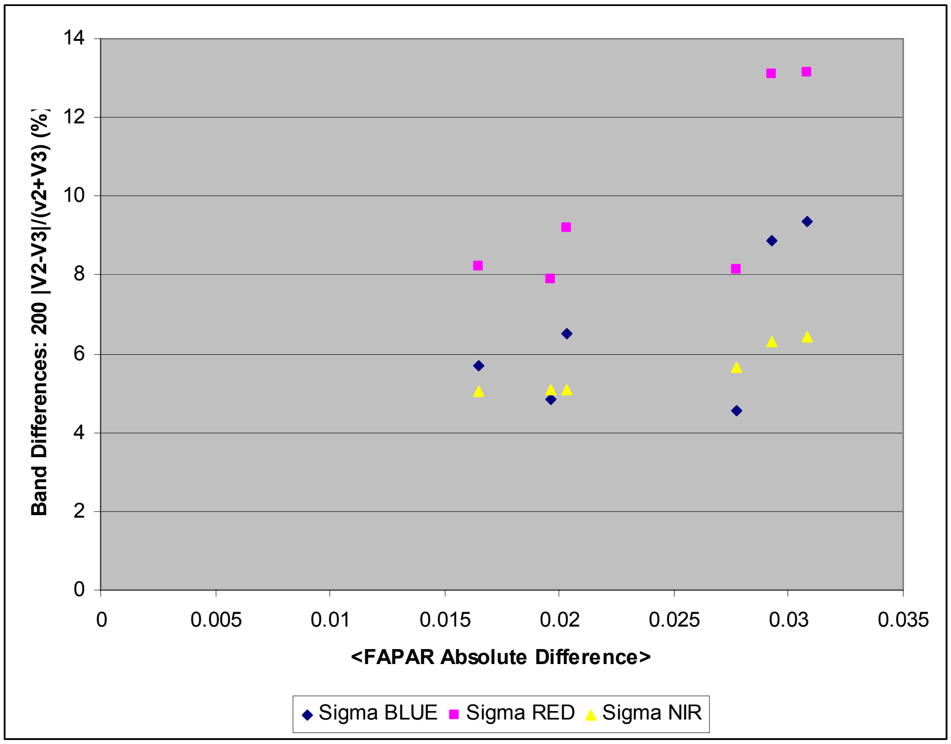

Figure 9: Summarize of the differences of absolute FAPAR averaged over Europe for 6 months as function of the averaged differences between the two SeaWiFS datasets for each BRF TOA 3 spectral bands in per cent.

We compare here the monthly FAPAR products over Europe at a spatial resolution of 1.5 km from the two data sets as well as the three spectral BRF TOA corresponding to the representative value. The differences between the values are plotted in Figure 10 to Figure 15 for each month and the average over the entire geographical window is summarized in Figure 9. This latter figure shows that when the

January 2004

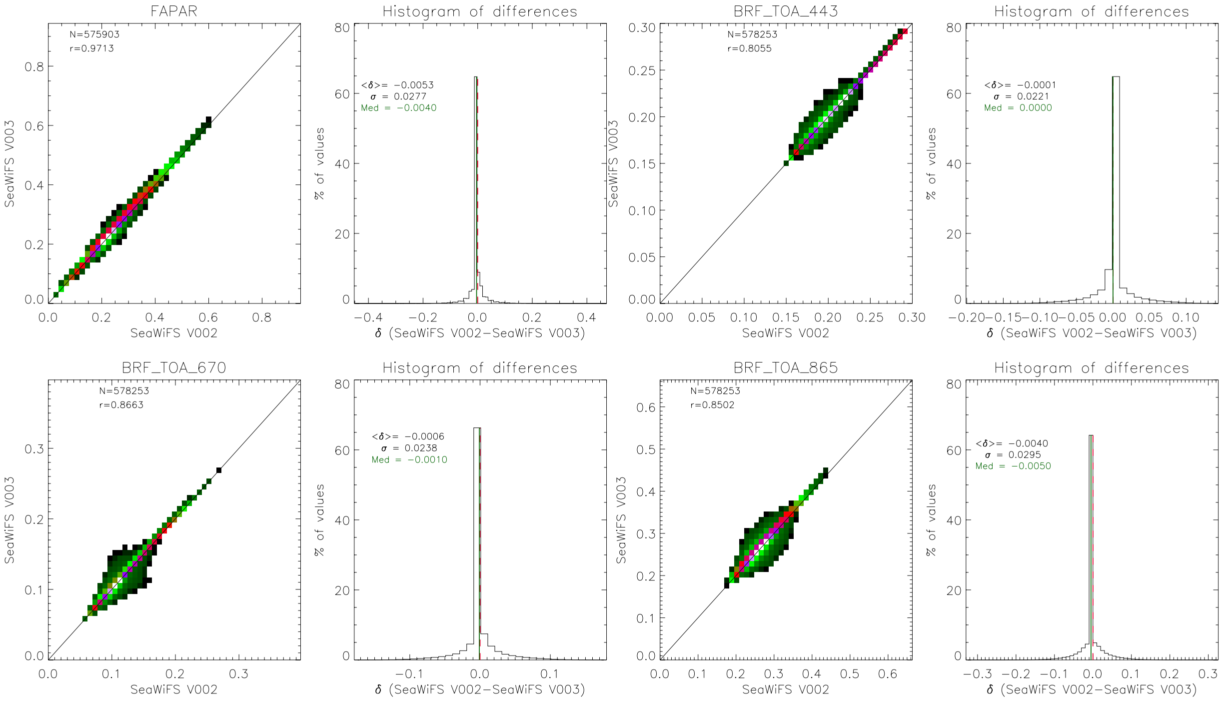

Figure 10: Scatter-plots and histogram of differences between the monthly FAPAR and its associated BRF TOA in the blue, red and near-infrared bands when using 'old' and new calibrated **SeaWiFS** data over Europe at 1.5 km in **January 2004**. N indicates the number of pixels, r the correlation, <δ> the mean of differences, σ the standard deviation and Med the median value of the differences.

February 2004

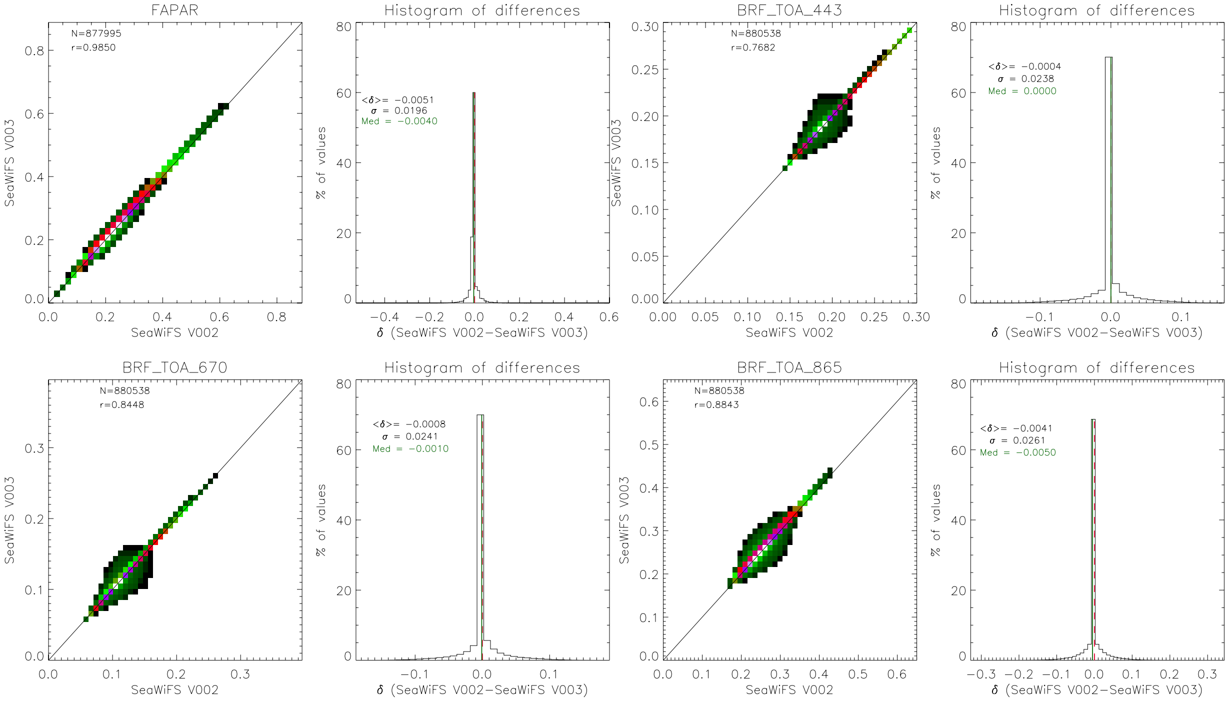

Figure 11: Scatter-plots and histogram of differences between the monthly FAPAR and its associated BRF TOA in the blue, red and near-infrared bands when using 'old' and new calibrated **SeaWiFS** data over Europe at 1.5 km in **February 2004**. N indicates the number of pixels, r the correlation, <δ> the mean of differences, σ the standard deviation and Med the median value of the differences.

March 2004

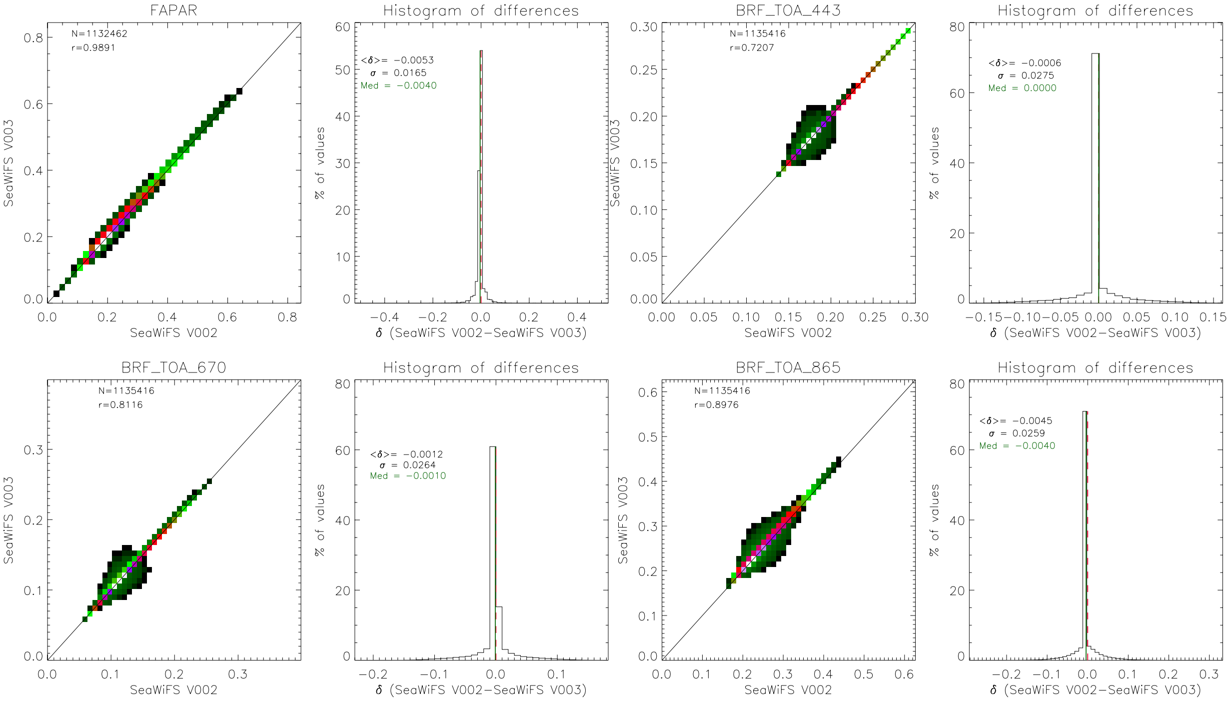

Figure 12: Scatter-plots and histogram of differences between the monthly FAPAR and its associated BRF TOA in the blue, red and near-infrared bands when using 'old' and new calibrated **SeaWiFS** data over Europe at 1.5 km in **March 2004**. N indicates the number of pixels, r the correlation, <δ> the mean of differences, σ the standard deviation and Med the median value of the differences.

April 2004

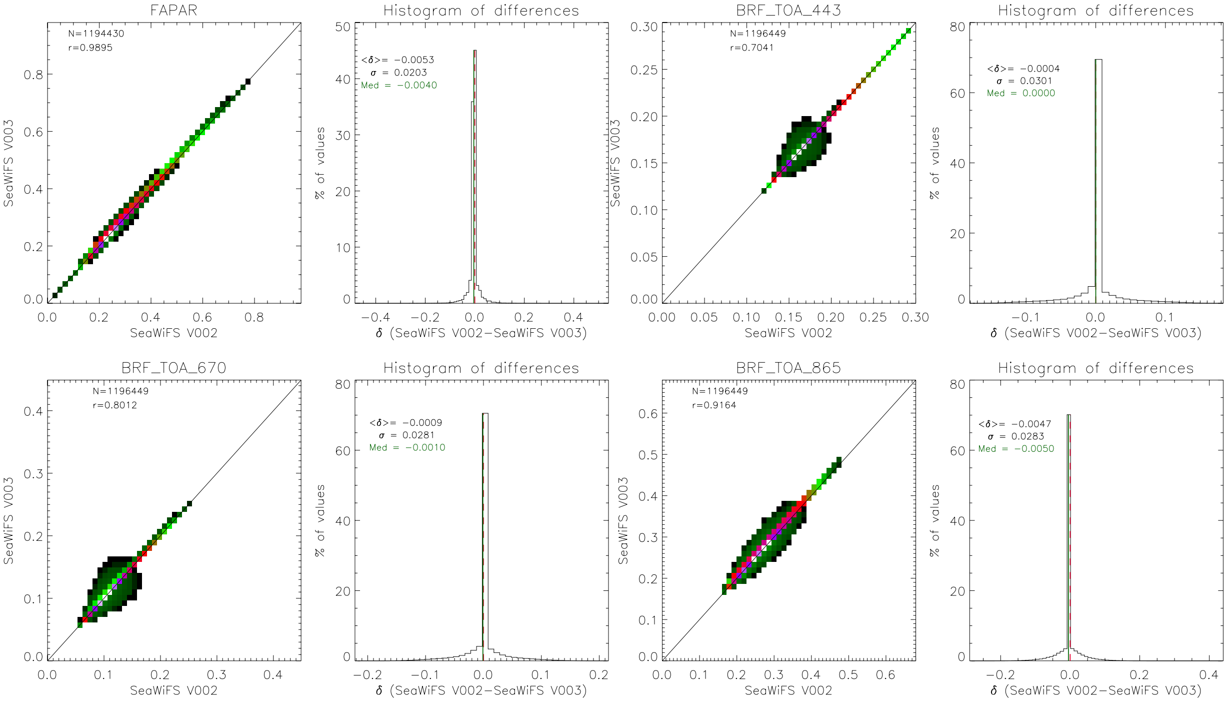

Figure 13: Scatter-plots and histogram of differences between the monthly FAPAR and its associated BRF TOA in the blue, red and near-infrared bands when using 'old' and new calibrated **SeaWiFS** data over Europe at 1.5 km in **April 2004**. N indicates the number of pixels, r the correlation, <δ> the mean of differences, σ the standard deviation and Med the median value of the differences.

May 2004

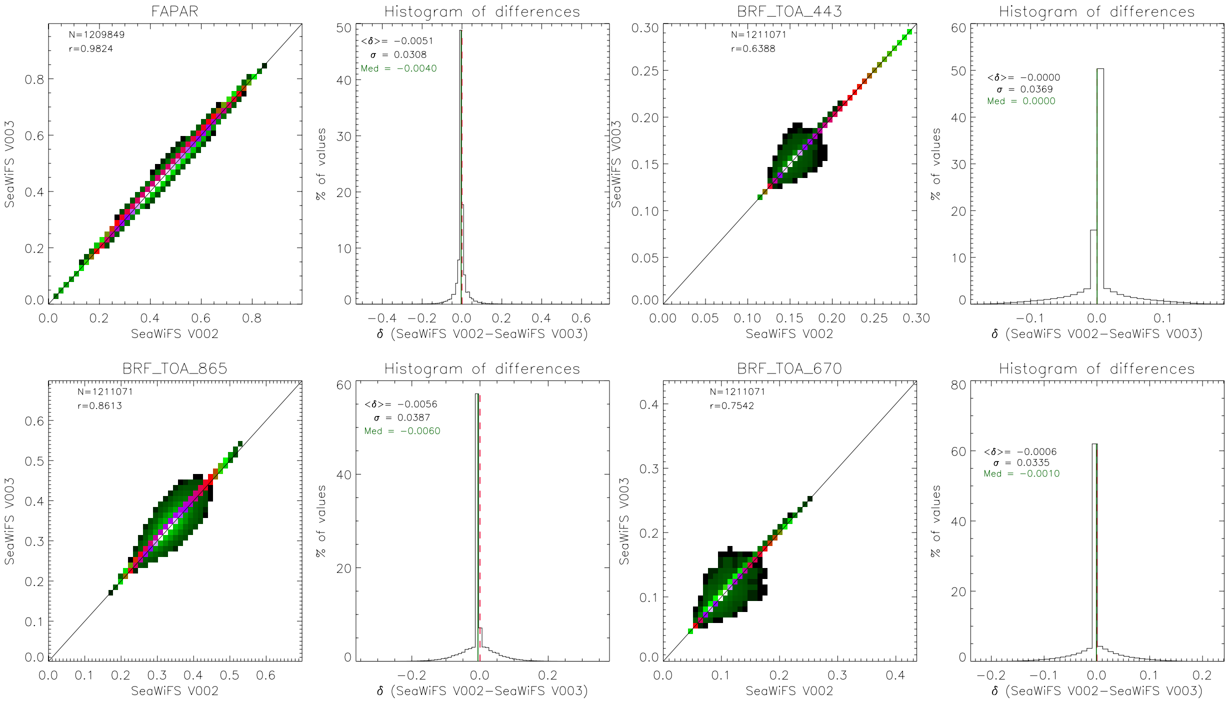

Figure 14: Scatter-plots and histogram of differences between the monthly FAPAR and its associated BRF TOA in the blue, red and near-infrared bands when using 'old' and new calibrated **SeaWiFS** data over Europe at 1.5 km in **May 2004**. N indicates the number of pixels, r the correlation, <δ> the mean of differences, σ the standard deviation and Med the median value of the differences.

June 2004

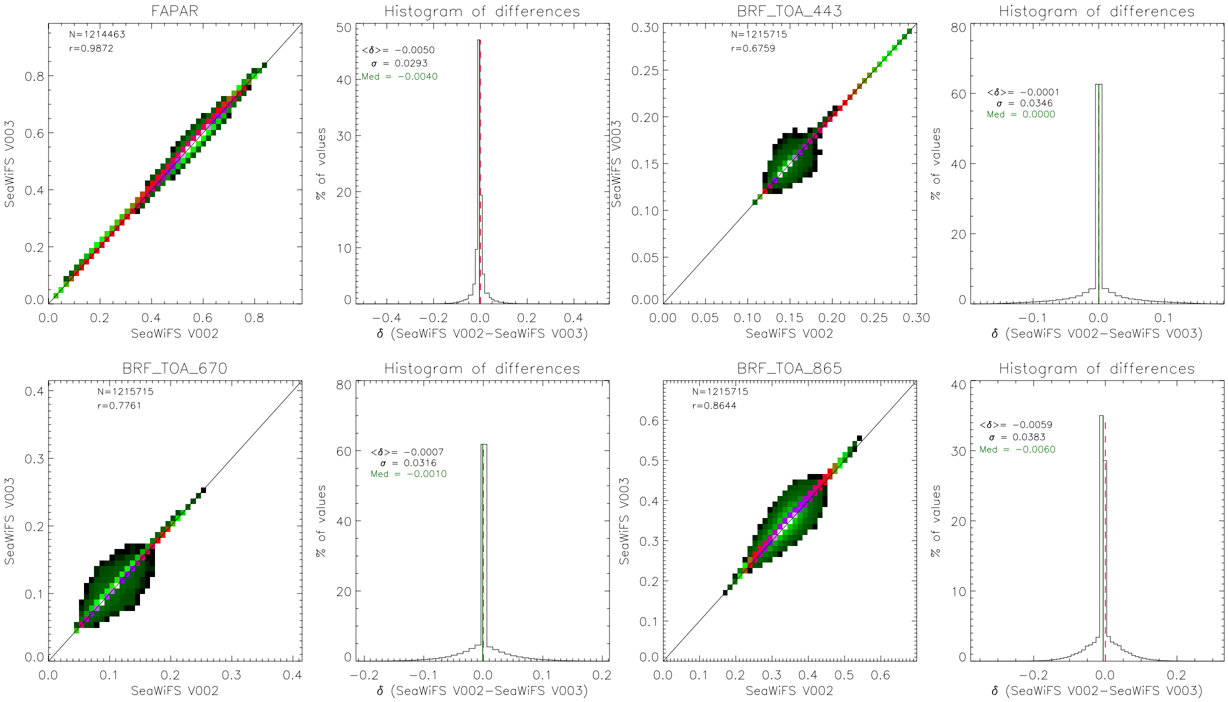

Figure 15: Scatter-plots and histogram of differences between the monthly FAPAR and its associated BRF TOA in the blue, red and near-infrared bands when using 'old' and new calibrated **SeaWiFS** data over Europe at 1.5 km in **June 2004**. N indicates the number of pixels, r the correlation, <δ> the mean of differences, σ the standard deviation and Med the median value of the differences.

averaged differences between BRF TOA are higher than 6% in all bands, the difference in FAPAR is about 0.03-0.04. The differences of monthly FAPAR do not depend on the season and are not dependent on the level of FAPAR, i.e. all the range of value are affected when the daily spectral calibration is changing. It remains to be investigated whether the differences are induced by a divergence in the selected day during the time-composite.

5. Time-composite Algorithm

A Time Composite code has been developed in C++ specifically for MERIS products and the description of the output products is available in [10].

The code has been designed to be reusable with FAPAR products derived from other sensor since the algorithm is generic *(~ 2700 lines of code including 1900 lines for HDF files classes)* and interacts with C++ classes which are sensor/file dependent *(~ 500 lines of code).*

To process data from a new instrument, only the sensor-dependent classes have to be written. It has been done for MODIS and MOS. This design decreases the development time needed to integrate a new sensor as well as the amount of code to maintain. It has been developed for comparing monthly product derived from daily MERIS, SeaWiFS and MODIS products. The following time-composite algorithm described in [9] was applied:

Compute the temporal average and corresponding deviation of product, e.g., FAPAR over an T-day period:

$$\overline{S} = \tfrac{1}{T}\sum_{t=1}^{T} S(t)$$

Select the “most representative day” in the N-days time series, i.e., report the FAPAR daily value that minimizes:

$$\Delta_S^T = \frac{1}{T}\sum_{t=1}^{T} | S(t) - \overline{S} |$$

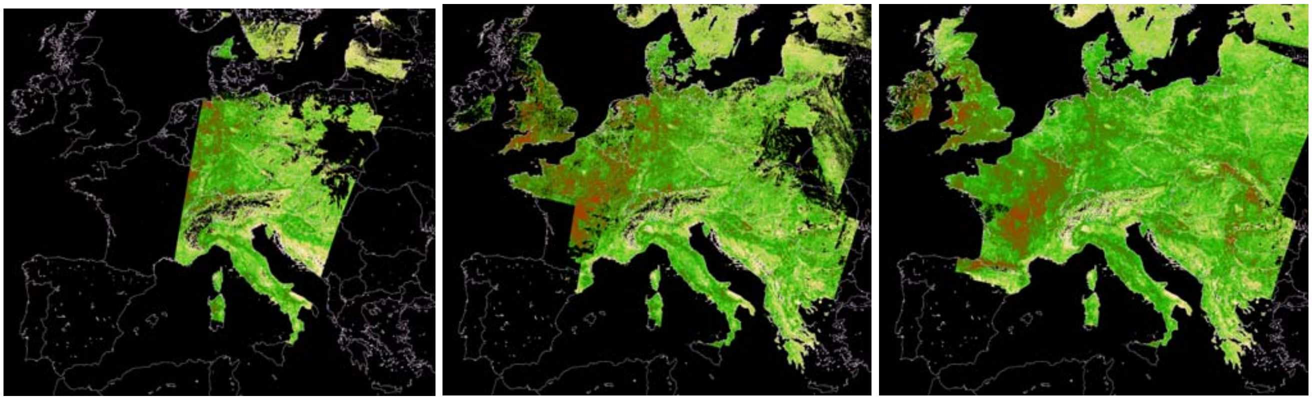
One Day 10-day monthly

Figure 16: Example of coverage map over Europe for one day, 10-day and monthly period.

Geophysical quantities and products can be traced back to the selected (most representative) day and are thus corresponding to physical values actually delivered by the FAPAR algorithm. The time composite algorithm is applied to several daily Level 2 products remapped over the same geographical window to generate Level 3 products.

6. Regional and temporal sampling

The next two sections concern the comparison of MERIS, MODIS and SeaWiFS data only over large geographical regions when data are available.

a. Single date images

MERIS, SeaWiFS and MODIS products have been re-mapped on the same geographical region in a rectangular projection at a resolution of 1.2 km (i.e. MERIS RR resolution) allowing the direct comparison of FAPAR values on a location by location basis.

Table 7: Location and dates of RR MERIS Level 2 data for European window

Site Name	Latitude	Longitude	Dates
AAOT	45.3	12.5	19-06-2002
AERONET	43.41	7.19	01-10-2002
BOREAS	53.98	-105.12	25-07-2002
GEESTHACHT	53.5	10.5	21 (22) -08 -2002
STATION_271	57.32	20.05	07-05-2002
STATION_114	54.86	13.28	06-08-2002
OUAGADOUGOU	12.15	-1.35	03-09-2002
Reprocessed Data			
BOREASSSA	51.00	-99.5	09/04/2003
JORNADA	34.00	-105.00	01/01/2003 06/04/2003 09/04/2003 10/04/2003 13/04/2003
MARICOPA	35.00	-112.00	27/12/2003
YATIR	33.00	34.00	30/04/2003

Results are shown in Annex A and B and analyzed in Section 7.

b. Monthly European products (NEW)

Comparisons over European countries have been made between Level-3 products using SeaWiFS and MERIS over the year 2003 and with MODIS for April 2003. The remote sensing data used in this exercise cover the geographical region between [-20°, 50°] in longitude and [30°, 80°] in latitude. The map is in the Lambert Azimuthal Equal Area projection which corresponds to the official EU projection concerning the EU-25 countries as defined at http://crs.bkg.bund.de/crs-eu/. The comparisons have been done using products re-mapped or re-gridded at 2 km spatial resolution.

Results are shown in Annex C and analyzed in Section 7.

c. Time series over CarboEurope IP sites

Comparison of MGVI with similar products derived from similar sensors for a series of European sites over a substantial period of time is done in this section. The emphasis have been placed on documenting to what extent the MGVI product from the ENVISAT ground segment documents the temporal evolution of the productivity of the vegetation for a series of well-documented sites in Europe. These sites are part of the CarboEurope network of field campaigns.

Table 8: Location and names of CarboEurope IP sites

Site Name	Latitude	Longitude
Braschaat	51.30917 N	4.520556 E
Castelporziano	41.70581 N	12.37731 E
Flakaliden	64.11278 N	19.45694 E
Hainich	51.0792 N	10.45218 E
Hesse	48.67422 N	7.064617 E
Hyytiälä	61.84742 N	24.29476 E
Lavarone	45.95526 N	11.28118 E
Loobos	52.16786 N	5.743959 E
Roccarespampani	42.39025 N	11.92094 E
Soroe	55.48694 N	11.64583 E
Tharandt	50.96361 N	13.56694 E

Results are shown in Annex D.

d. Time series over EOS ground validation sites (NEW)

Comparison of ***lastest process MGVI*** (MGS-PC/7.4) with similar products derived from the SeaWiFS, MERIS, MODIS, MISR and MOS instruments for a set of 11 well-documented EOS calibration and validation sites began during this project. We will present here the preliminary results over two sites, namely Bondville and Konza prairie.

Table 9: EOS validation sites description: location and vegetation type.

Site Name	Location	Latitude	Longitude	Biome
Bondville (AGRO)	**Illinois, USA**	**40.006627**	**-88.291030**	**Corn and soybean**
Braschaat (De Inslaag)	Belgium	51.30917	4.520556	Conifer/broad-lead-scrub forest
Dahra	Senegal	15.3675	-15.4434	Semi-arid grass savannah
Dahra North	Senegal	15.4119	-15.4335	
Tessekre South	Senegal	15.8192	-15.0609	
Tessekre North	Senegal	15.8960	-15.0609	
Metolius (METL)	USA	44.437189	-121.566756	Dry needle-leaf forest
Mongu	South Africa	-15.4383	23.2533	Shrub-land/woodland
Sevilleta (SEVI)	USA	34.360290	-106.700285	Desert grassland
Harvard Forest	USA	42.538259	-72.171378	Conifer/broad-leaf forest
Konza	**KS, USA**	**39.082286**	**-96.560251**	**Grassland/Cereal Crop**

7. Results of comparison

The figures presenting the results of comparison between FAPAR derived from various sensors are given in appendices when indicated.

a. Single date images (Annex A)

These case studies have been made using **MERIS Level 2 processing MEGS-PC/6.1** (ACRI) software.
In case of daily comparison of (instantaneous) FAPAR products derived from MERIS, SeaWiFS and MODIS data, 3 color maps of remapped FAPAR are displayed using a color scale varying from white, green to red for the value of FAPAR about 0, 0.5 to 1.0. The non-processed data in anyone of the two three sensors have been masked (black pixels). They correspond to either shadow or clouds contamination, or bare soil pixels. We also removed the points for which the solar (viewing) zenith angle values were higher than 60 (45) degrees. These thresholds correspond to the sun angle limit in the radiative transfer models and to the larger observation angle for which the size of the pixel is larger than 2.0 km.
Figure 28 to Figure 43 summarize the comparison results over the data described in Table 7. The panels illustrate the comparison of FAPAR derived from MERIS or SeaWiFS values against the FAPAR derived from SeaWiFS or MODIS. Both scatter-plots and histograms of differences are plotted using data over the vegetated pixels only and the following statistics of differences are reported:

- <δ> corresponds to the average of the difference between FAPAR derived from sensor 1 and sensor 2 over all pixels.
- σ indicates the standard deviation of the difference between the 2 ensembles to be compared.
- Median corresponds to the median value of the differences between the two ensembles to be compared.
- r is the linear Pearson correlation coefficient between the two data string.

The values of the three first statistics values are reported for each image in Table 10.

In general, we can see that the standard deviation is of about 0.1179 (0.10604) between the MERIS and SeaWiFS or MODIS products, whereas the standard deviation between SeaWiFS and MODIS is about 0.1239.

The <δ> /Median values show that we have a small bias between MERIS and SeaWiFS (MODIS) of about -0.036/-0.040 (-0.016/-0.019) which means that FAPAR derived from MERIS is smaller than the FAPAR derived from SeaWiFS (MODIS). However, it seems that MERIS and MODIS provide closest values. The difference between SeaWiFS and MODIS is, on average, of about 0.0390/0.0394.
The bias between SeaWiFS and other sensor FAPAR product is, however, quite small and the reasons for this bias could be the following:

- Different acquisition. The FAPAR depends on the Sun zenith angle as it has been shown by in-situ measurements and by radiative transfer simulations. Since the JRC-FAPAR algorithms provide instantaneous estimates, the differences in the time of acquisition can therefore explain the bias between the two products.

- Extra shadowing clouds effects are also to be anticipated in the case of MERIS.
- Calibration issues: if at least one of the three spectral bands is not inter-calibrated between two instruments, we can expect to have a systematic difference in the FAPAR product as it has been shown in previous section.

Table 10: Statistics values when comparing FAPAR values from a pair of instruments.

Sensor Pair	**MERIS/SeaWiFS**			**MERIS/MODIS**			**SeaWiFS/MODIS**		
Site Name\Statistics of differences	**<δ>**	**σ**	**Median**	**<δ>**	**σ**	**Median**	**<δ>**	**σ**	**Median**
AAOT	-0.0363	0.1262	-0.036	-0.0129	0.1151	-.0131	.0185	0.129	0.016
AERONET	-0.0295	0.1208	-0.0397	0.0185	0.1027	0.0167	0.0553	0.1135	0.056
BOREAS	-0.0244	0.1197	-0.0289	-0.006	0.1085	-0.0079	.0123	.1187	0.008
GEESTHACHT_233	-0.0513	0.1229	-0.0567	-0.0825	0.0646	-0.0838	.0384	.1329	0.048
GEESTHACHT_234	-0.0514	0.1071	-0.05	-0.008	0.123	-0.0093	.0694	.1393	0.064
STATION_271	-0.0533	0.1043	-0.0535	-0.0224	0.1086	-0.0255	.0236	.1069	0.024
STATION_114	-0.0092	0.1243	-0.0168	-0.0023	0.1198	-0.0122	.0612	.1272	0.06
Averaged values	**-0.0369**	**0.1179**	**-0.0402**	**-.01652**	**.10604**	**-0.0193**	**.0398**	**.1239**	**.0394**
OUAGADOUGOU				0.0319	0.0601	0.0308			

In the following section, we will try to document the differences by using newly reprocessed MERIS data, i.e. software **MEGS-PC/7.4**. Note that because the reprocessing has been operated for data acquired in 2003 we can not show the results of comparisons over the same regions as above.

b. Single date images with reprocessed data (Annex B)

First of all, a first inter-comparison has been made between two sets of Level-2 MERIS coming from 'old' (**Level 2 MEGS-PC/6.1)** and 'new' (**Level 2 MEGS-PC/7.4**) processing over European region on the 13 August 2003. The technical differences between the two processing software versions are explained in http://earth.esa.int/pcs/envisat/meris/documentation/MERISRRsecondreprocessing-V2.pdf.

Figure 17 summarizes the results with the two maps of FAPAR, the scatter-plot, the histogram of differences and the map of differences. The value of the averaged difference, <δ>, is about 0.0013 and over this particular region, the FAPAR from the reprocessed MERIS data is a little bit larger than for the previous one.
The map of FAPAR differences shows that they are located in various lines along track, which may come from the 'smile effect' correction which has been implemented in the new processing chain. (http://earth.esa.int/pcs/envisat/meris/documentation/MERIS_Smile_Effect.pdf).

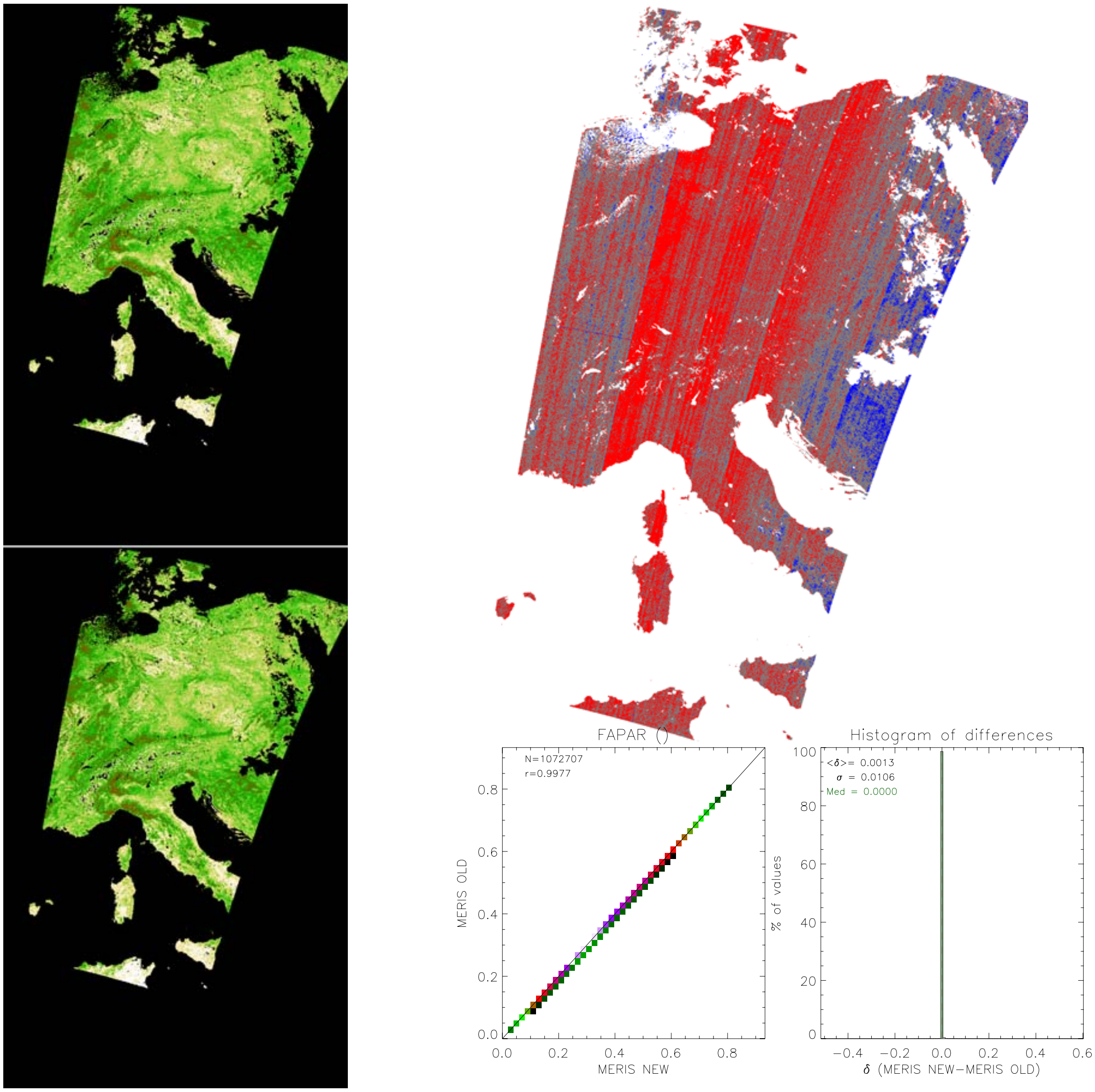

Figure 17: Left panel: maps of FAPAR values remapped at 1.2 km for MERIS new (top) and MERIS old (bottom). Bottom right panel: Scatter-plots and histogram of difference between FAPAR values remapped at 1.2 km derived from MERIS (new) and MERIS (old). N indicates the number of pixels, r the correlation, <δ> the mean of differences, σ the standard deviation and Med the median value of the differences. Upper right panel: map of differences between the two data sets. (Grey color indicates no difference, red color a positive difference and blue color a negative one.)

The calibration coefficients have been changed and the maps (Figure 18) show the differences (new – old) in the three spectral bands at the level of top of atmosphere radiances. The left map shows that the blue band is larger in the new processing than the previous one over the entire region. The value of this difference is about 1 $\mathrm{mWst^{-1}m^{-2}}$ (comparing to an averaged value of 60 $\mathrm{mWst^{-1}m^{-2}}$). The middle map corresponds to the red band for which the differences are also positive but with some lines along tracks which are negative. These features are also found in the near-infrared bands with more effects on the eastern region.

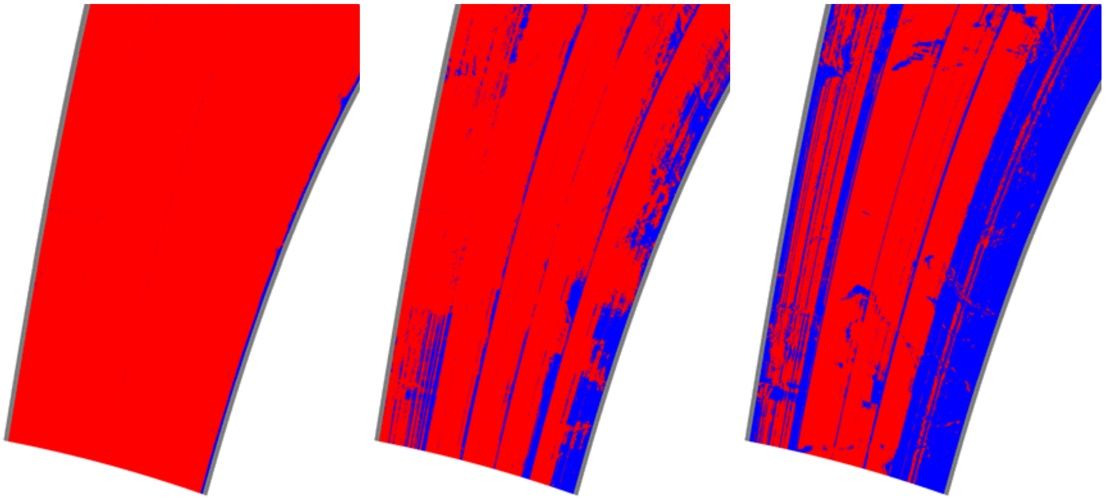

Figure 18: Maps of difference values between the radiances at the top of atmosphere from the old and the new processing in the blue, red and near-infrared bands. (Grey color indicates no difference, red color a positive difference and blue color a negative one.)

The new processed MERIS data do not imply large differences between the FAPAR products. In general, FAPAR may be a slightly larger with the new version.

In the following, we compare the new reprocessed MERIS products versus SeaWiFS and MODIS data when available over the regions described in Table 9. Figure 44 to Figure 57 illustrate the comparison results over these cases. The statistics values of differences (same as above) are reported in Table 11.

Table 11: Values of correlation when comparing FAPAR values from three instruments.

Sensor Pair	**MERIS/SeaWiFS**			**MERIS/MODIS**			**SeaWiFS/MODIS**		
Site Name\Statistics of differences	**<δ>**	**σ**	**Median**	**<δ>**	**σ**	**Median**	**<δ>**	**σ**	**Median**
BOREAS_SSA	-0.0158	0.0230	-0.0168	-.0036	0.023	-.0051	0.0096	.0261	0.008
JORNADA									
01/01/2003	0.0103	0.0399	0.008	0.011	0.0483	-.0009			
06/04/2003	-0.0197	0.0361	-0.0213	-.0318	0.0439	-.0294	-0.0042	.0552	-0.004
09/04/2003	-0.0174	.0318	-0.02	-0.0302	0.0302	-.0029	0.0085	.0316	0.012
10/04/2003	-0.0264	0.0661	-0.0268	-.0701	0.0719	-.0691	-0.0107	.0697	-0.004
13/04/2003	-0.0239	0.0578	-0.0248						
Maricopa/Metiolius	0.0037	0.0448	0.0066						
Yatir				-.0162	0.0735	-0.0165			
Averaged Values	-0.01223	0.040714	-0.00667	-0.02088	0.053578	-0.02376	-0.00745	0.06245	-0.004

It seems that with these new reprocessed MERIS data, the magnitude of the differences between FAPAR products derived from MERIS and SeaWiFS are smaller than with the previous data.
The averaged σ value decreases from 0.1179 to 0.0407 when comparing MERIS and SeaWiFS images, and decreases from 0.10604 to 0.053578 with MODIS. The differences between SeaWiFS and MODIS also gets smaller which means that we can not conclude that the new reprocessing brings better results and especially because a bias is still there.

At this stage, we can not therefore conclude that the new reprocessing data has a positive impact on the results.

Figure 19 and Figure 20 show the σ and averaged differences <δ> as a function of the Sun zenith angle values averaged over each image. The diamond and square (triangle) symbols in pink (blue) color correspond to the comparison between MERIS and SeaWiFS (MODIS), respectively whereas the brown to the comparison between SeaWiFS and MODIS. The differences in instantaneous FAPAR values do not vary with the Sun zenith angle values.

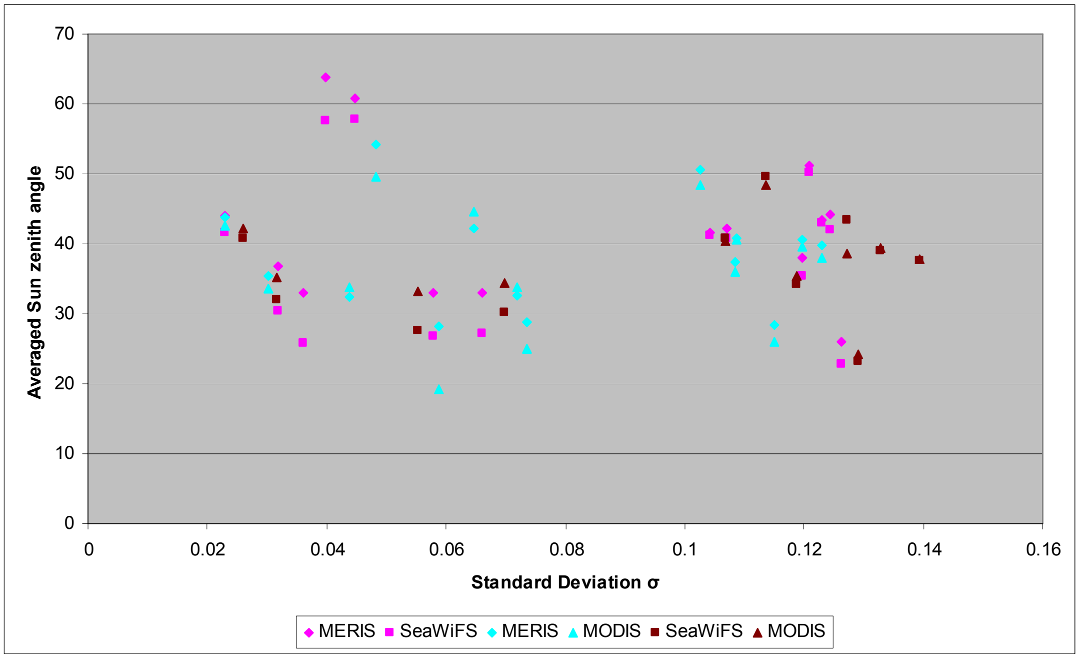

Figure 19: Sun zenith angles averaged over the images as function of the standard deviation of the FAPAR differences, σ

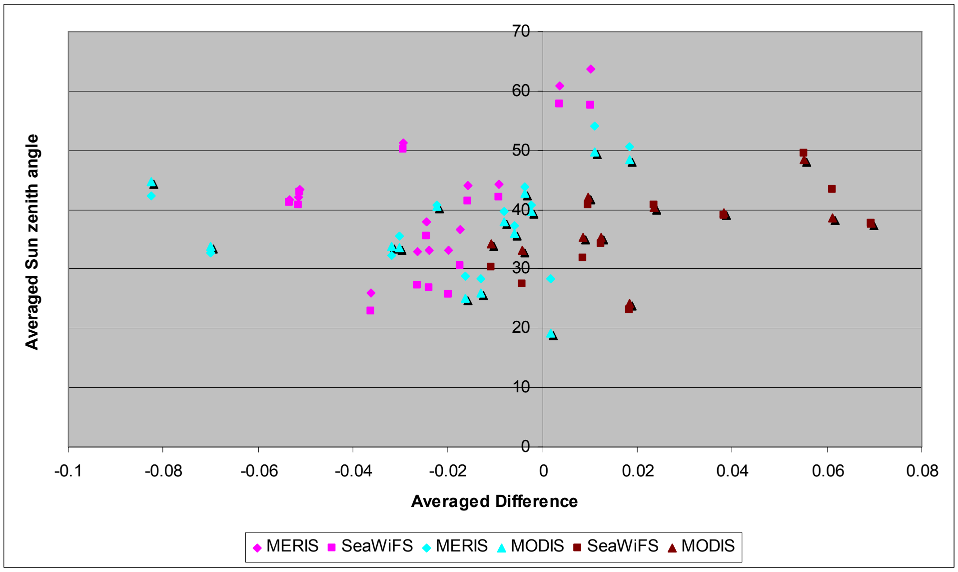

Figure 20: Sun zenith angles averaged over the images as function of the averaged difference of FAPAR, <δ>.

After comparing instantaneous products, we will compare now the time-composite products which permit us to remove possible outliers due to cloud shadow contamination.

a. Monthly European Products (Annex C)

FAPAR monthly products have been computed using the same time-composite technique described in [9] from SeaWiFS and MERIS daily products over the entire 2003.
These Level-3 products have been then remapped or aggregated into the EU-25 Lambert Azimuthal Equal Area (LAEA) projection at 2 km. Figure 60 to Figure 71 show the scatter-plots and histogram of differences when comparing the two results respectively from January to December 2003. The top figures correspond to the case where all points have been used in the statistics and the bottom one when we remove the pixels for which the Sun zenith angle is larger than 55°. The vertical red line indicates the difference value of zero and the green one is plotted for the median value of difference. Figure 21, Figure 22 and Table 12 summarize the results of statistics of differences between the two products as a function of each month in the case when all geometries of illumination are taken and when we remove the illumination larger than 55°. In general, the products from MERIS are lower than the values derived from SeaWiFS. These differences decrease by removing the large Sun zenith angles (orange and yellow lines) especially over the winter months. The values of the MERIS Sun zenith angles are always higher than for SeaWiFS during all the year because of the different time of acquisition.

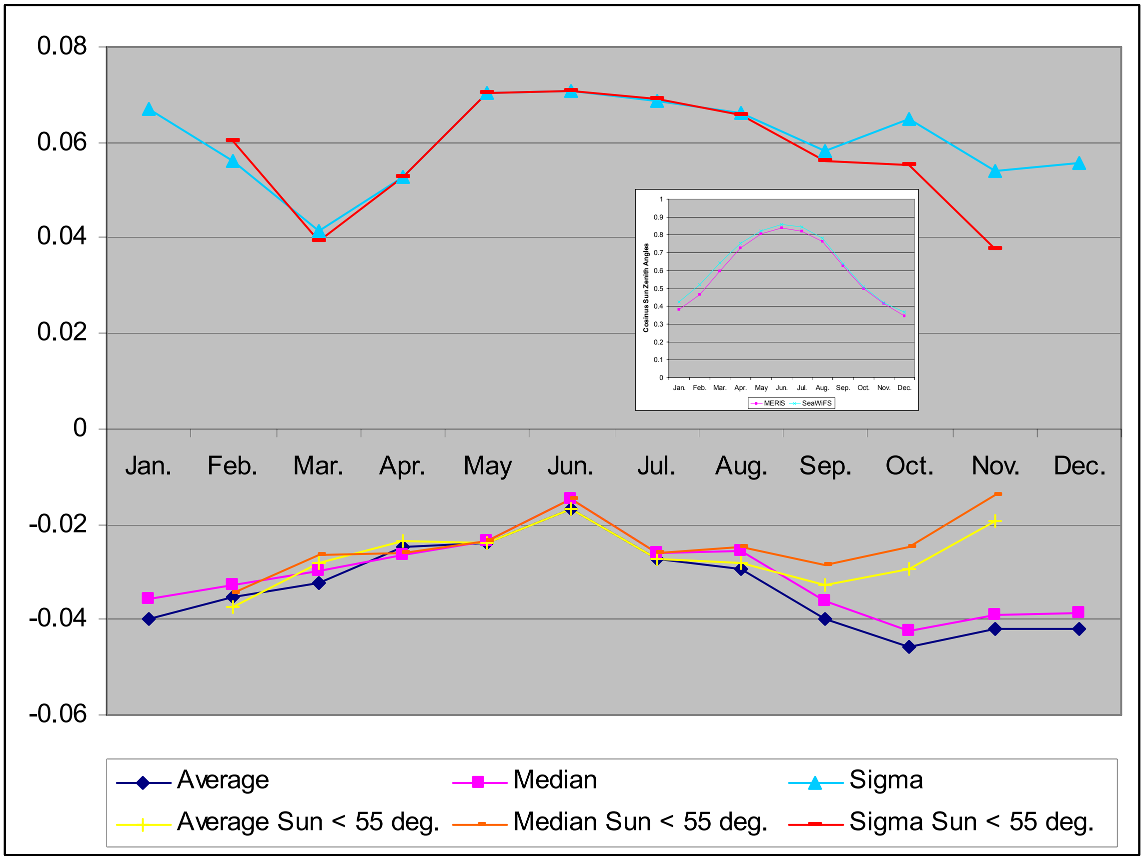

Figure 21: Statistics values of differences between MERIS and SeaWiFS products as function of month during the year 2003. The in-laid graph indicates the average values of the Sun zenith angles during the year (at the respective time of acquisition).

Table 12: Statistics of differences between MERIS and SeaWiFS product

	All Sun Zenith Angles					Sun Zenith Angle < 55 deg.				
Month	<δ>	Median	σ	r	N	<δ>	Median	σ	r	N
Jan.	-0.0398	-0.0358	0.0668	0.7997	530702					
Feb.	-0.0354	-0.0328	0.0562	0.8404	706531	-0.0373	-0.0343	0.0602	0.8661	37663
Mar.	-0.0322	-0.0298	0.0414	0.9246	1199544	-0.028	-0.0263	0.0395	0.9365	758391
Apr.	-0.0248	-0.0266	0.0528	0.9139	1431780	-0.0236	-0.0259	0.0528	0.9162	1367600
May	-0.024	-0.0236	0.0702	0.9026	1631328	-0.024	-0.0236	0.0702	0.9025	1629372
Jun.	-0.0167	-0.0149	0.0707	0.922	1685890	-0.0167	-0.0148	0.0708	0.9219	1683121
Jul.	-0.0273	-0.026	0.0688	0.9137	1694054	-0.0273	-0.0259	0.0689	0.9137	1693301
Aug.	-0.0293	-0.0256	0.0662	0.9049	1690745	-0.0282	-0.0248	0.0657	0.909	1611752
Sep.	-0.0397	-0.0362	0.0582	0.8906	1678285	-0.0328	-0.0286	0.0561	0.9222	1057508
Oct.	-0.0457	-0.0423	0.0651	0.8217	1400798	-0.0295	-0.0247	0.0553	0.8929	360795
Nov.	-0.0418	-0.0389	0.0541	0.8312	942466	-0.0194	-0.014	0.0377	0.9268	4156
Dec.	-0.0419	-0.0385	0.0556	0.8423	680871					

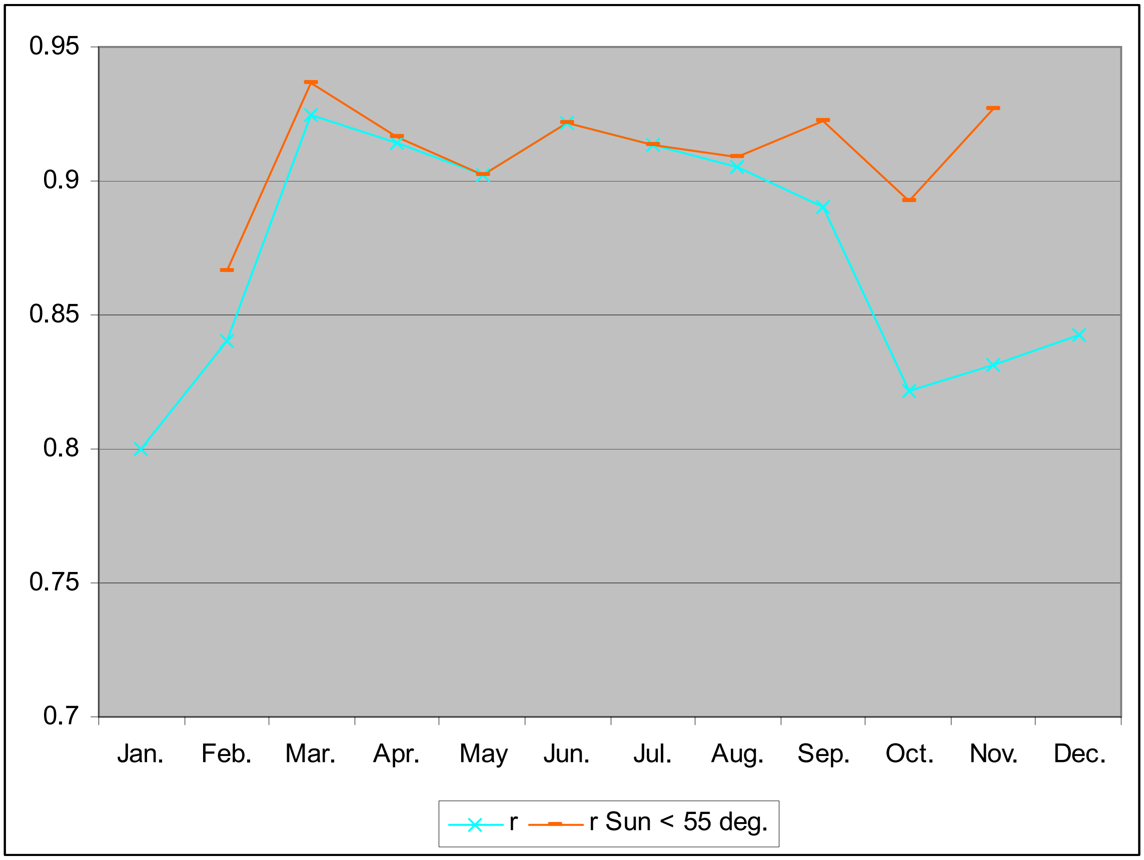

Figure 22: Correlation factor between monthly products from MERIS and SeaWiFS as function of each month over 2003.

In the previous exercise, we used MERIS Level-3 products which have been "aggregated" from 1.2 km pixel into the LAEA 2km map.

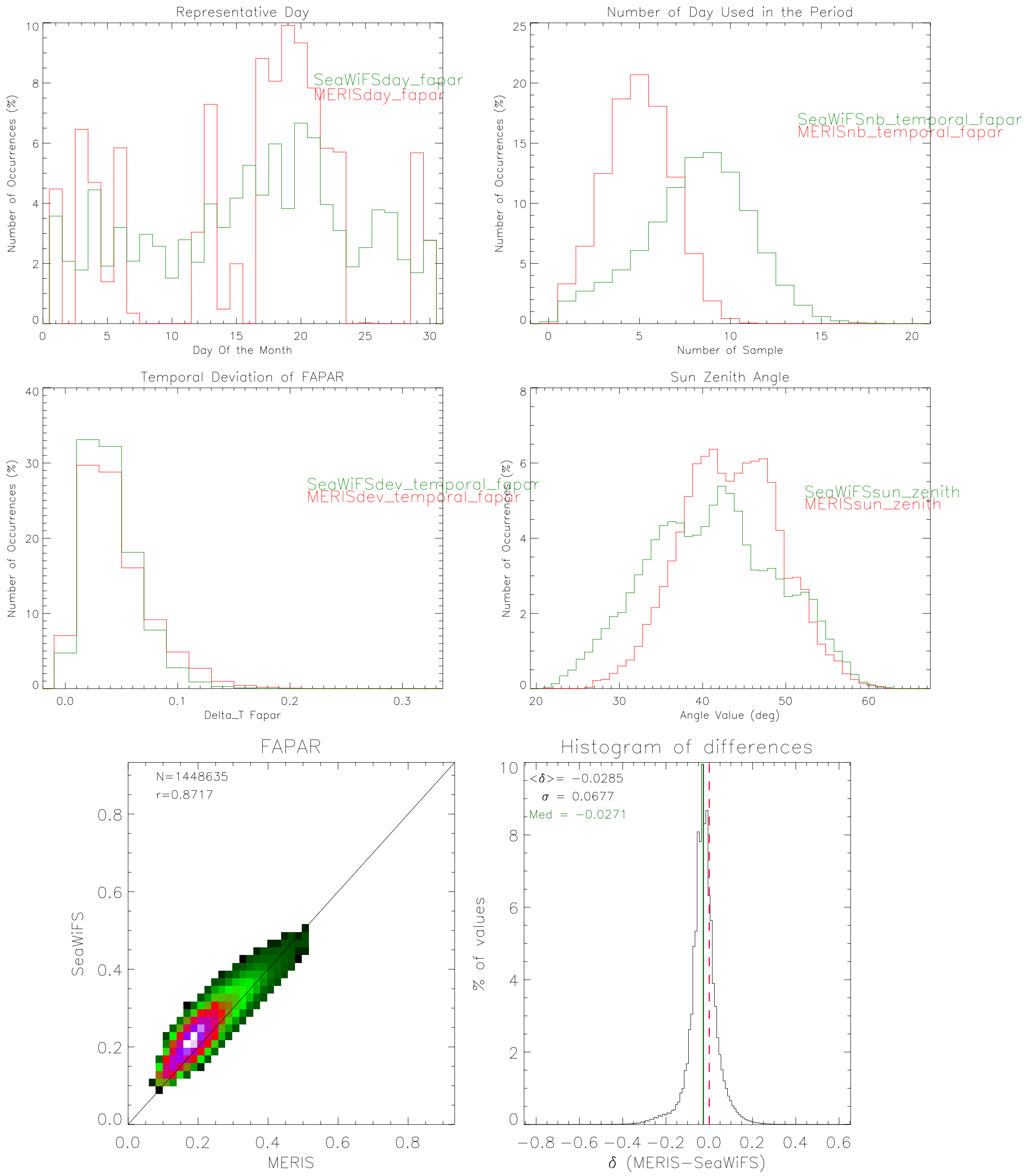

Figure 23: Comparisons between the associated products and FAPAR (bottom panel) when the monthly products derived from MERIS and SeaWiFS are remapped into the LAEA projection. Top panels: Histogram of the representative day of the FAPAR value during the month (left) and of the number of days used in the time-composite algorithm (right). Middle panels: (left) Histogram of the temporal deviation of FAPAR during the month and (right) of the sun zenith angles.

In order to analyse in more details these results we used a new Level-3 product corresponding to the MERIS data at 1.2 km ***remapped*** into the LAEA projection at 2km (no aggregation) and we added the MODIS derived products. These products allow us to compare the 1) the day which has been selected as 'most representative day' 2) the number of day during the period which has been used in the time-composite algorithm as well as 3) the temporal deviation of FAPAR during the time period of the composite as well as the corresponding Sun zenith angle of the selected day. The analyses are made using data acquired in April 2003 with the monthly values.

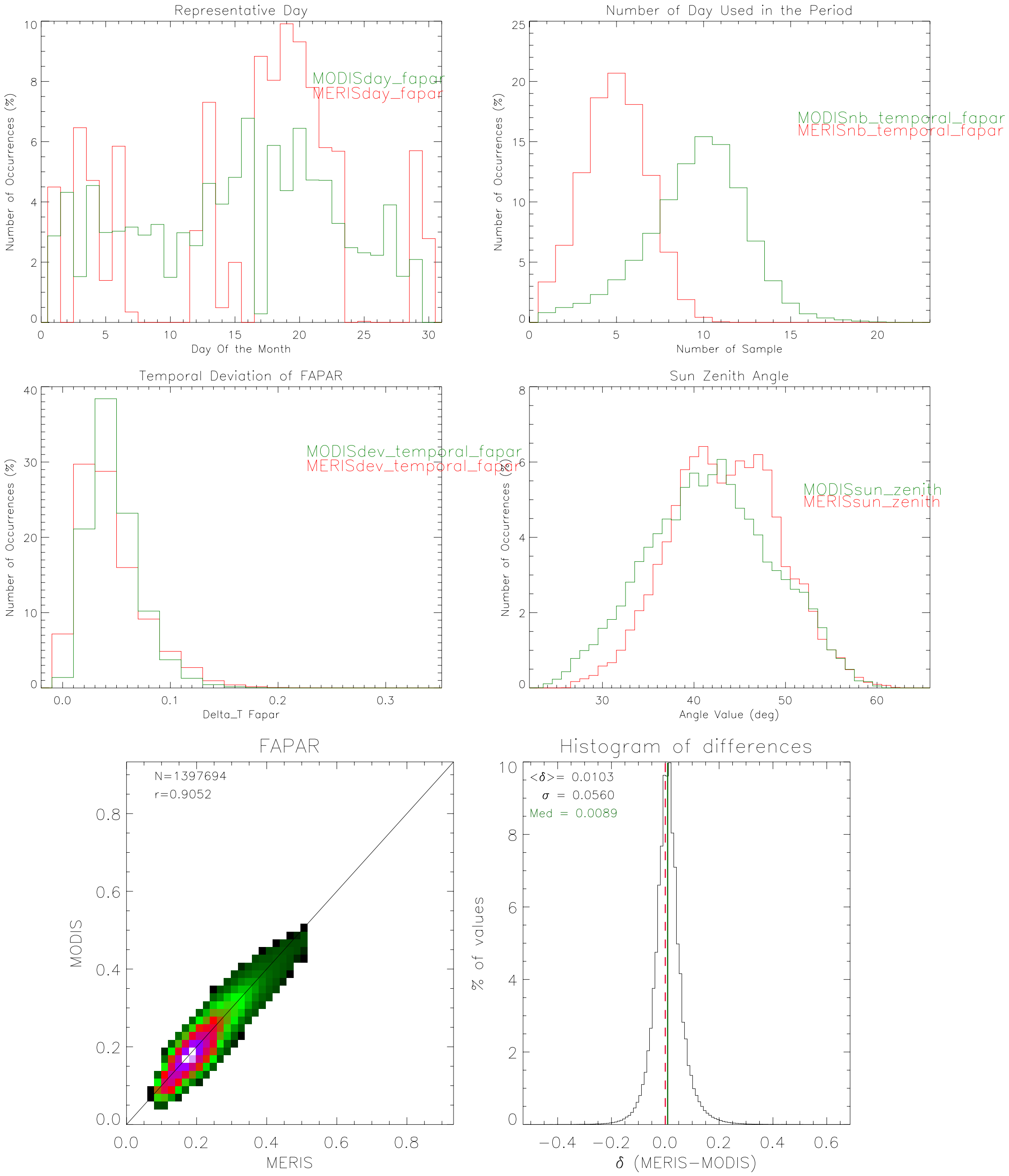

Figure 24: Comparisons between the associated products and FAPAR (bottom panel) when the monthly products derived from MERIS and MODIS are remapped into the LAEA projection. Top panels: Histogram of the representative day of the FAPAR value during the month (left) and of the number of days used in the time-composite algorithm (right). Middle panels: (left) Histogram of the temporal deviation of FAPAR during the month and (right) of the sun zenith angles.

Figure 23 shows the results of comparisons between the MERIS and SeaWiFS products. MERIS FAPAR product is smaller that the one of SeaWiFS with <δ> = -0.0285, which is about the same value than when the Level-3 products were aggregated (<δ> = -0.0248). We can also notice that the values of the representative day cover all the days of the month for SeaWiFS but not for MERIS which can be explained by some missing orbits. The number of acquisition of MERIS during one month over Europe is also lower than with SeaWiFS. The histograms of **the temporal deviation of FAPAR during the month show a median value at about 0.02-0.04** for both instruments with a smaller value for MERIS.

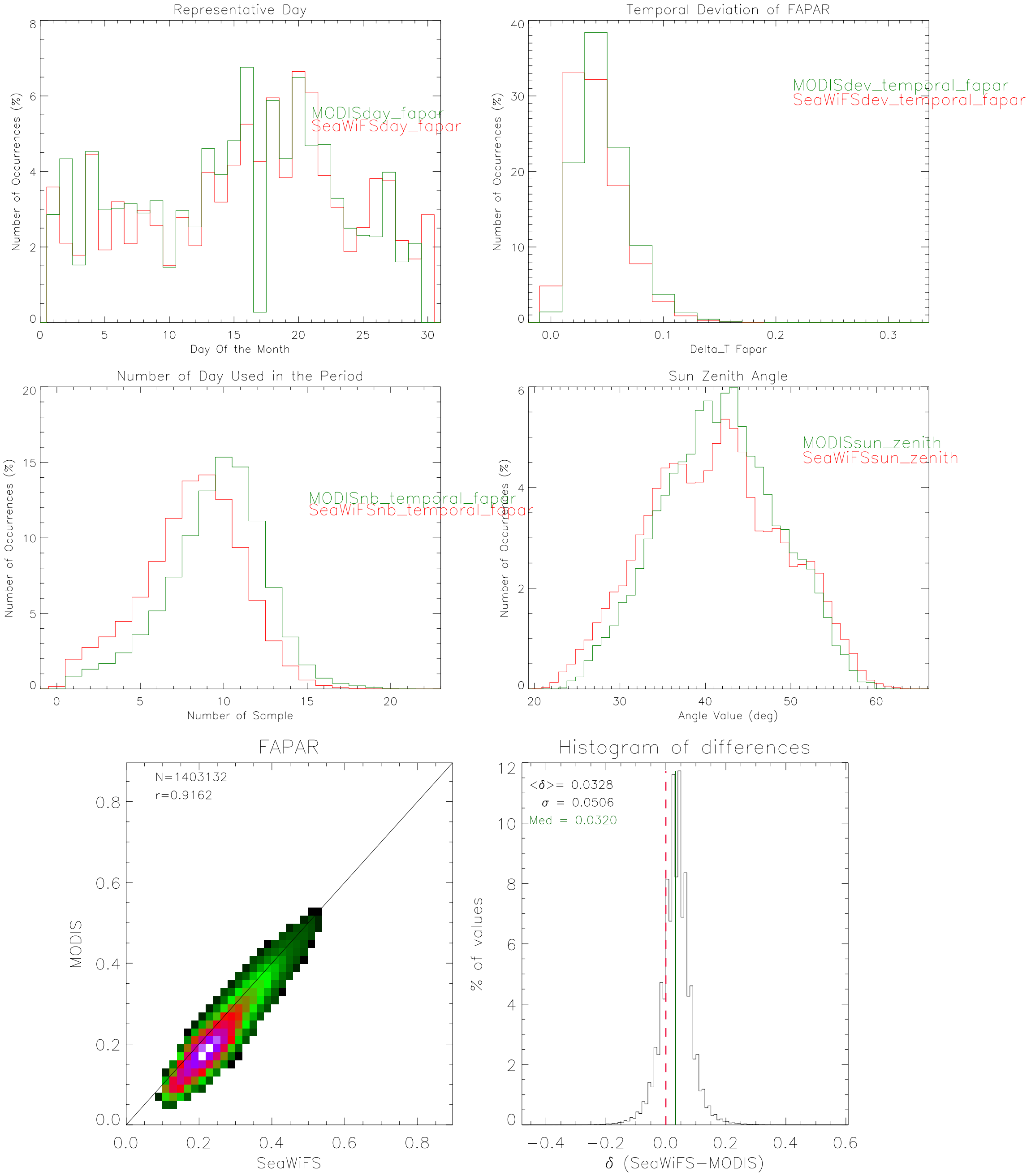

Figure 25: Comparisons between the associated products and FAPAR (bottom panel) when the monthly products derived from SeaWiFS and MODIS are remapped into the LAEA projection. Top panels: Histogram of the representative day of the FAPAR value during the month (left) and of the number of days used in the time-composite algorithm (right). Middle panels: (left) Histogram of the temporal deviation of FAPAR during the month and (right) of the sun zenith angles.

As we already showed with the seasonal variation of illumination, the Sun zenith angle of MERIS is larger than for SeaWiFS. Figure 24 shows the same type of comparisons results between MERIS and MODIS and the same analysis than above can be made: MERIS FAPAR product is smaller than FAPAR MODIS with $<\delta> = 0.0314$ with a correlation coefficient r of about 0.8751. The histogram of number of days shows that we have much more data acquisition for MODIS than for MERIS. If we compare now the SeaWiFS and MODIS results, we obtain a difference averaged value of about -0.0004 with a correlation coefficient of 0.9165. The histograms of both Sun zenith angles and number of representative day show that the acquisition time and number of images are closest than with MERIS.

b. Time series over CarboEurope-IP sites (Annex D)

Figure 72 and Figure 81 illustrate the seasonal cycle of FAPAR over the main CARBOEUROPE-IP sites (http://www.carboeurope.org/) from January 2003 to August 2004 with SeaWiFS products (triangles symbol) and from January 2003 to July 2005 with MERIS (dots) for which the months at the beginning of year 2004 are missing. Each year is represented by a color: red for 2003, pink for 2004 and purple for 2005. The comparison is made with monthly FAPAR products of averaged values over 3x3 pixels around the central pixel. It means that the values which are plotted are averaged spatially over dates which can be different: see the time-composite algorithm.

In general, both FAPAR products are in a good agreement and the seasonal cycles from the two products provide consistent information with same shape as function of the seasons. Typical seasonal variations from one year to another with one instrument is well retrieved when no change have affected the vegetation. Moreover, both sensor products show lower values in summer 2003 comparing to 2004, or the inverse, which means that both sensor products detect change in the same order of level. In the case of MERIS products, values at the beginning of 2005 demonstrate that levels of FAPAR are comparable to the ones in 2003 over the particular sites of Castelporziano and Lavarone.

c. Time series over ground validation sites

The JRC-FAPAR products derived from the SeaWiFS instrument have been compared against ground-based estimation of FAPAR over various EOS validation sites listed in Table 9. These sites have been categorized into various radiative transfer regimes to assess the sources of errors of the measurements and the results are published in [16].

EOS Site of Validation	Ground-estimations year	Sensor in same year	Sensors for 2003
Agro (Bondville)	2000	SeaWiFS 2.17 km MOS 500 m MODIS 1 km MISR 275 m	SeaWiFS MERIS
Konza Prairie	2000	SeaWiFS 2.17 km MOS 500 m MODIS 1 km	SeaWiFS MERIS

Here, we propose to add other sources of remote sensing data when available as well as the FAPAR derived from MERIS in 2003 by assuming that the vegetation activity during a seasonal cycle has not changed from the specific year where ground estimations are available. Annex E summarizes the data which have been used in the analysis.

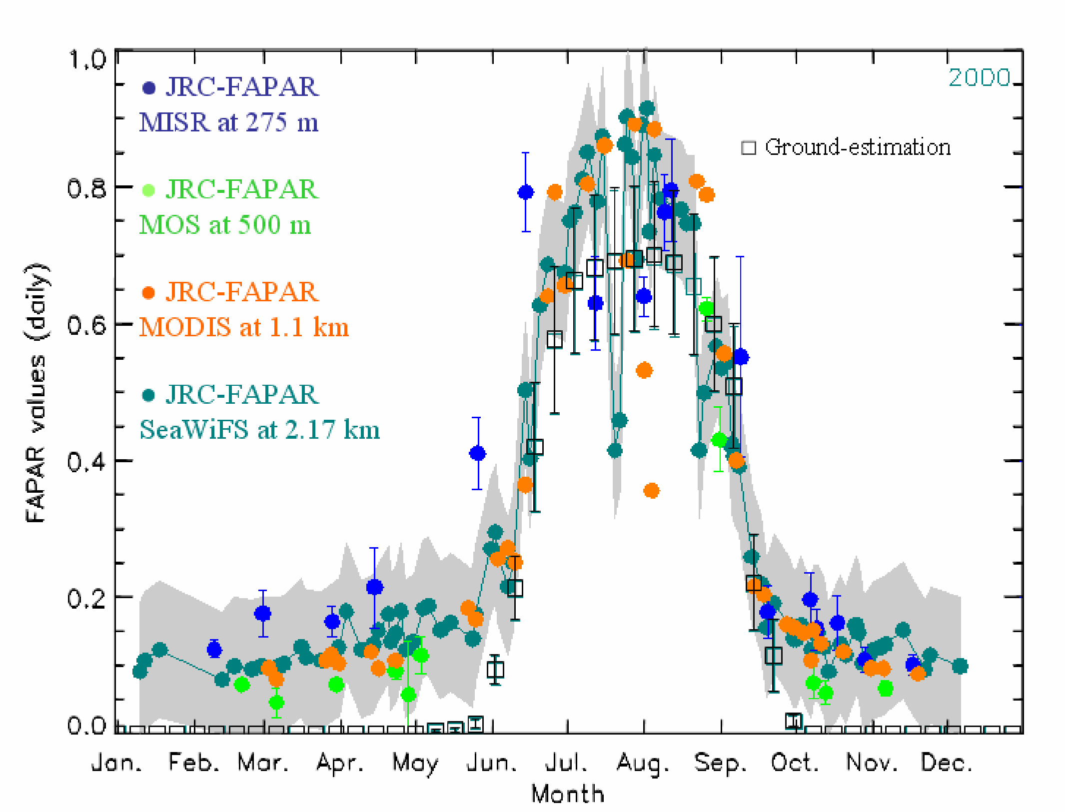

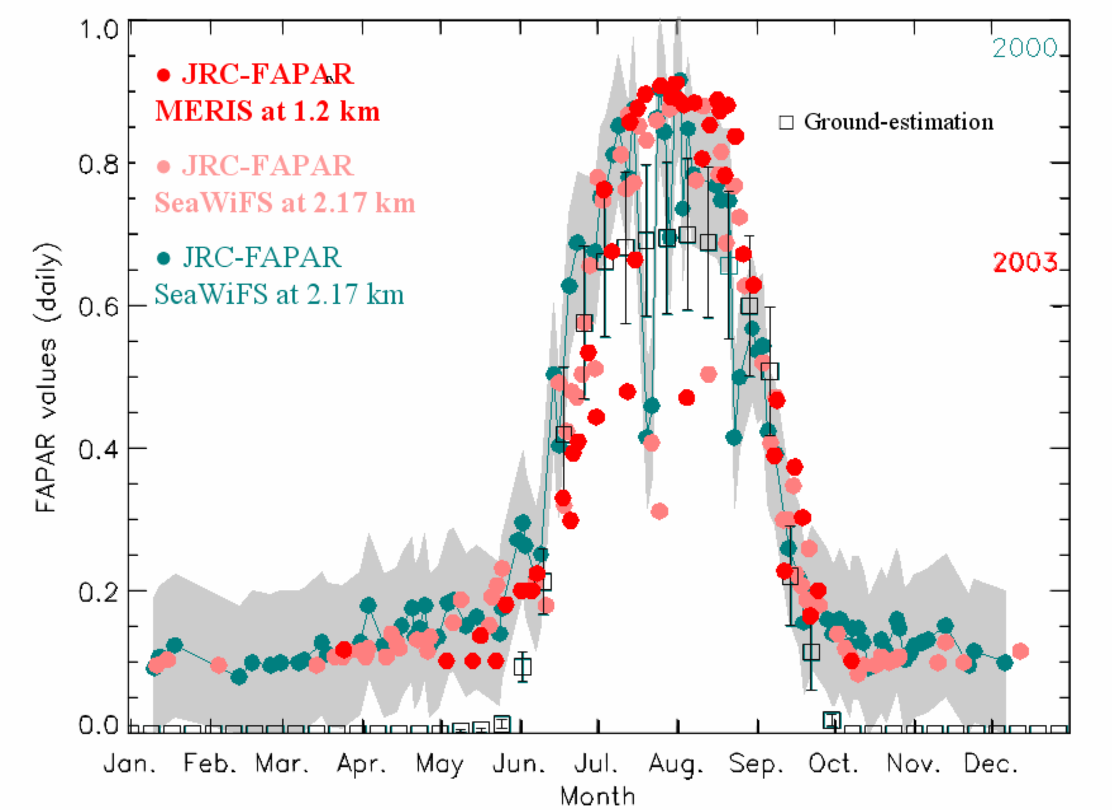

Figure 26: Comparisons of ground-based FAPAR estimations profiles (black empty square symbols) and instantaneous daily JRC-FAPAR products (full circle symbols) over the site of AGRO in 2000 (top panel) with data of MERIS and SeaWiFS in 2003 (bottom panel). The zone shaded in grey delineates the ±0.1 uncertainty range around the FAPAR JRC-products. The vertical bars indicate the uncertainty range around the ground-based estimations or around the central pixel in case of MISR and MOS instrument.

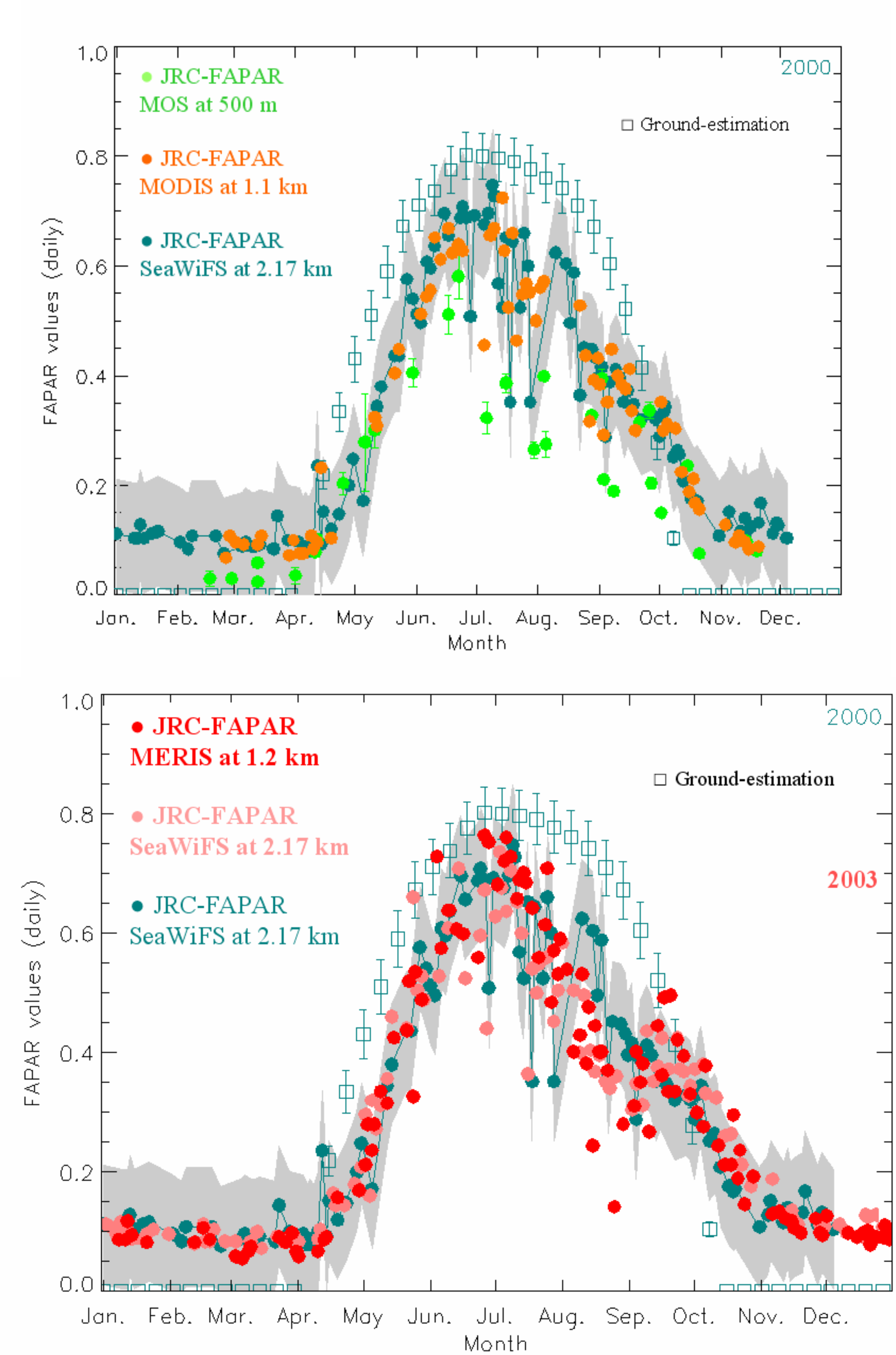

Figure 27: Comparisons of ground-based FAPAR estimations profiles (black empty square symbols) and instantaneous daily JRC-FAPAR products (full circle symbols) over the site of Konza prairie in 2000 (top panel) with data of MERIS and SeaWiFS in 2003 (bottom panel). The zone shaded in grey delineates the ±0.1 uncertainty range around the FAPAR JRC-products. The vertical bars indicate the uncertainty range around the ground-based estimations or around the central pixel in case of MOS instrument.

8. Conclusions

We found that there is a small bias between the FAPAR derived from MERIS (i.e. MGVI) and those derived from SeaWiFS or MODIS when comparing daily regional products. This difference and, the level, is however not systematic and depends on the geographical regions selected to perform the inter-comparisons. The differences can be explained by the uncertainties at the level of radiances, since it has been shown that the differences of "inter-calibration" between SeaWiFS and MERIS can be propagated to differences on the products.

At the level of monthly products (Level 3) the scatter-plots show better agreements because the outliers, that can be due to cloud and cloud shadows, have been removed and the differences are somewhat smoother. This illustrates that the time-composite technique for constructing Level-3 products and applied here provides a consistency between the two sets of FAPAR products during one year over Europe.

Investigations have been conducted to evaluate if the illumination and observation geometries can explain the differences. We reach the conclusion that the differences in geometries do not lead to the differences between the products.

We also compare the FAPAR products against "ground-based estimations" values over two types of vegetation and show that the discrepancy between two sensors products are anyway always smaller than when compared against the "ground-estimations" of FAPAR.

9. Recommendations

The validation of the MGVI products should continue **during the life time of the instrument** in order to assess the quality of the land surface products which also depends on the processing version on the Level 1 data. The inter-comparison was essentially conducted here with the first processing version data. This requires **further analysis with new reprocessing data** (**MEGS-PC/7.4**) to better understand the small difference especially at the daily level. The use of full resolution (FR) MERIS Level 2 products is also required to confirm the RR results.

This type of work has also permitted us to assess the performance of the algorithm itself (different sensors provide a comparable biophysical product) and the **merging of the geophysical products** coming from different sensors can be therefore achieved in order to provide more complete products to the scientific communities regarding their spatial coverage.

The **time-composite technique** is also very important in order to conserve the statistical distribution of both compositing and daily values at various spatial and temporal resolutions. The maximum value technique used by other agencies implies systematic bias to higher values of the geophysical products.

Validation of the biophysical products is essential to establish their accuracies to the scientific communities aiming at the assimilation of RS products. Both comparisons with ground-based estimates and generation of global products would help to provide uncertainties associated to the spatial resolution of products. The comparison against same type of products derived either from past, contemporary or future instruments, also permits us to assess any technical drift (like calibration) of sensors. However, the in-situ based estimates have to be clearly defined in term of methodology of measurements (protocol) and definition. Again the MERIS FR Level 2 products would also be requested to continue the validation against ground-based estimates.

10. Acknowledgements

Frédéric Mélin provided daily Level 2 and Level 3 SeaWiFS FAPAR products.
The MERIS data have been processed and delivered by Ludovic Bourg (ACRI), Olga Faber from Brockmann's consult and Fabrice Brito (ESRIN). We thank Paul Snoeij for his comments on the work which has been done during this contract. The remarks of Michael Rast, Philippe Goryl and Peter Regner during the final presentation helped to improve this final report document.
Ophélie Aussedat was financially supported by this project.

11. References

[1] GOVAERTS, Y., VERSTRAETE, M. M., PINTY, B. AND GOBRON, N., 1999: Designing Optimal Spectral Indices: A Feasibility and Proof of Concept Study, *International Journal of Remote Sensing*, **20**, pp. 1853-1873.
[2] GOBRON, N., PINTY, B., VERSTRAETE, M. M. AND GOVAERTS Y., 1999: The MERIS Global Vegetation Index (MGVI): Description and Preliminary Application, *International Journal of Remote Sensing*, **20**, pp. 1917-1927.
[3] GOBRON, N., PINTY, B., VERSTRAETE, M.M, AND WIDLOWSKI, J.-L., 2000: Advanced Vegetation Indices Optimized for Up-Coming Sensors: Design, Performance, and Applications. *IEEE Transactions on Geoscience and Remote Sensing*, **38**, pp. 2489-2505.
[4] GOBRON, N., MÉLIN, F., PINTY, B., VERSTRAETE, M. M., WIDLOWSKI, J.-L. AND BUCINI, G., 2001: A Global Vegetation Index for SeaWiFS: Design and Applications. In: Beniston M. and Verstraete M. M. (eds.)**:** Remote Sensing and Climate Modeling: Synergies and Limitations, pp. 5-21 Kluwer Academic, Dordrecht.
[5] PINTY, B., WIDLOWSKI, J.-L., GOBRON, N., VERSTRAETE, M. M. AND DINER, D. J. 2002: Uniqueness of Multiangular Measurements Part 1: An Indicator of Subpixel Surface Heterogeneity from MISR, *IEEE Transactions on Geoscience and Remote Sensing, MISR Special Issue*, **40**, 1560-1573.
[6] GOBRON, N., PINTY, B., VERSTRAETE, M. M., WIDLOWSKI, J.-L. AND DINER, D. J. 2002: Uniqueness of Multiangular Measurements Part 2: Joint Retrieval of Vegetation Structure and Photosynthetic Activity from MISR, *IEEE Transactions on Geoscience and Remote Sensing, MISR Special Issue*, **40**, 1574-1592.
[7] GOBRON, N., PINTY, B., VERSTRAETE, M. M. AND TABERNER, M. 2002: Global Land Imager (GLI) - An optimized FAPAR Algorithm - Theoretical Basis Document, *Institute for Environment and Sustainability*, EUR REPORT **NO. 20147 EN**, 19 PP.
[8] GOBRON, N., AUSSEDAT, O., AND PINTY, B. 2006: Moderate Resolution Imaging Spectroradiometer (MODIS) Optimized JRC-FAPAR Algorithm - Theoretical Basis Document, *Institute for Environment and Sustainability*, EUR REPORT **NO. 22164 EN**, 19 PP.
[9] PINTY, B., GOBRON, N., MÉLIN, F. AND VERSTRAETE, M. M., 2002: A Time Composite Algorithm Theoretical Basis Document, *Institute for Environment and Sustainability*, EUR Report **No. 20150 EN**, 8 pp.

[10] Aussedat O., Gobron, N., Pinty, B. and Taberner, M. 2006: MERIS Level 3 Land Surface Time Composite Product Description, *Institute for Environment and Sustainability*, EUR Report **No. 22165 EN**, 17 pp.

[11] http://www-loa.univ-lille1.fr/Hdflook/hdflook_gb.html

[12] Gobron, N., Pinty, B., Mélin, F., Taberner, M. and Verstraete, M. M., 2002: Sea Wide Field-of-View Sensor (SeaWiFS) - An Optimized FAPAR Algorithm - Theoretical Basis Document, *Institute for Environment and Sustainability*, EUR Report **No. 20148 EN**, 20 pp.

[13] Gobron, N., Mélin, F., Pinty, B., Taberner, M. and Verstraete, M. M., 2005: MERIS/ENVISAT biophysical land products: Validation and performance, Advances in Space Research, **doi:10.1016/j.asr.2003.07.079**.

[14] Rahman, H., Verstraete, M. M. and Pinty, B. 1993: Coupled surface-atmosphere reflectance (CSAR) model. 1. Model description and inversion on synthetic data, *Journal of Geophysical Research*, **98**, 20,779-20,789.

[15] Mélin, F., Steinich, C., Gobron, N., Pinty, B. and Verstraete, M. M., 2002: Optimal merging of LAC and GAC data from SeaWiFS, *International Journal of Remote Sensing*, **23**, pp. 801-807.

[16] Gobron, N., Pinty, B., Aussedat, O., Chen, O., Cohen, W. B., Fensholt, R., Gond, V., Huemmrich, K. F., Lavergne, T., Mélin, T., Privette, J. L., Sandholt, I,. Taberner, M., Turner, D. P., Verstraete, M. M. and Widlowski, J.-L. 2006: Evaluation of FAPAR products for different canopy radiation transfer regimes: Methodology and results using JRC products derived from SeaWiFS against ground-based estimations', *Journal of Geophysical Research, DOI.* 10.1029/2005JD006511.

12. List of figures

13. List of tables

14. ANNEX A: Results of comparison between instantaneous FAPAR derived from single images of MERIS/SeaWiFS/MODIS

These cases studies have been made using MERIS Level 2 processing MEGS-PC/6.1 (ACRI) software.

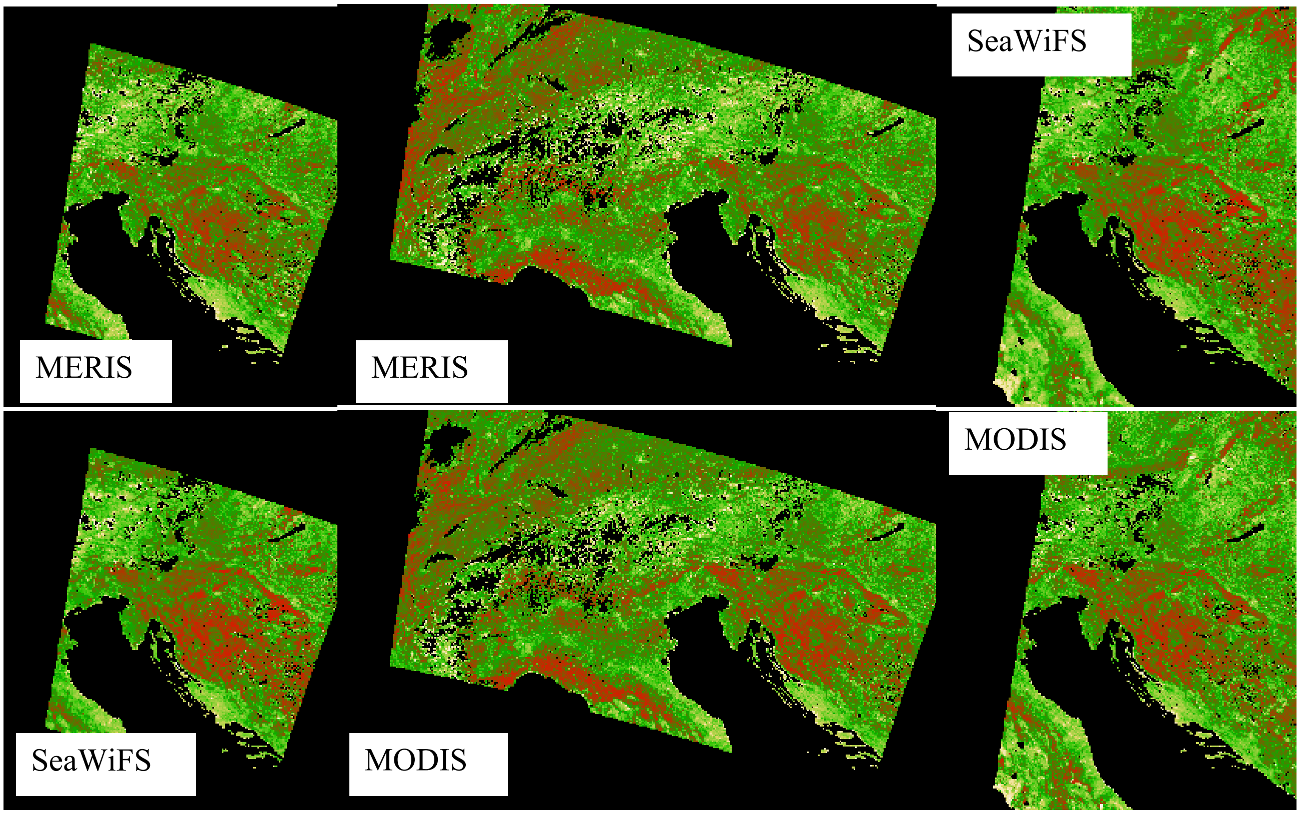

Figure 28: Maps of FAPAR values remapped at 1.2 km for MERIS, SeaWiFS and MODIS. The black pixels correspond to common mask when comparing FAPAR from MERIS/SeaWiFS (left), MERIS/MODIS (middle) and SeaWiFS/MODIS (right) over **AAOT**.

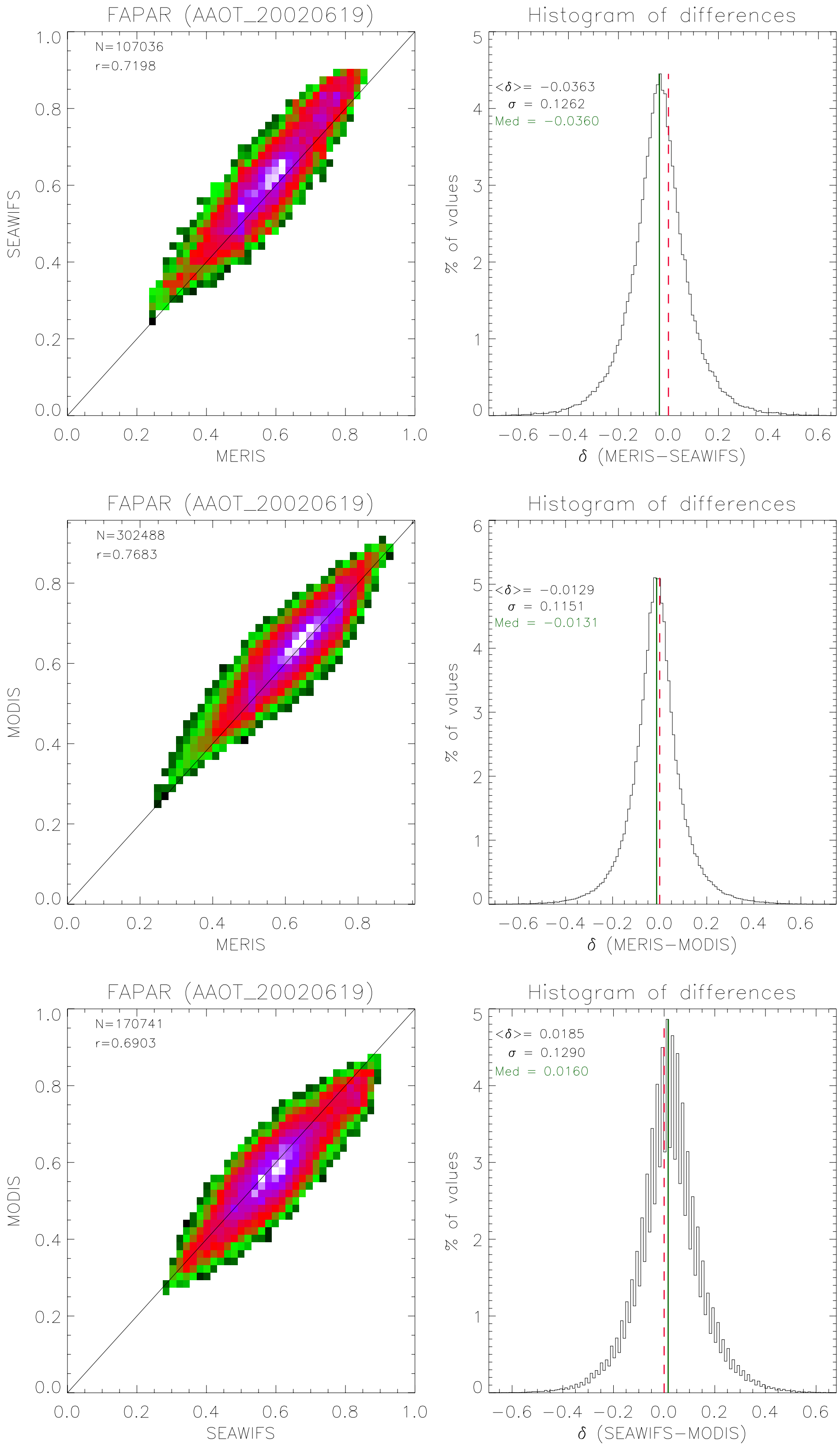

Figure 29: Scatter-plots and histogram of difference between FAPAR values remapped at 1.2 km derived from MERIS, SeaWiFS and MODIS over **AAOT**. N indicates the number of pixels, r the correlation, <δ> the mean of differences, σ the standard deviation and med the median value of the differences.

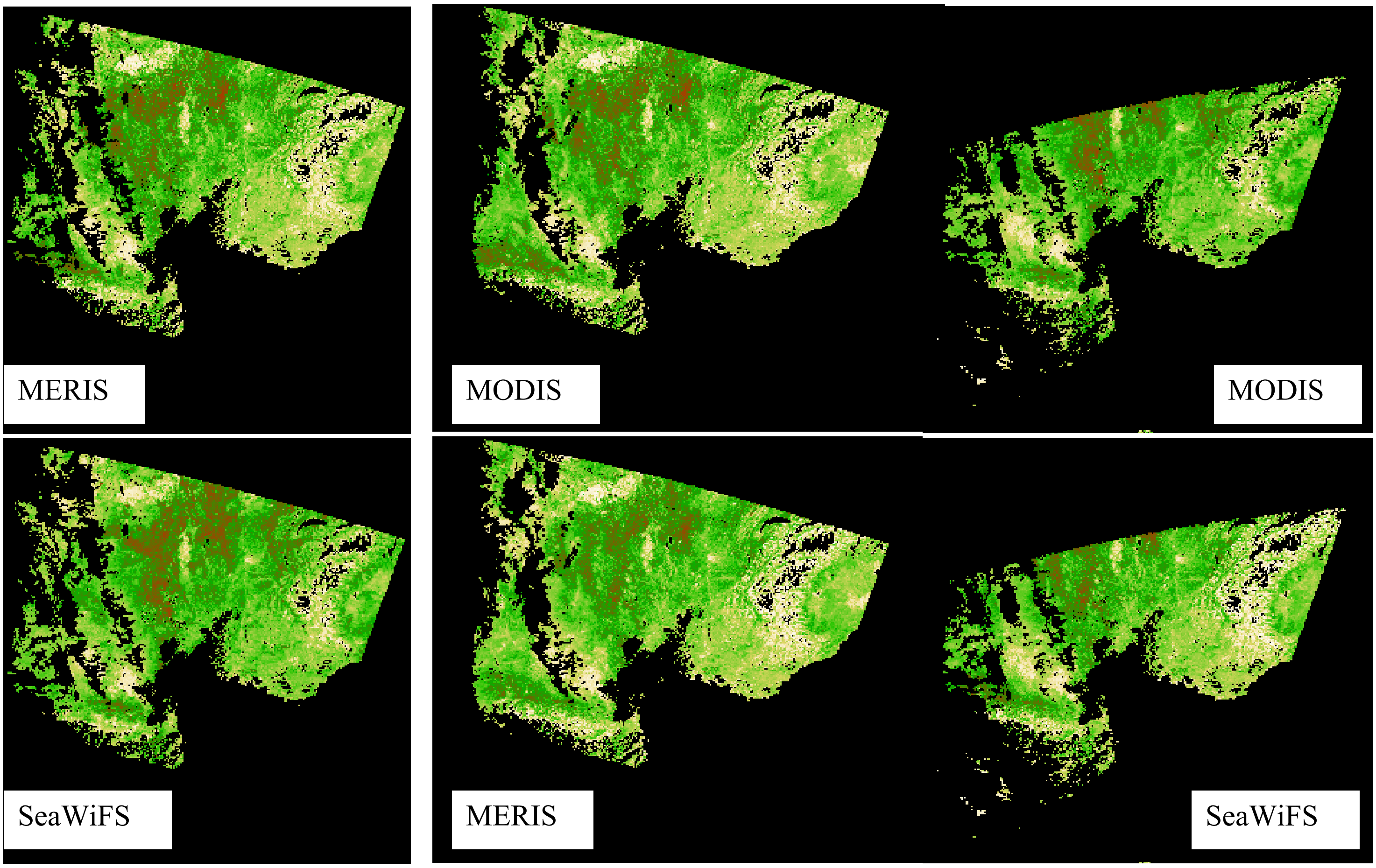

Figure 30: Maps of FAPAR values remapped at 1.2 km for MERIS, SeaWiFS and MODIS. The black pixels correspond to common mask when comparing FAPAR from MERIS/SeaWiFS (left), MERIS/MODIS (middle) and SeaWiFS/MODIS (right) over **Aeronet**.

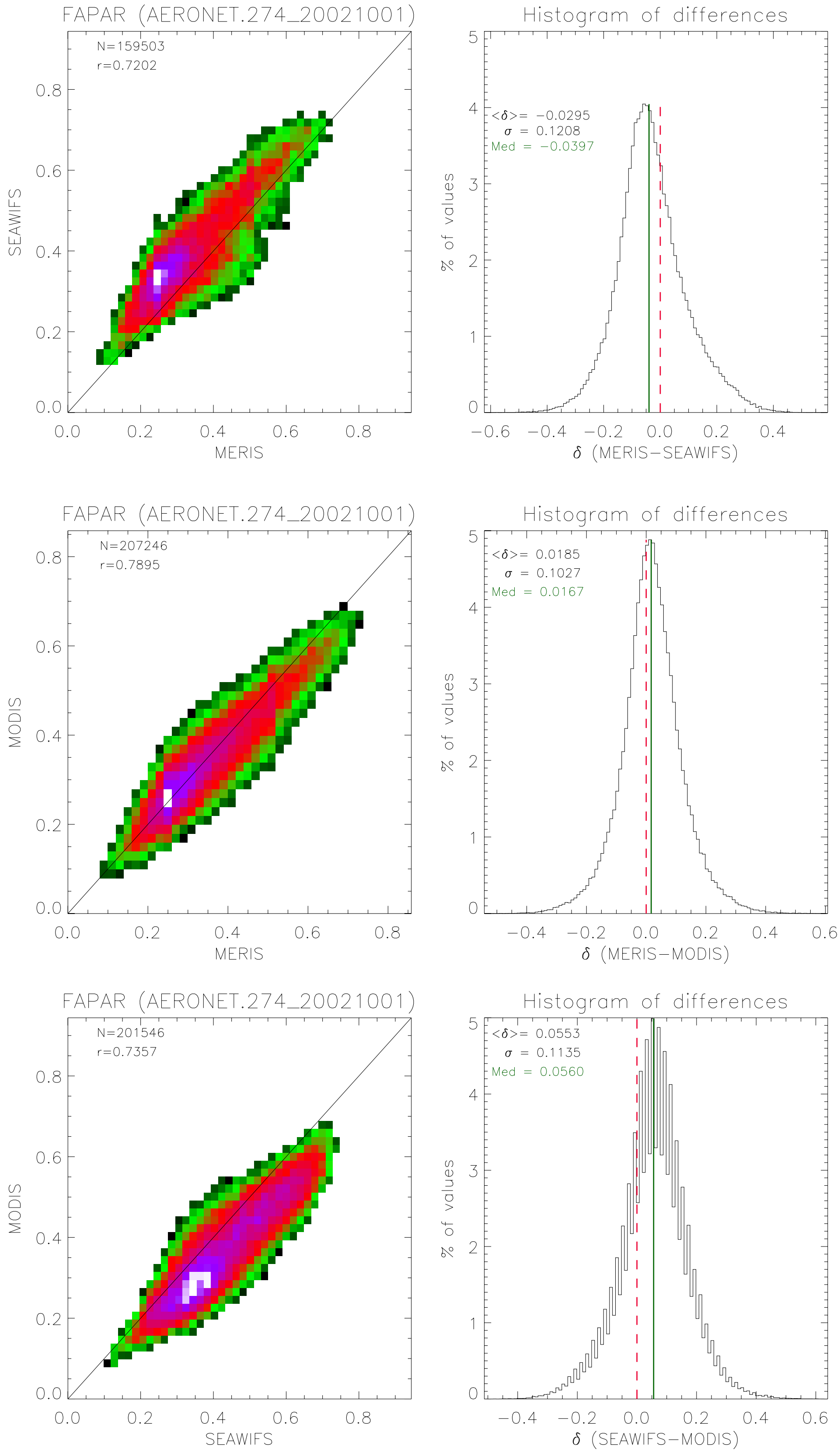

Figure 31: Scatter-plots and histogram of difference between FAPAR values remapped at 1.2 km derived from MERIS, SeaWiFS and MODIS over Aeronet. N indicates the number of pixels, r the correlation, <δ> the mean of differences, σ the standard deviation and med the median value of the differences.

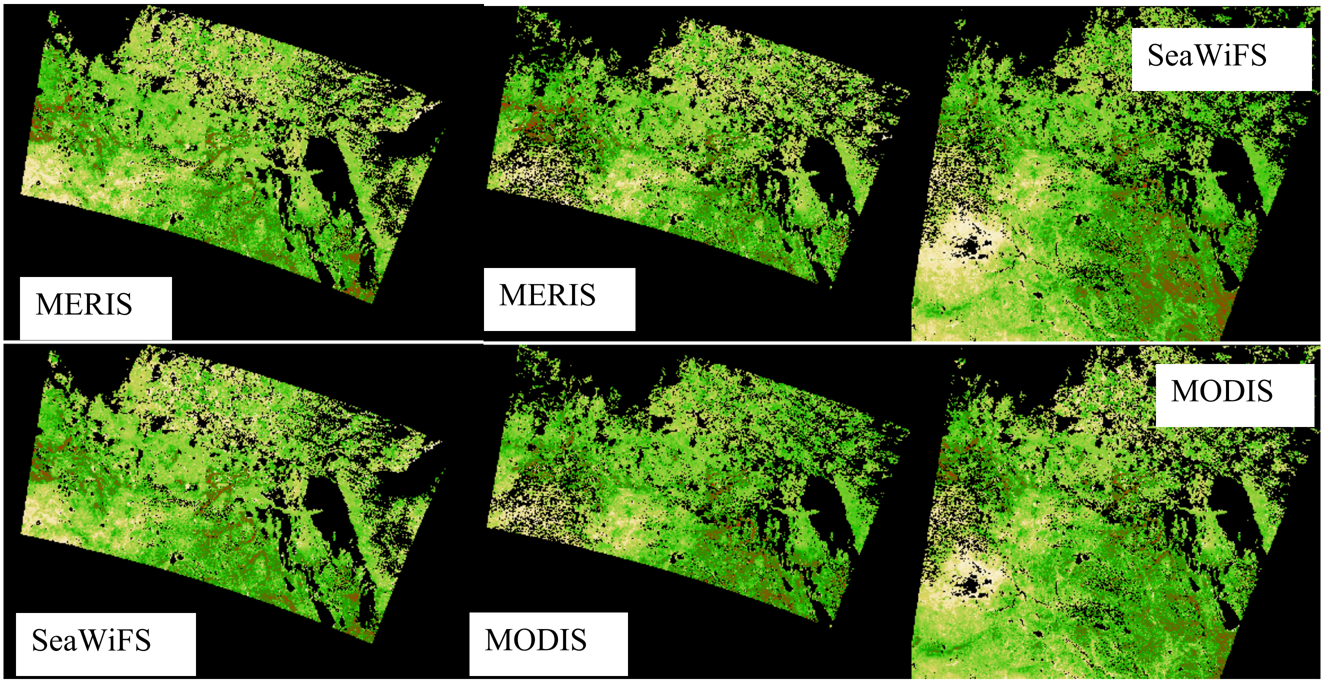

Figure 32: Maps of FAPAR values remapped at 1.2 km for MERIS, SeaWiFS and MODIS. The black pixels correspond to common mask when comparing FAPAR from MERIS/SeaWiFS (left), MERIS/MODIS (middle) and SeaWiFS/MODIS (right) over **BOREAS**.

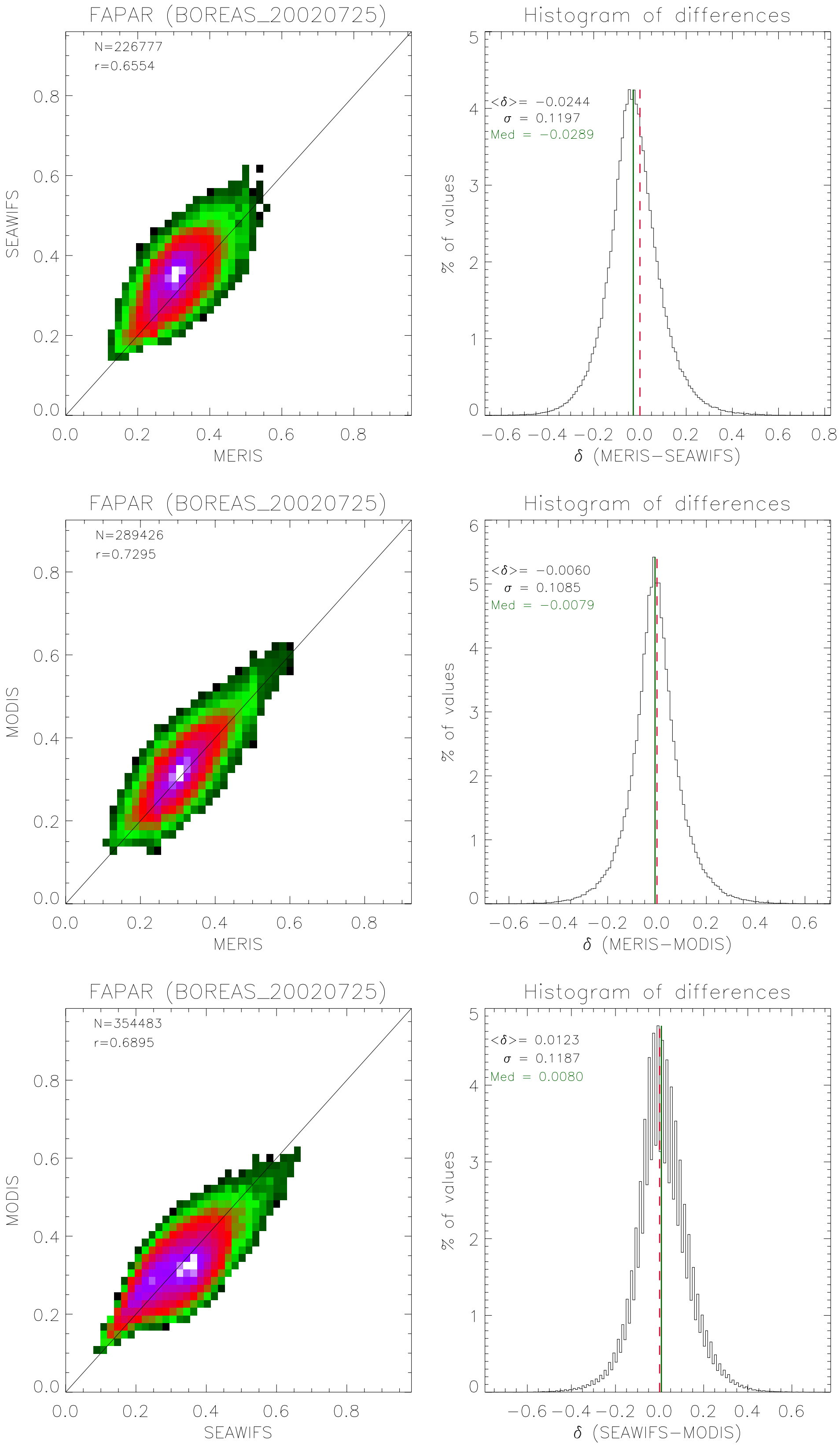

Figure 33: Scatter-plots and histogram of difference between FAPAR values remapped at 1.2 km derived from MERIS, SeaWiFS and MODIS over BOREAS. N indicates the number of pixels, r the correlation, <δ> the mean of differences, σ the standard deviation and med the median value of the differences.

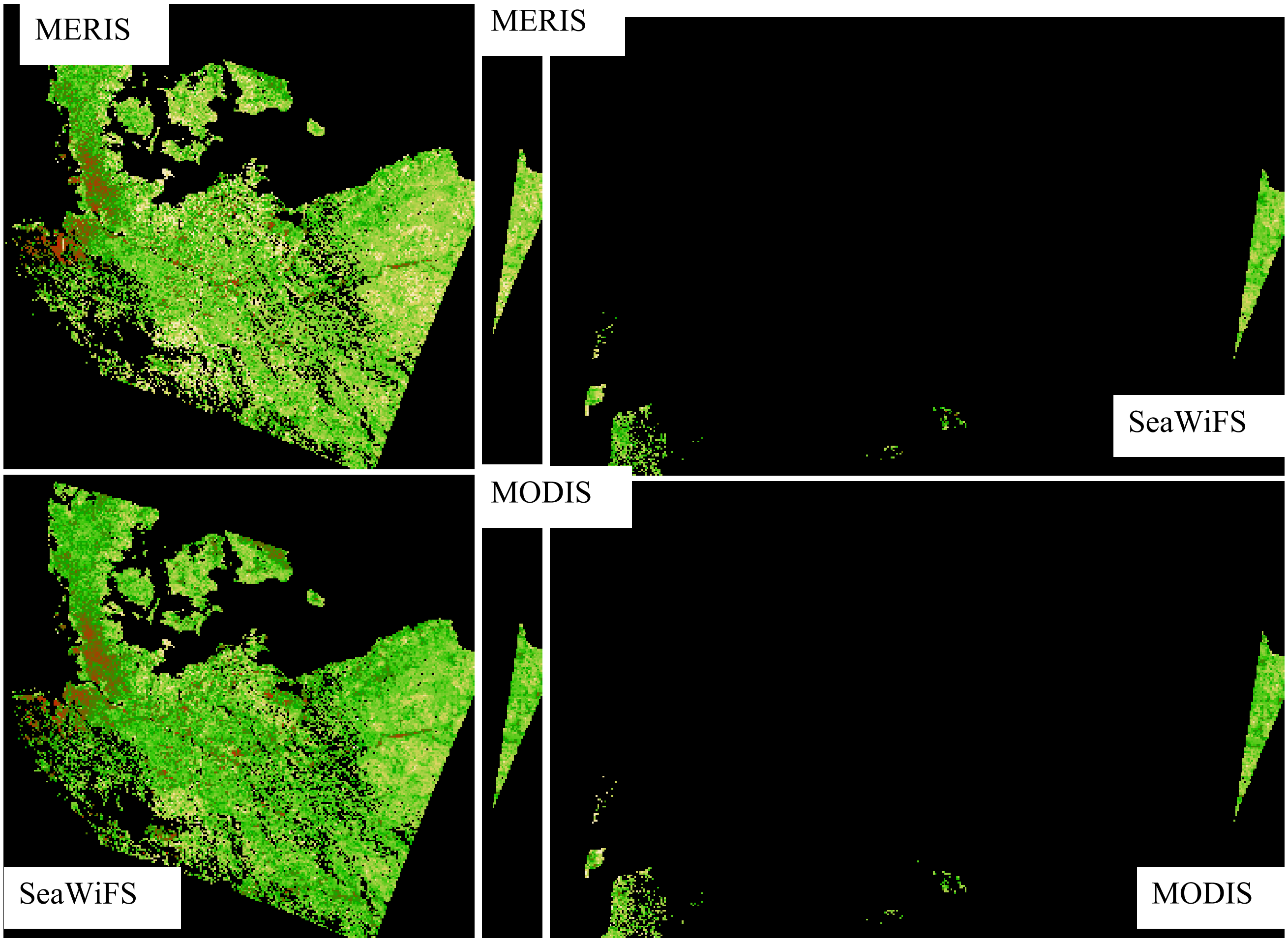

Figure 34: Maps of FAPAR values remapped at 1.2 km for MERIS, SeaWiFS and MODIS. The black pixels correspond to common mask when comparing FAPAR from MERIS/SeaWiFS (left), MERIS/MODIS (middle) and SeaWiFS/MODIS (right) over **GEESTHACHT**_233.

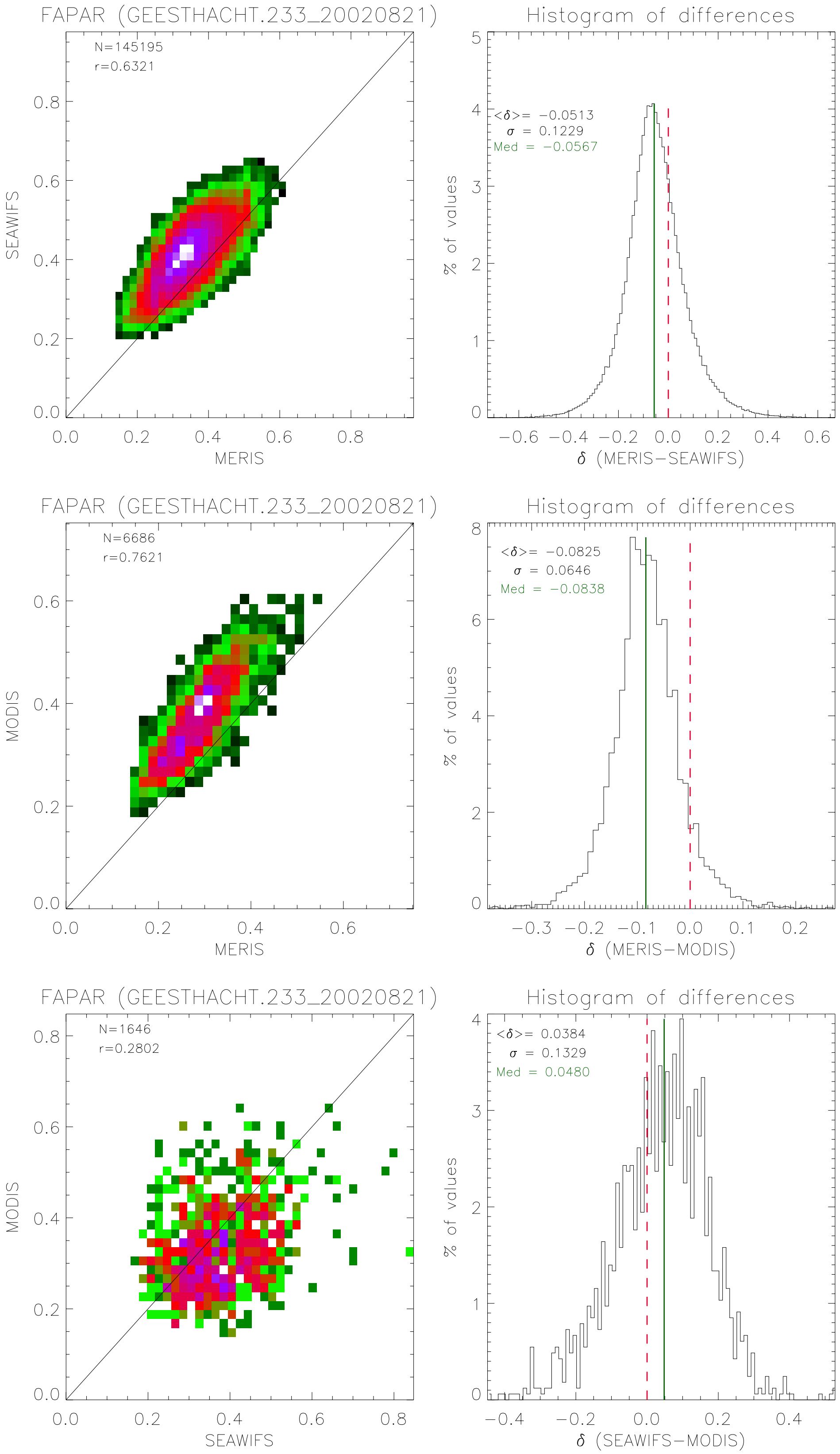

Figure 35: Scatter-plots and histogram of difference between FAPAR values remapped at 1.2 km derived from MERIS, SeaWiFS and MODIS over **GEESHACHT**_233. N indicates the number of pixels, r the correlation, <δ> the mean of differences, σ the standard deviation and med the median value of the differences.

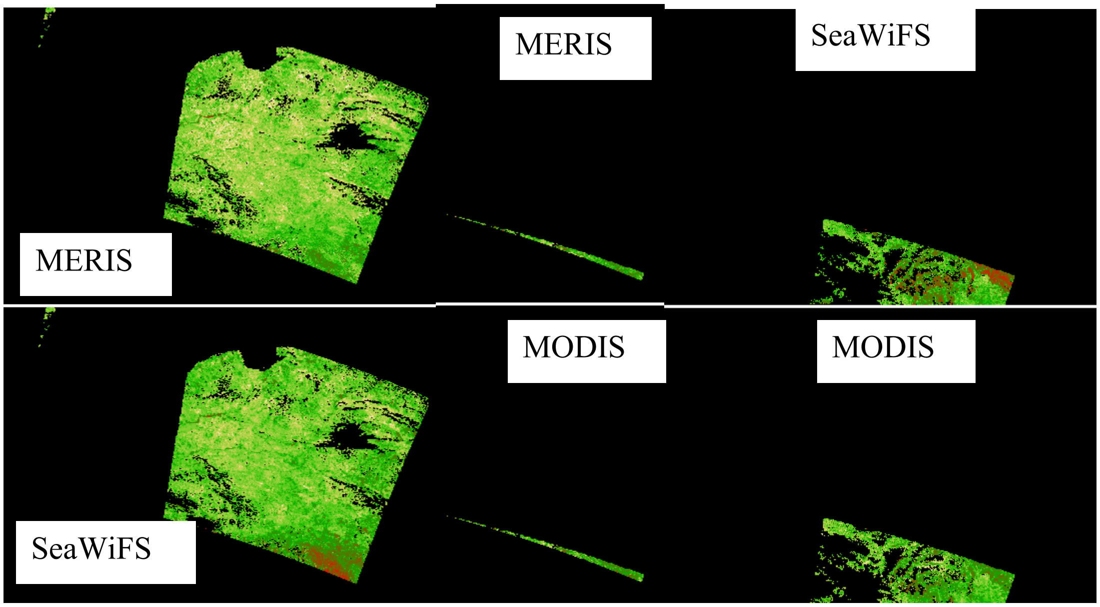

Figure 36: Maps of FAPAR values remapped at 1.2 km for MERIS, SeaWiFS and MODIS. The black pixels correspond to common mask when comparing FAPAR from MERIS/SeaWiFS (left), MERIS/MODIS (middle) and SeaWiFS/MODIS (right) over **GEESTHACHT**_234.

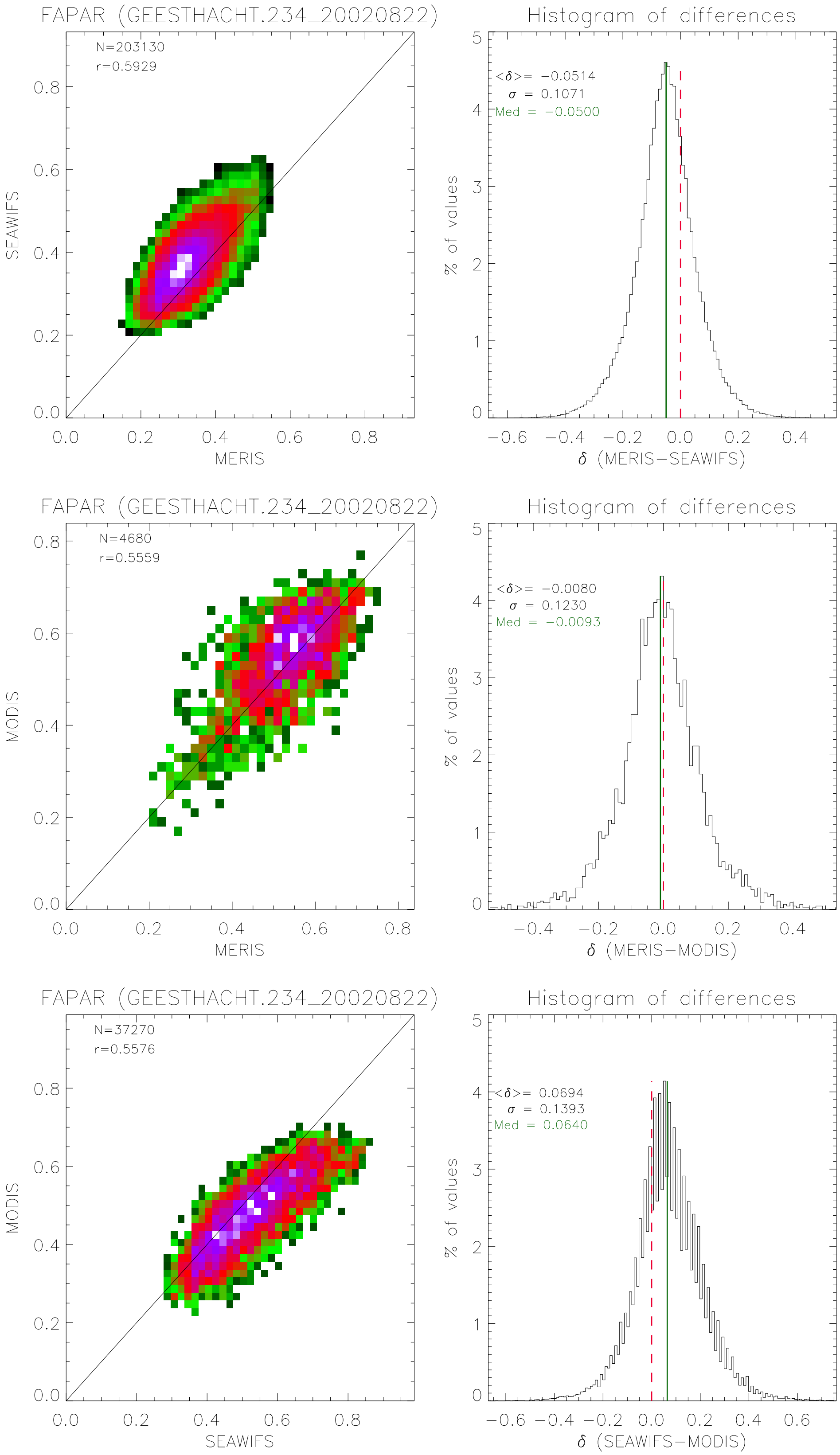

Figure 37: Scatter-plots and histogram of difference between FAPAR values remapped at 1.2 km derived from MERIS, SeaWiFS and MODIS over **GEESHACHT**_234. N indicates the number of pixels, r the correlation, <δ> the mean of differences, σ the standard deviation and med the median value of the differences.

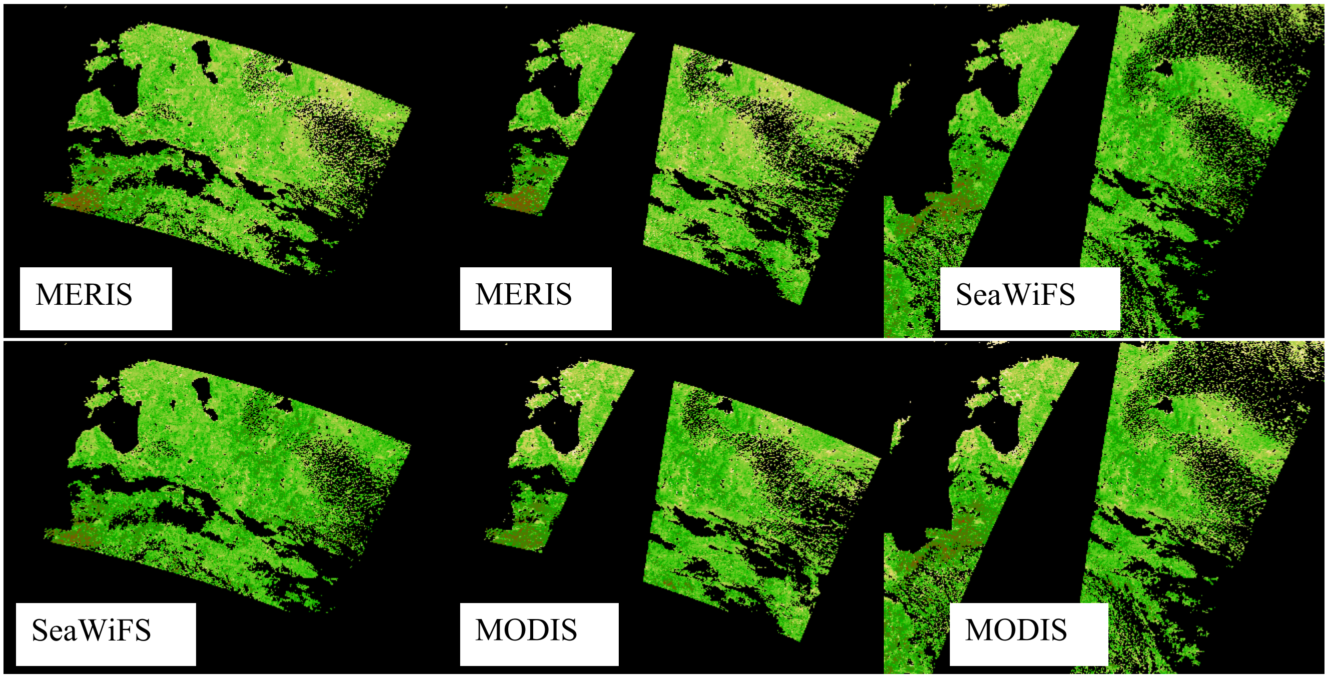

Figure 38: Maps of FAPAR values remapped at 1.2 km for MERIS, SeaWiFS and MODIS. The black pixels correspond to common mask when comparing FAPAR from MERIS/SeaWiFS (left), MERIS/MODIS (middle) and SeaWiFS/MODIS (right) over **STATION**_271.

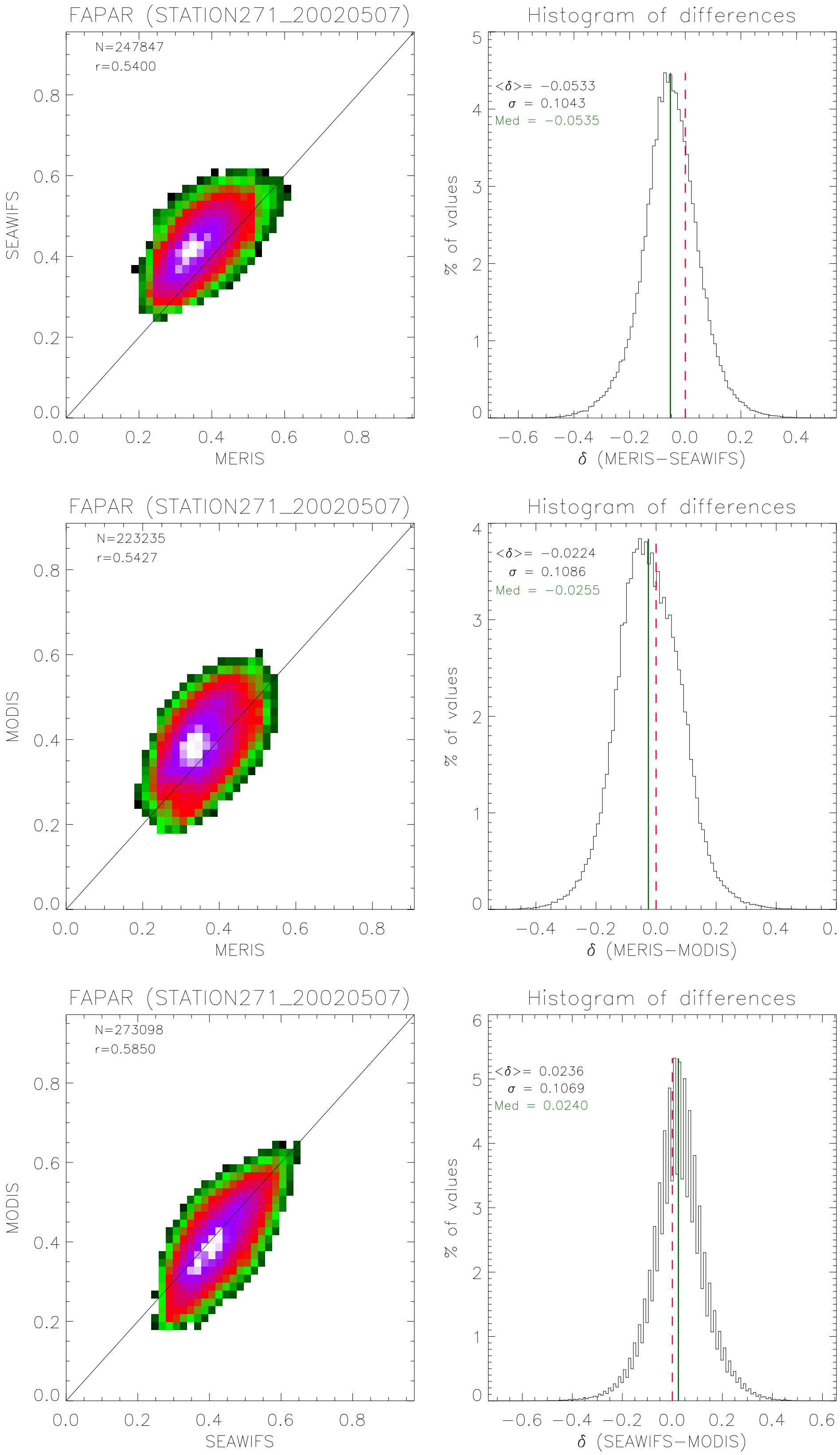

Figure 39: Scatter-plots and histogram of difference between FAPAR values remapped at 1.2 km derived from MERIS, SeaWiFS and MODIS over **STATION**_271. N indicates the number of pixels, r the correlation, <δ> the mean of differences, σ the standard deviation and med the median value of the differences.

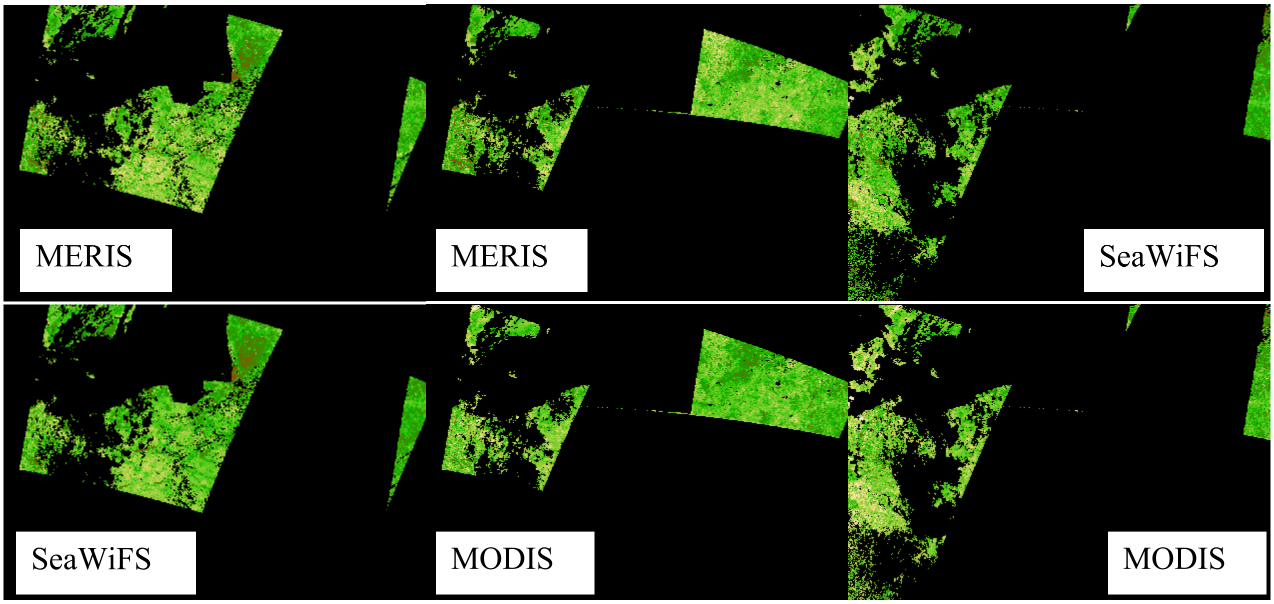

Figure 40: Maps of FAPAR values remapped at 1.2 km for MERIS, SeaWiFS and MODIS. The black pixels correspond to common mask when comparing FAPAR from MERIS/SeaWiFS (left), MERIS/MODIS (middle) and SeaWiFS/MODIS (right) over **STATION**_114.

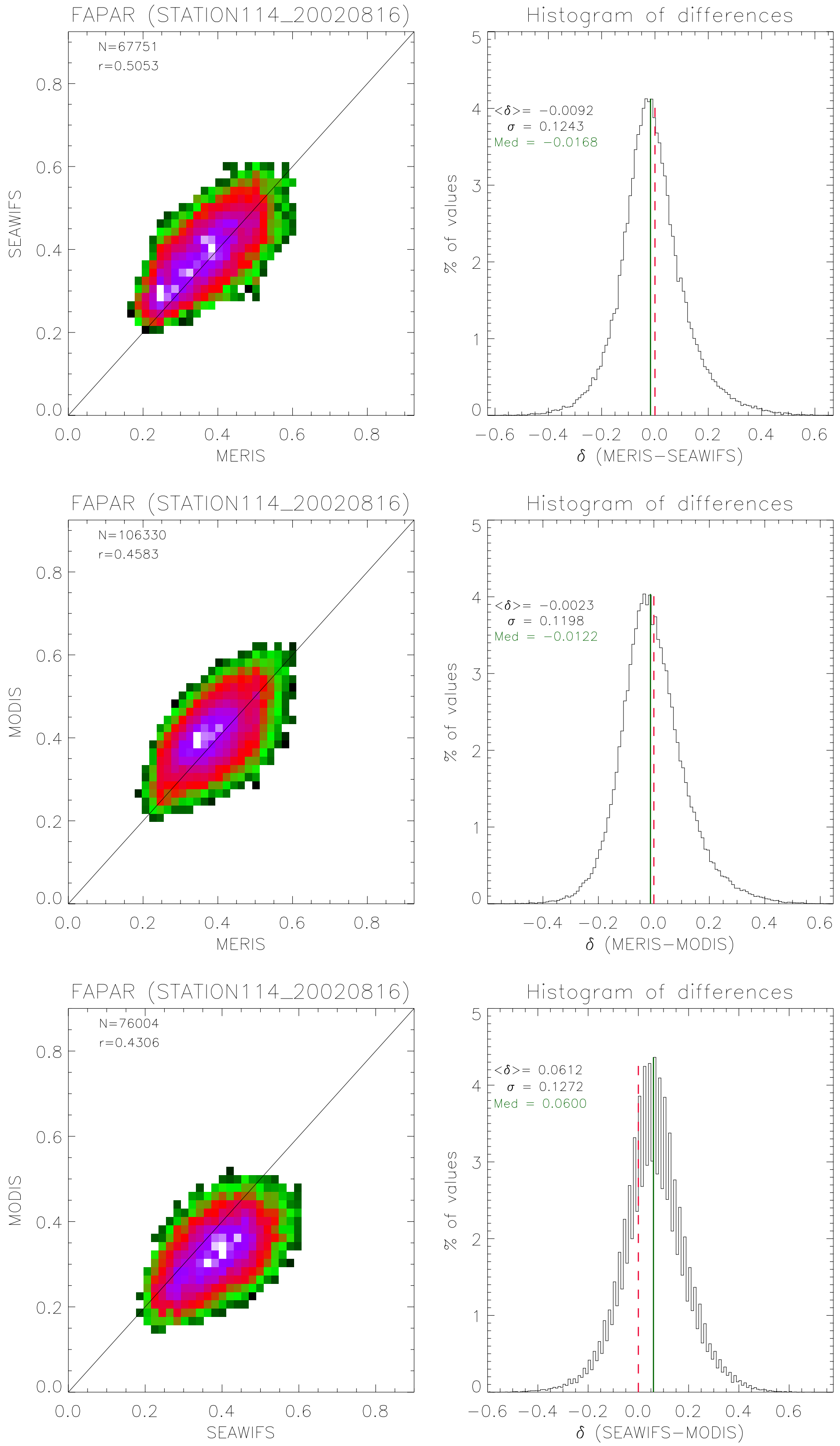

Figure 41: Scatter-plots and histogram of difference between FAPAR values remapped at 1.2 km derived from MERIS, SeaWiFS and MODIS over **STATION**_114. N indicates the number of pixels, r the correlation, <δ> the mean of differences, σ the standard deviation and med the median value of the differences.

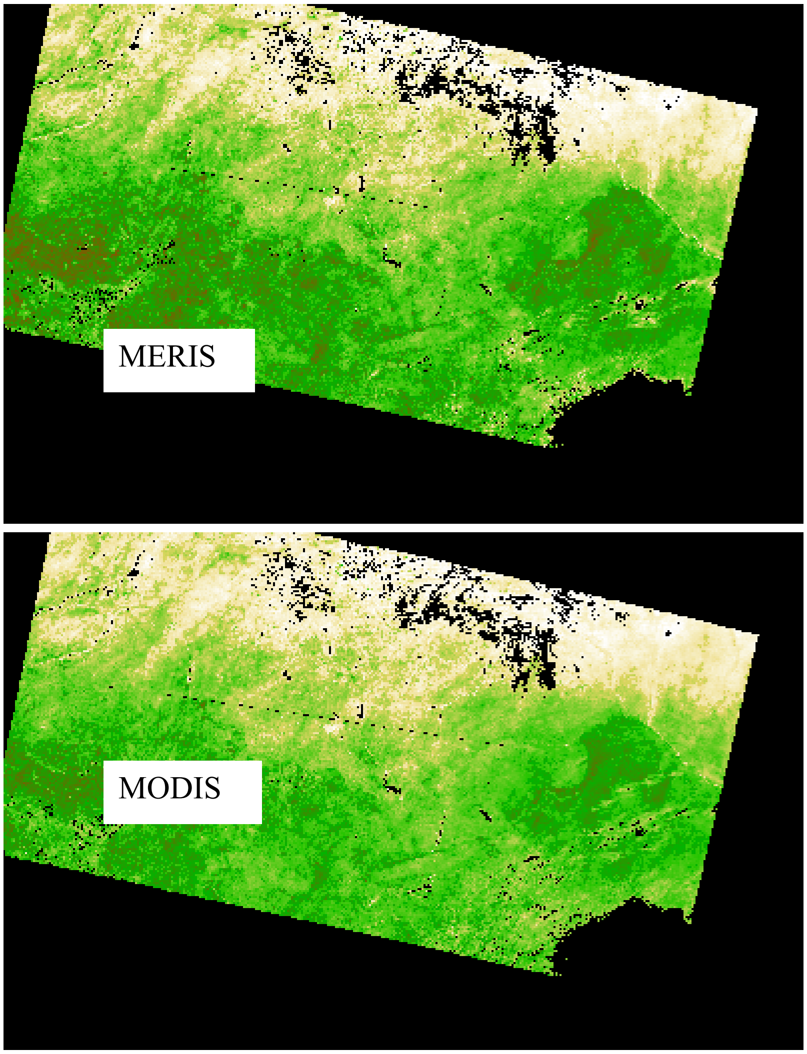

Figure 42: Maps of FAPAR values remapped at 1.2 km for MERIS and MODIS. The black pixels correspond to common mask when comparing FAPAR from MERIS/MODIS over **OUADADOUGOU**.

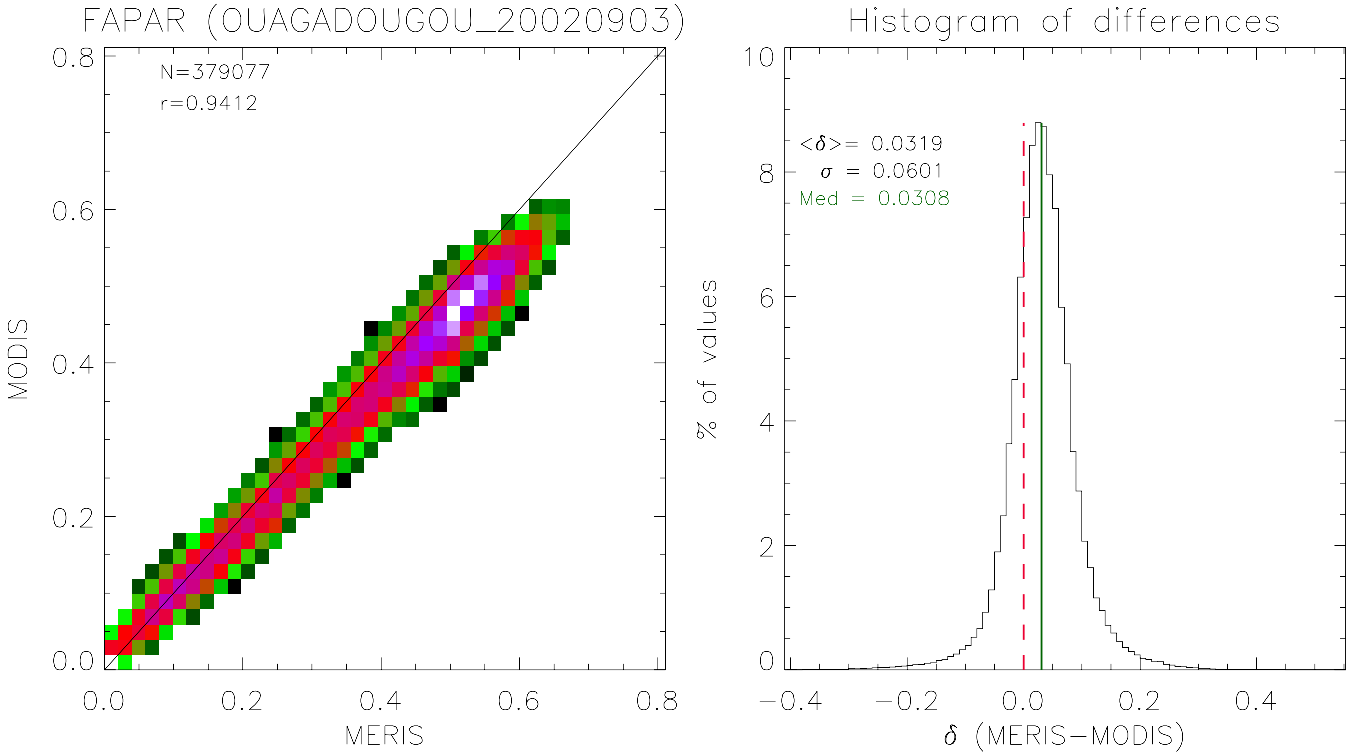

Figure 43: Scatter-plots and histogram of difference between FAPAR values remapped at 1.2 km derived from MERIS and MODIS over **OUAGADOUGOU**. N indicates the number of pixels, r the correlation, <δ> the mean of differences, σ the standard deviation and med the median value of the differences.

15. ANNEX B: Results of comparison between instantaneous FAPAR derived from single images of MERIS (reprocessed data) /SeaWiFS/MODIS.

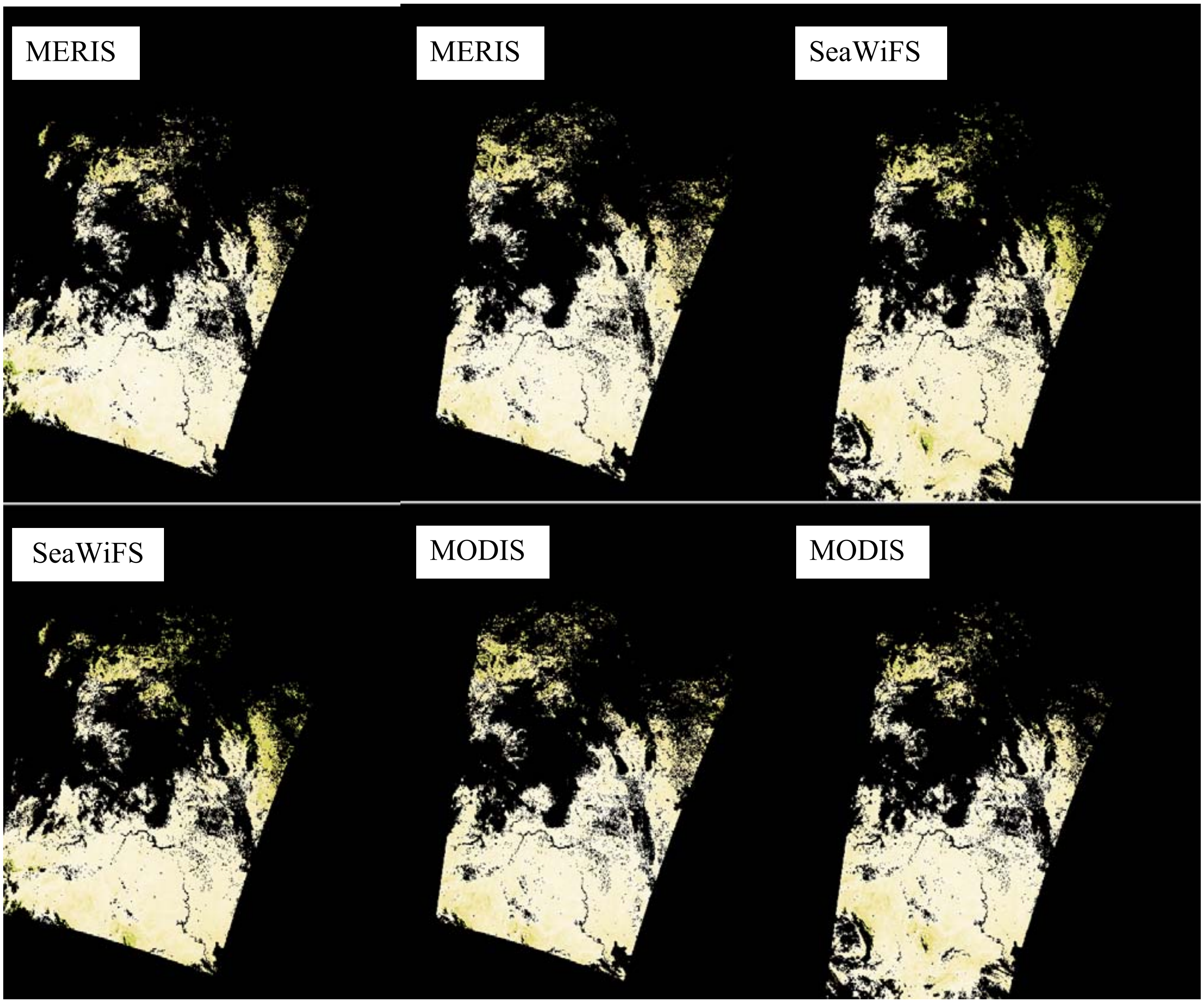

Figure 44: Maps of FAPAR values remapped at 1.2 km for MERIS/SeaWiFS (left panel), MERIS/MOIS (middle panel) and SeaWiFS /MODIS (right panel) over **BOREASSSA**. The black pixels correspond to common mask when comparing FAPAR derived from two instruments.

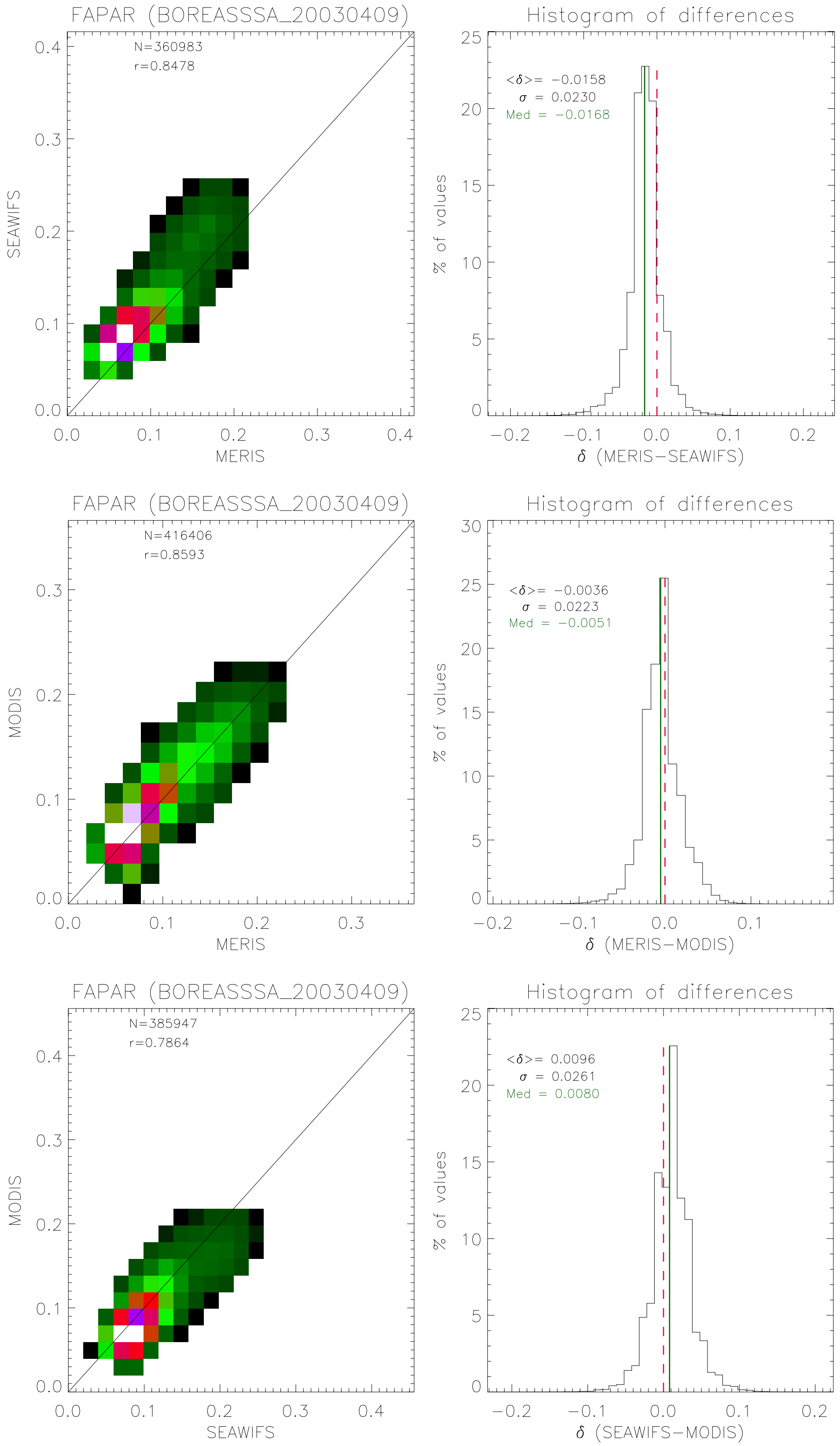

Figure 45: Scatter-plots and histogram of difference between FAPAR values remapped at 1.2 km derived from MERIS/SeaWiFS, MERIS/MODIS and SeaWiFS/MODIS over **BOREASSSA**. N indicates the number of pixels, r the correlation, <δ> the mean of differences, σ the standard deviation and med the median value of the differences.

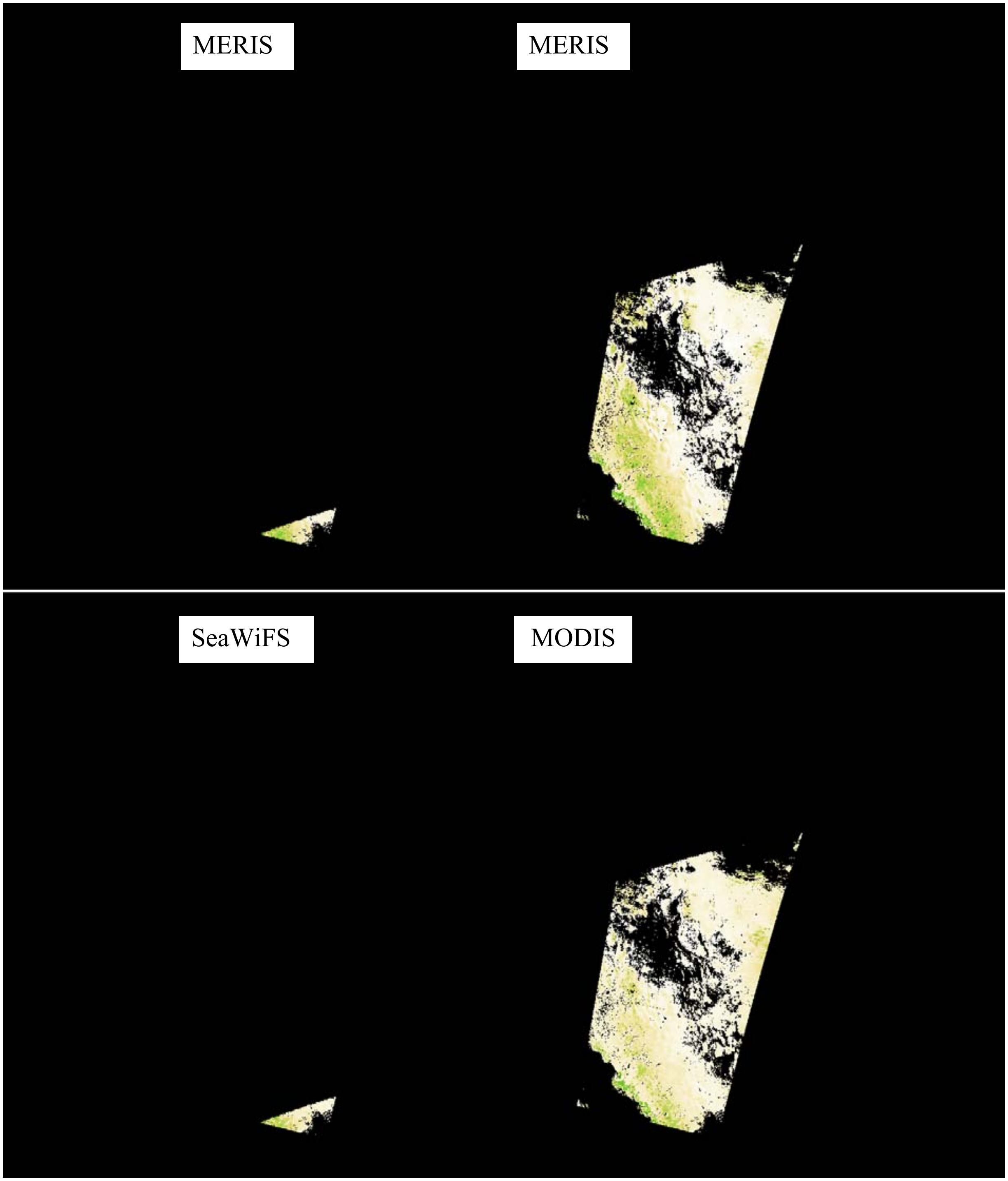

Figure 46: Maps of FAPAR values remapped at 1.2 km for MERIS/SeaWiFS (left panel) and MERIS/MODIS (right panel) over **JORNADA** (2003/01/01). The black pixels correspond to common mask when comparing FAPAR derived from two instruments.

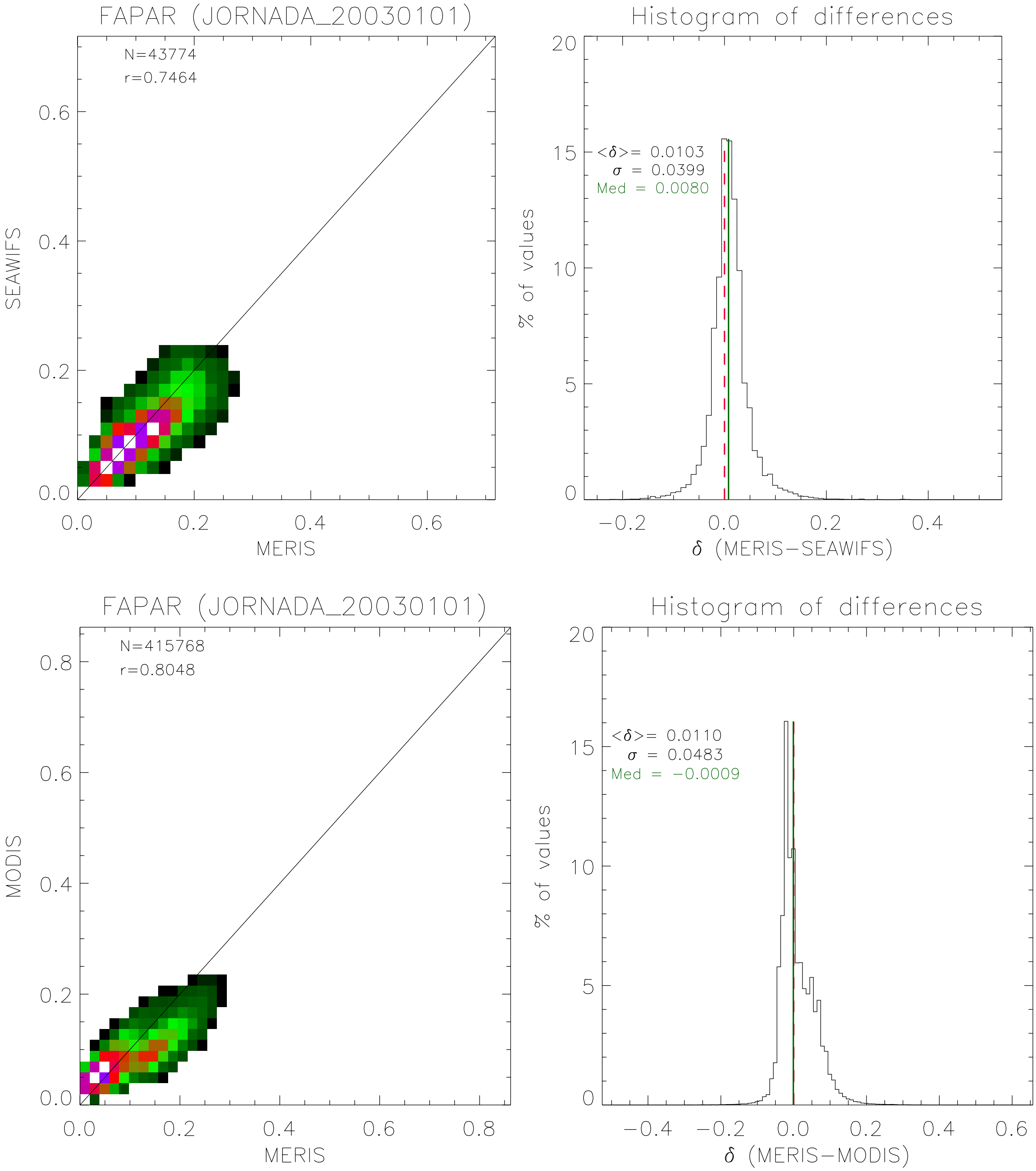

Figure 47: Scatter-plots and histogram of difference between FAPAR values remapped at 1.2 km derived from MERIS/SeaWiFS and MERIS/MODIS over **JORNADA** (2003/01/01). N indicates the number of pixels, r the correlation, <δ> the mean of differences, σ the standard deviation and med the median value of the differences.

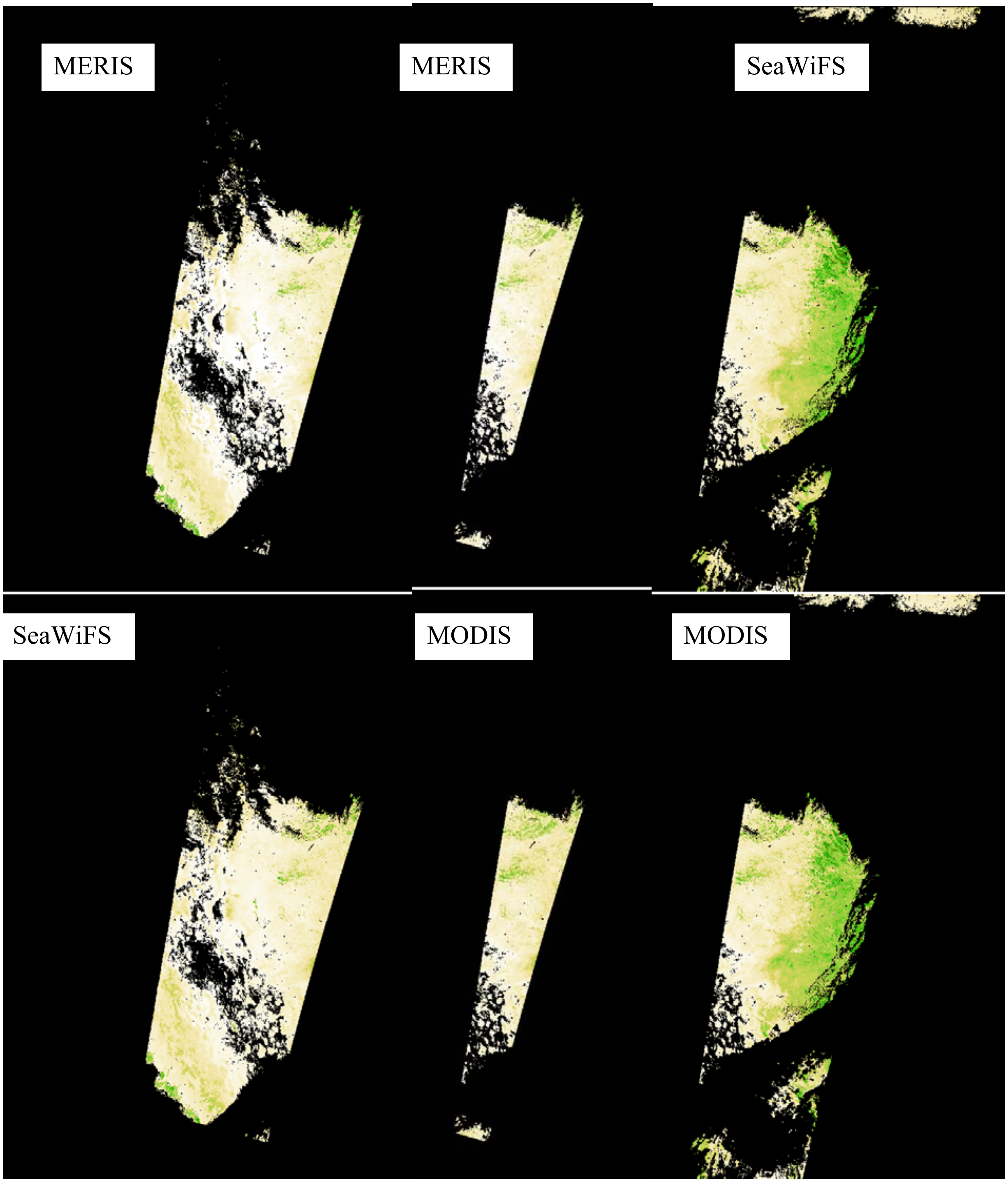

Figure 48: Maps of FAPAR values remapped at 1.2 km for MERIS/SeaWiFS (left panel), MERIS/MODIS (middle panel) and SeaWiFS/MODIS (left panel) over **JORNADA** (2003/04/06). The black pixels correspond to common mask when comparing FAPAR derived from two instruments.

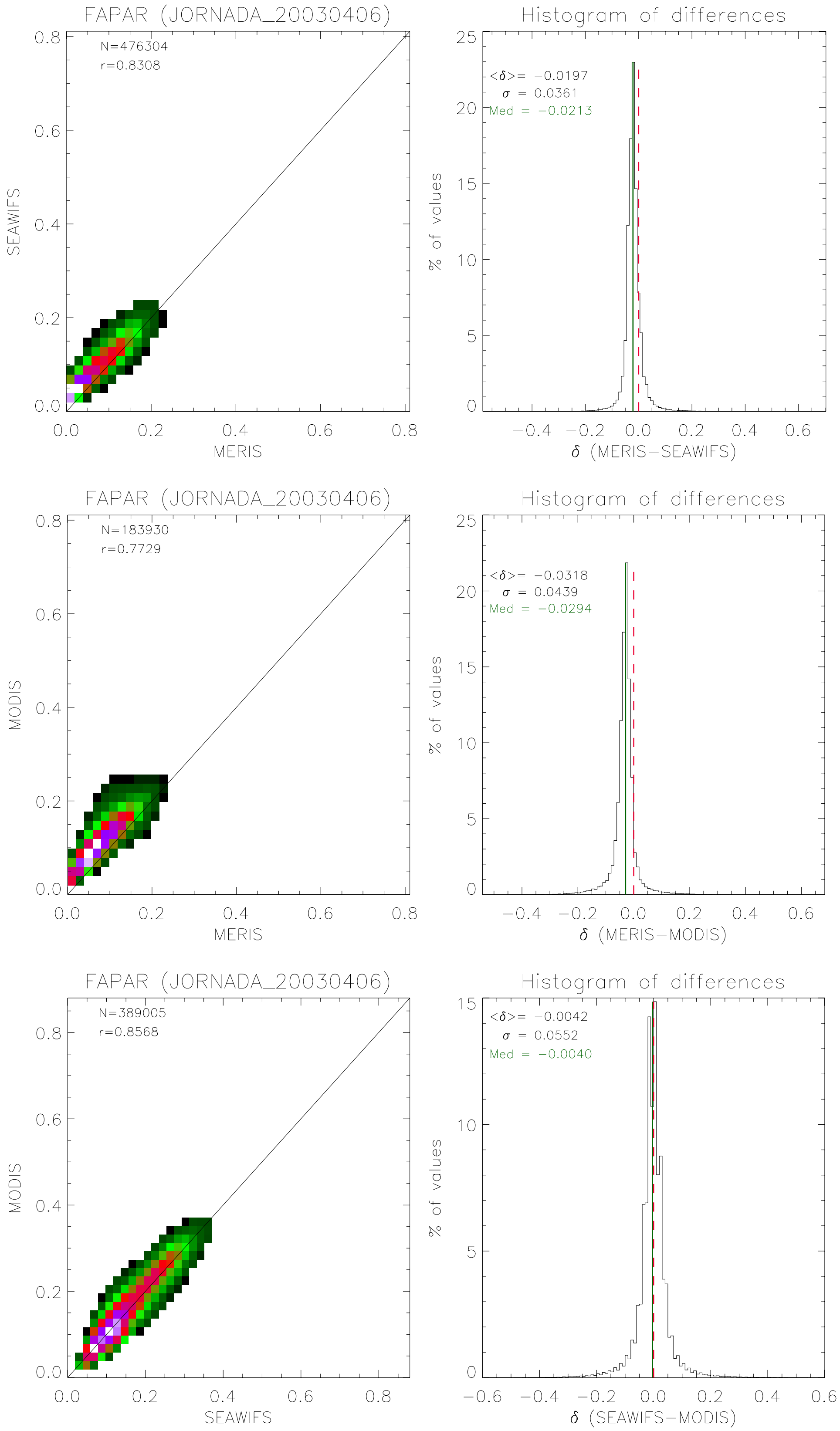

Figure 49: Scatter-plots and histogram of difference between FAPAR values remapped at 1.2 km derived from MERIS/SeaWiFS, MERIS/MODIS and SeaWiFS/MODIS over **JORNADA** (2003/04/06). N indicates the number of pixels, r the correlation, <δ> the mean of differences, σ the standard deviation and med the median value of the differences.

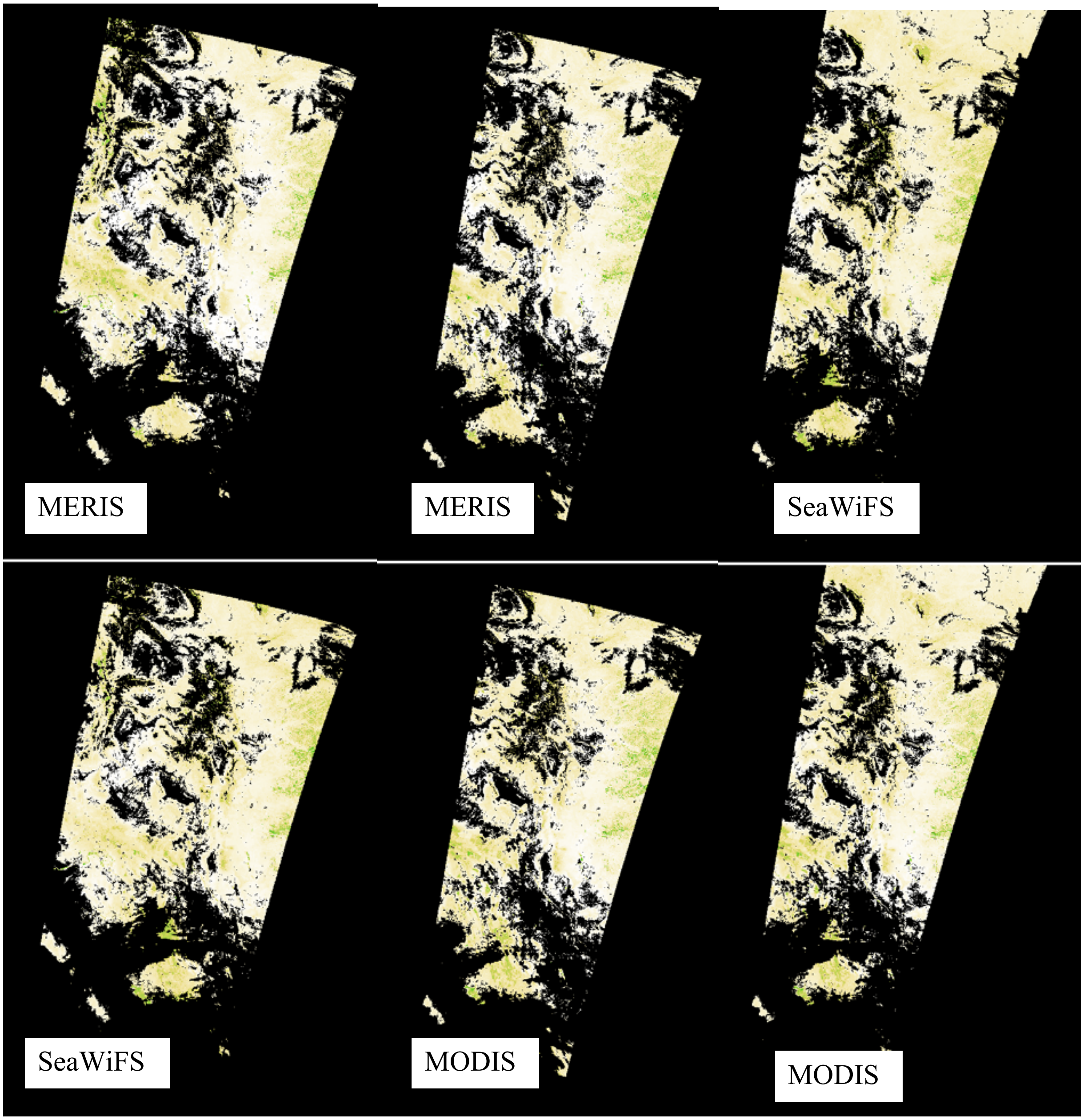

Figure 50: Maps of FAPAR values remapped at 1.2 km for MERIS/SeaWiFS (left panel), MERIS/MODIS (middle panel) and SeaWiFS/MODIS (left panel) over **JORNADA** (2003/04/09). The black pixels correspond to common mask when comparing FAPAR derived from two instruments.

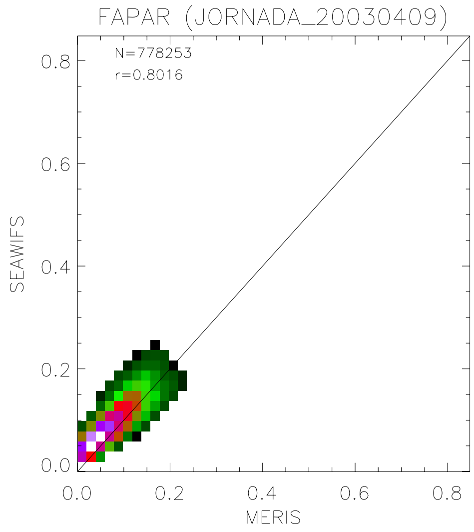
FAPAR (JORNADA_20030409)
N=778253
r=0.8016
SEAWIFS
MERIS
0.0
0.2
0.4
0.6
0.8

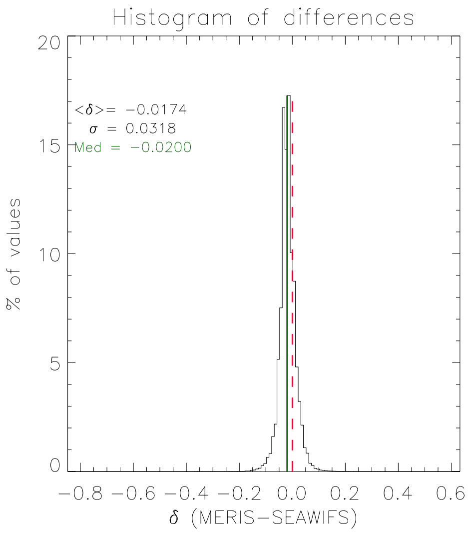
Histogram of differences
<δ>= −0.0174
σ = 0.0318
Med = −0.0200
% of values
δ (MERIS−SEAWIFS)
0
5
10
15
20
−0.8 −0.6 −0.4 −0.2 0.0 0.2 0.4 0.6

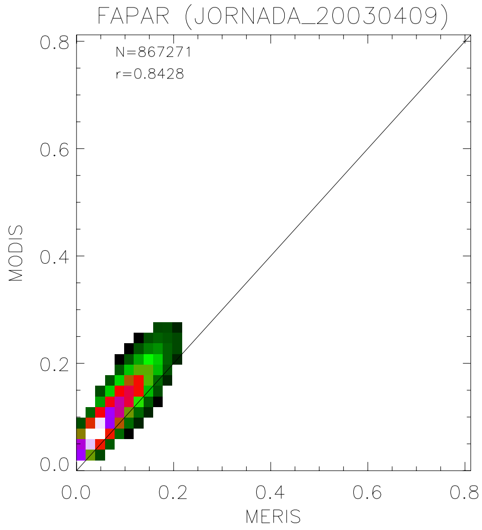
FAPAR (JORNADA_20030409)
N=867271
r=0.8428
MODIS
MERIS
0.0
0.2
0.4
0.6
0.8

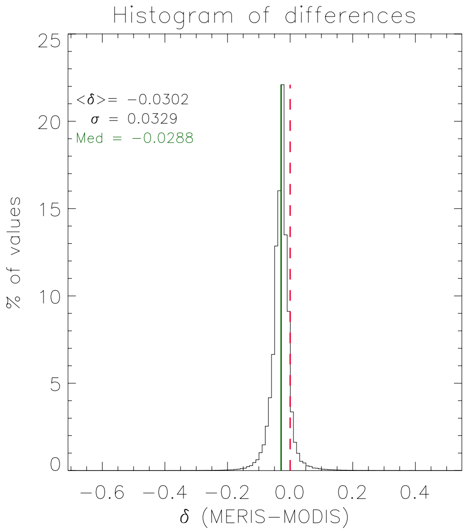
Histogram of differences
<δ>= −0.0302
σ = 0.0329
Med = −0.0288
% of values
δ (MERIS−MODIS)
0
5
10
15
20
25
−0.6 −0.4 −0.2 0.0 0.2 0.4

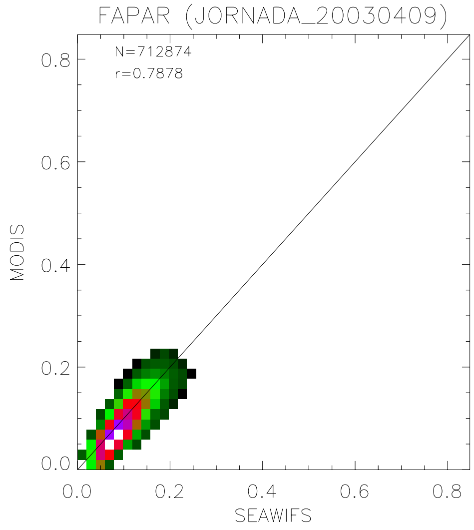
FAPAR (JORNADA_20030409)
N=712874
r=0.7878
MODIS
SEAWIFS
0.0
0.2
0.4
0.6
0.8

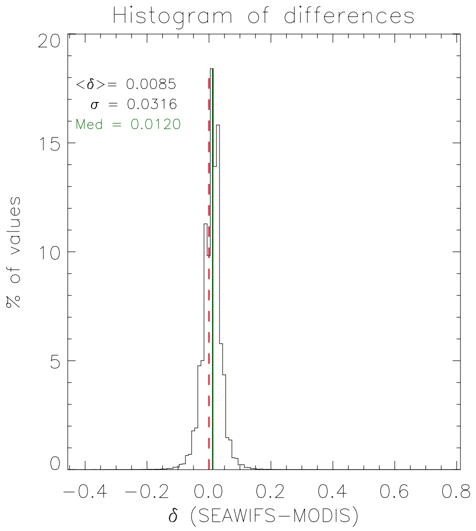
Histogram of differences
<δ>= 0.0085
σ = 0.0316
Med = 0.0120
% of values
δ (SEAWIFS−MODIS)
0
5
10
15
20
−0.4 −0.2 0.0 0.2 0.4 0.6 0.8

Figure 51: Scatter-plots and histogram of difference between FAPAR values remapped at 1.2 km derived from MERIS/SeaWiFS, MERIS/MODIS and SeaWiFS/MODIS over **JORNADA** (2003/04/09). N indicates the number of pixels, r the correlation, <δ> the mean of differences, σ the standard deviation and med the median value of the differences.

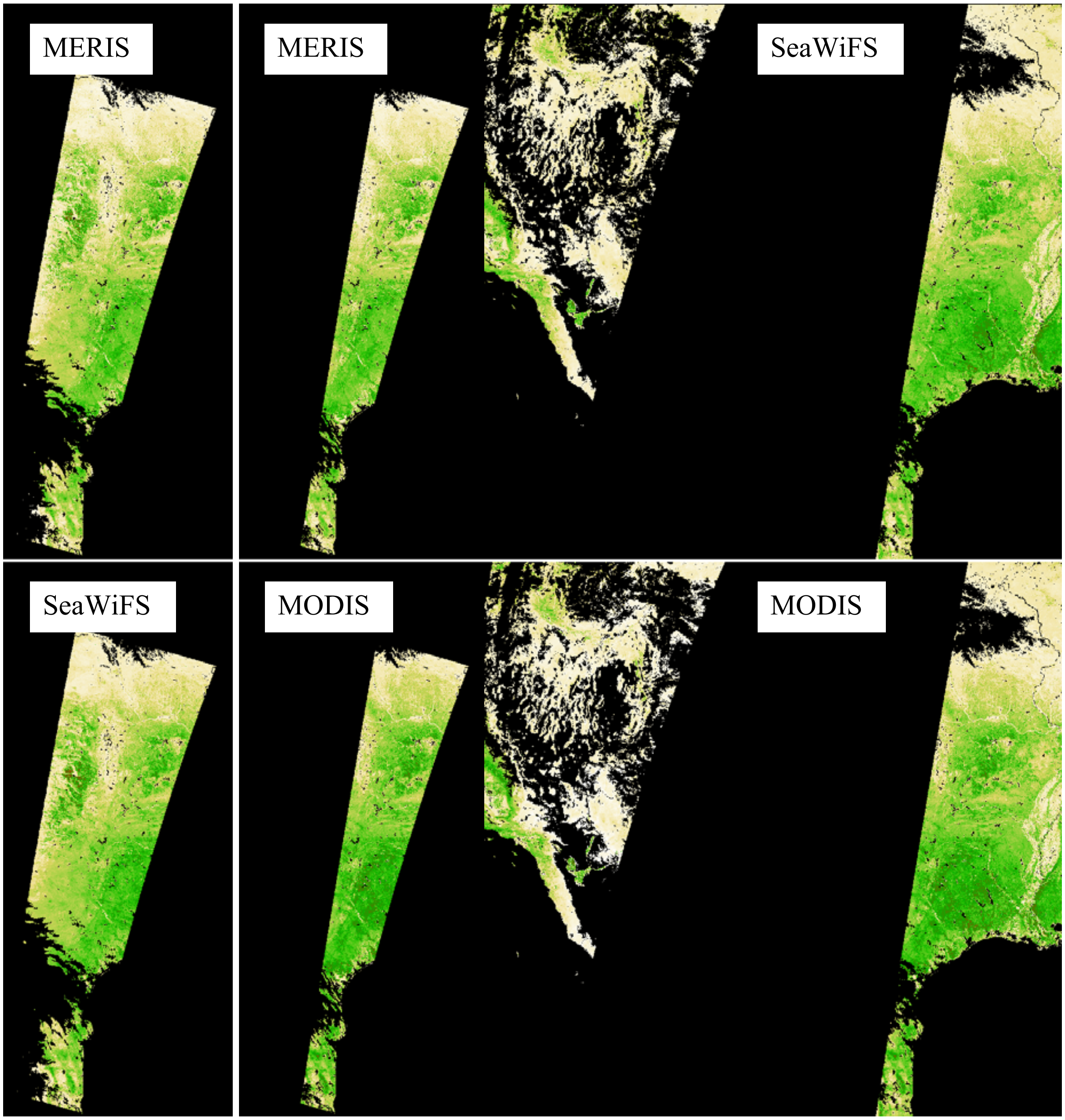

Figure 52: Maps of FAPAR values remapped at 1.2 km for MERIS/SeaWiFS (left panel), MERIS/MODIS (middle panel) and SeaWiFS/MODIS (left panel) over **JORNADA** (2003/04/10). The black pixels correspond to common mask when comparing FAPAR derived from two instruments.

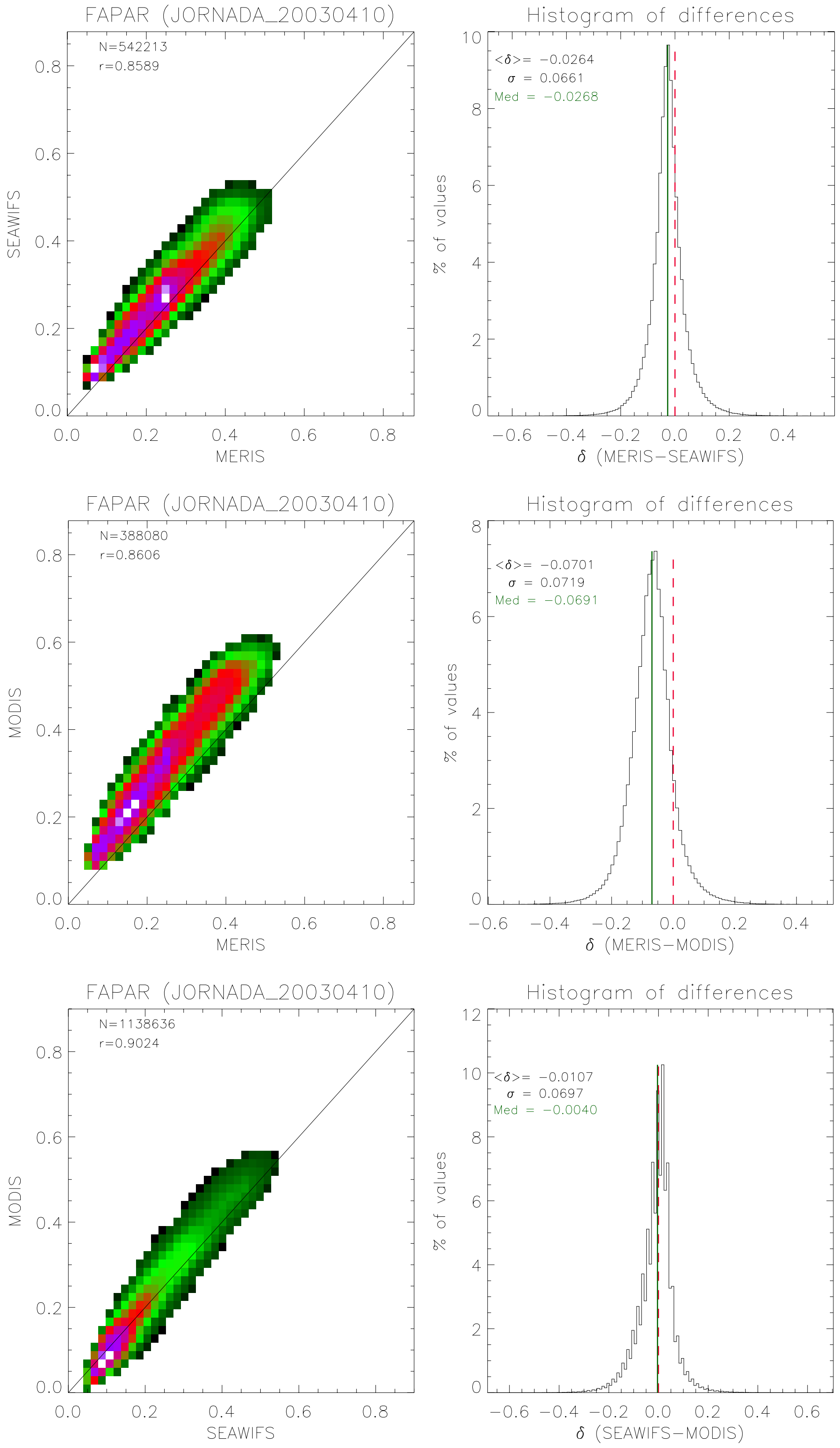

Figure 53: Scatter-plots and histogram of difference between FAPAR values remapped at 1.2 km derived from MERIS/SeaWiFS, MERIS/MODIS and SeaWiFS/MODIS over **JORNADA** (2003/04/10). N indicates the number of pixels, r the correlation, <δ> the mean of differences, σ the standard deviation and med the median value of the differences.

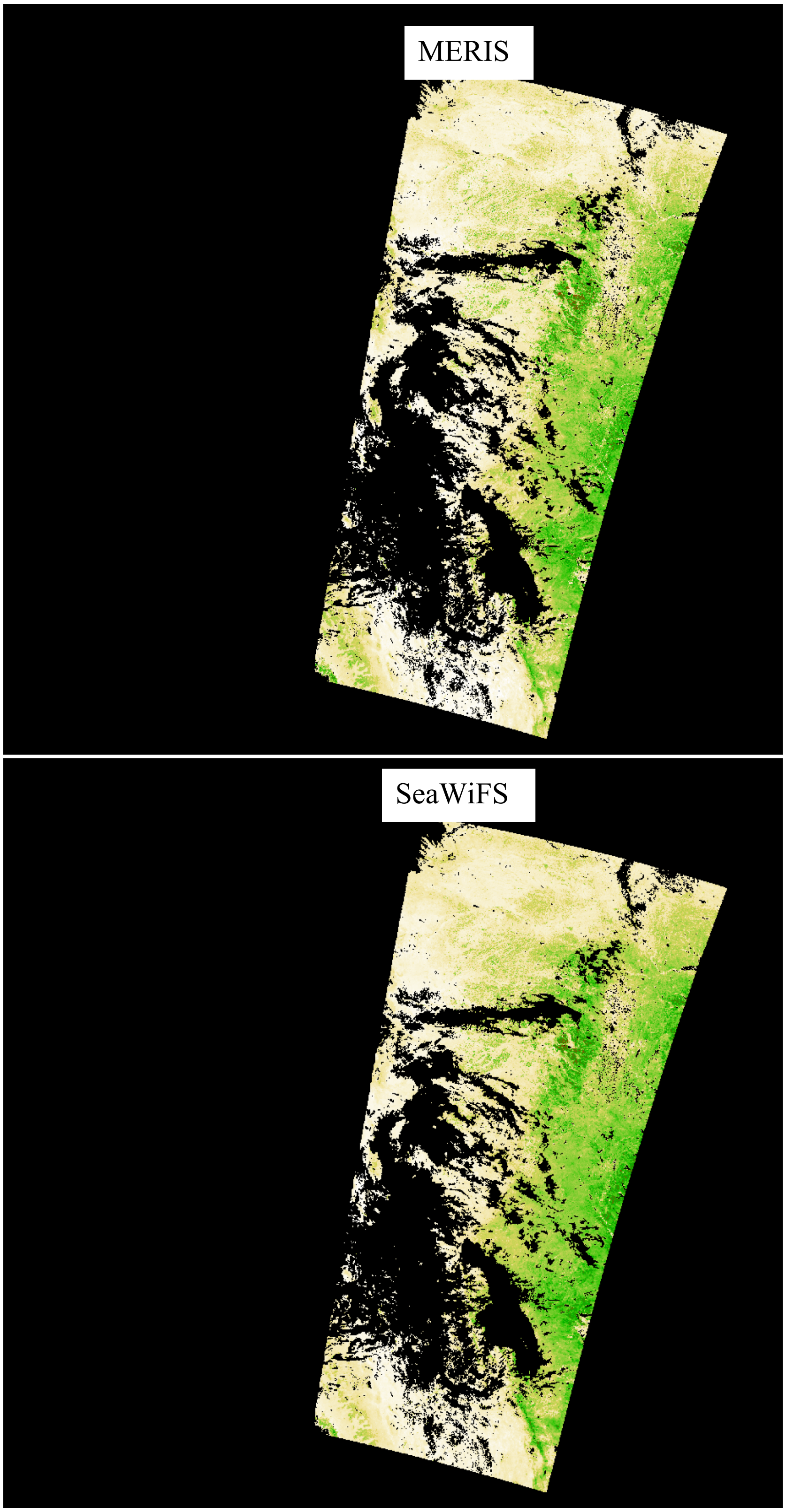

Figure 54: Maps of FAPAR values remapped at 1.2 km for MERIS/SeaWiFS over **JORNADA** (2003/04/13). The black pixels correspond to common mask when comparing FAPAR derived from two instruments.

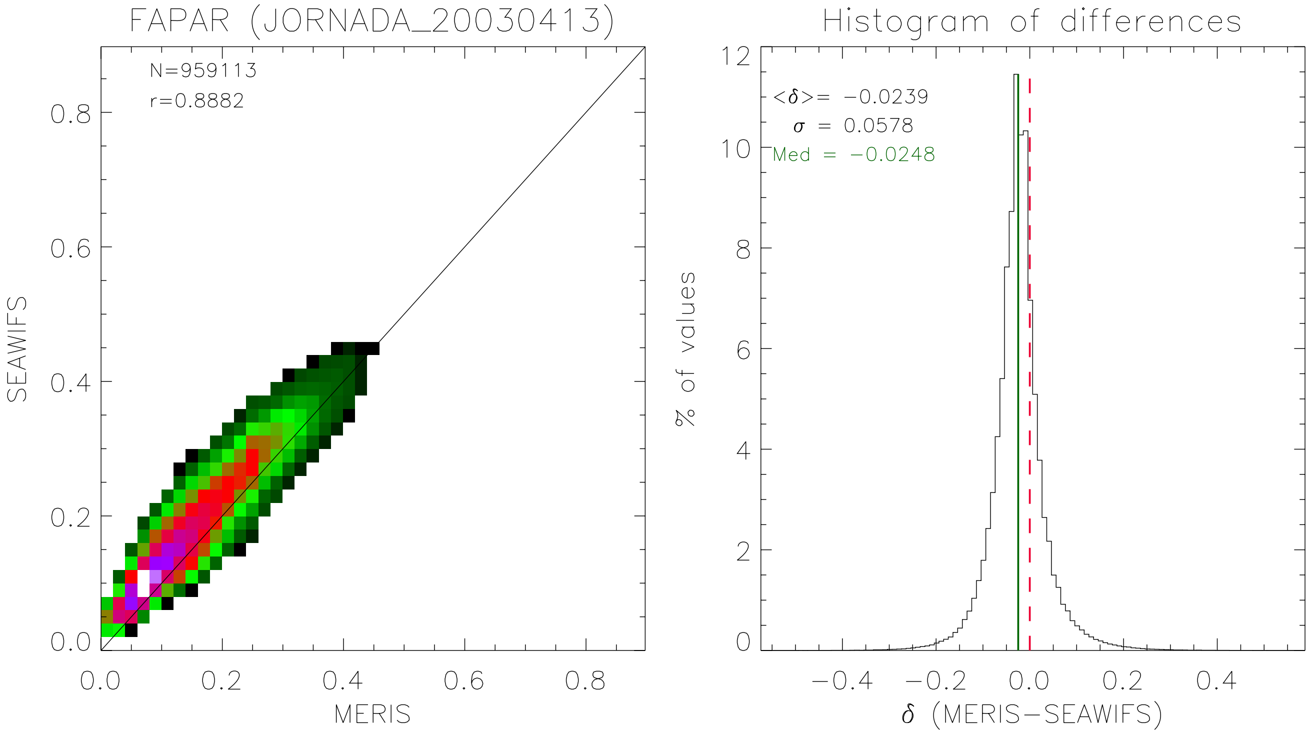

Figure 55: Scatter-plots and histogram of difference between FAPAR values remapped at 1.2 km derived from MERIS and SeaWiFS. N indicates the number of pixels, r the correlation, <δ> the mean of differences, σ the standard deviation and med the median value of the differences over **JORNADA** (2003/04/13).

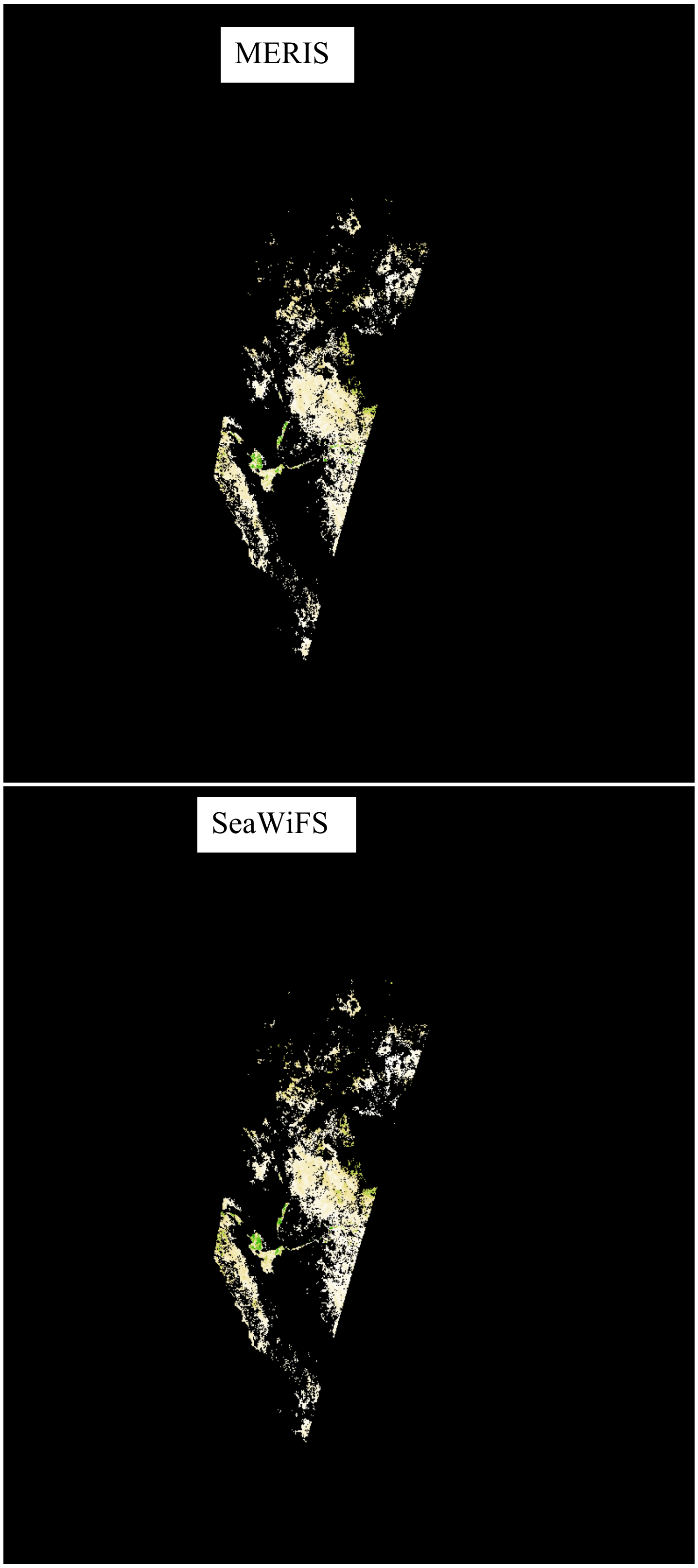

Figure 56: Maps of FAPAR values remapped at 1.2 km for MERIS/SeaWiFS over **MARICOPA** (2002/12/27). The black pixels correspond to common mask when comparing FAPAR derived from two instruments.

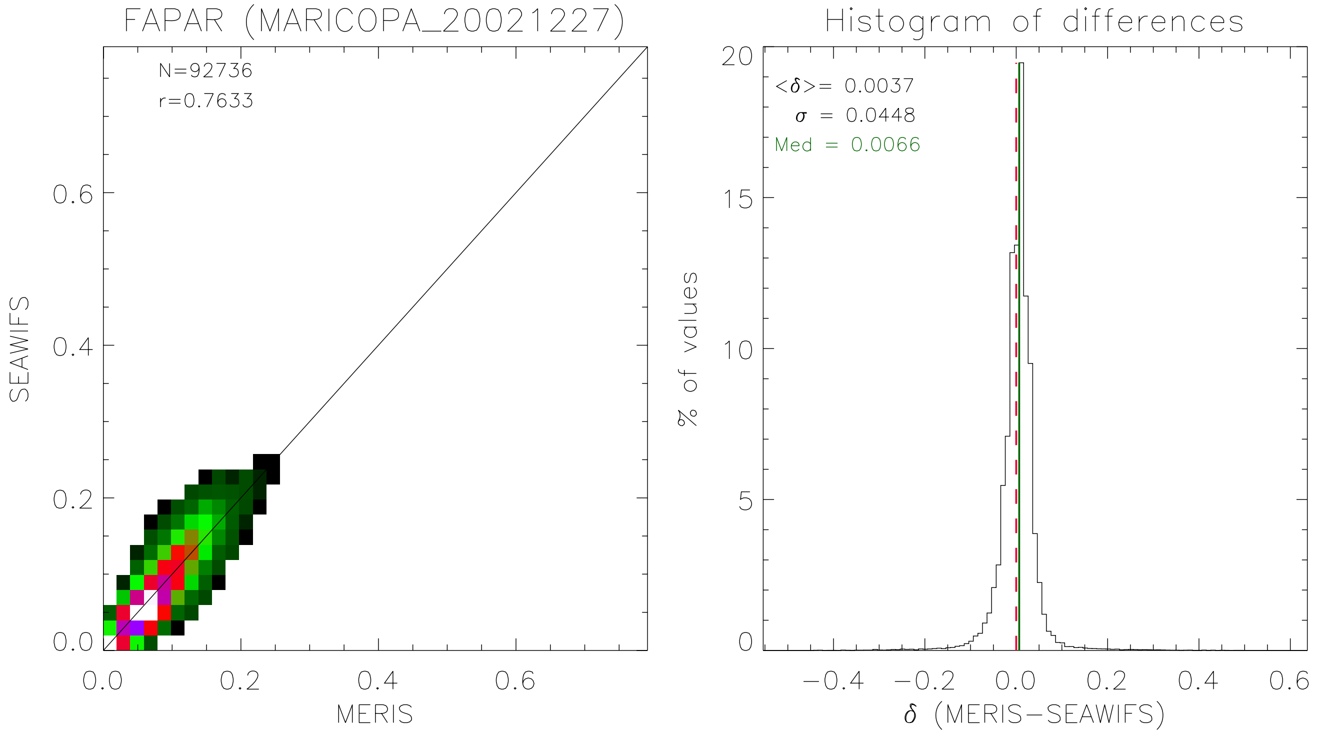

Figure 57: Scatter-plots and histogram of difference between FAPAR values remapped at 1.2 km derived from MERIS/SeaWiFS. N indicates the number of pixels, r the correlation, <δ> the mean of differences, σ the standard deviation and med the median value of the differences **MARICOPA** (2002/12/27).

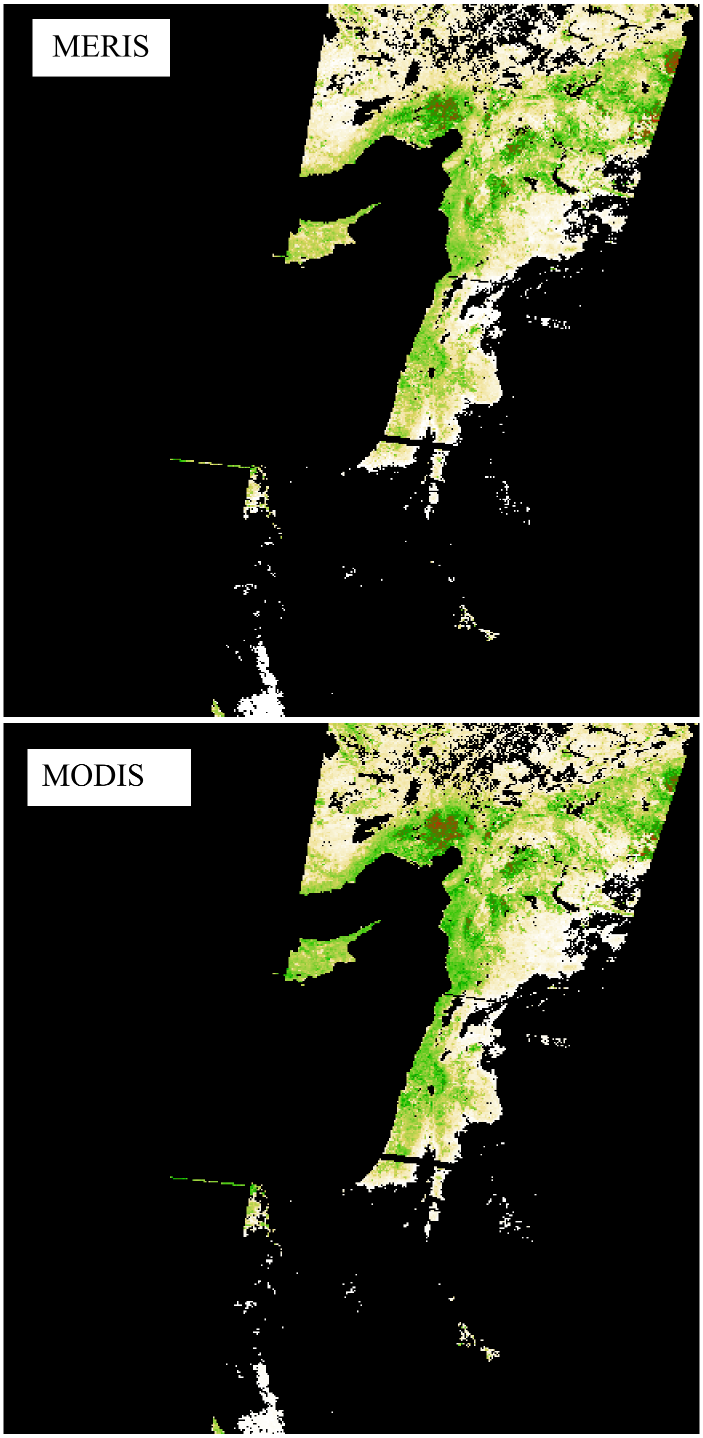

Figure 58: Maps of FAPAR values remapped at 1.2 km for MERIS and MODIS over **YATIR** (2003/04/30). The black pixels correspond to common mask when comparing FAPAR derived from two instruments.

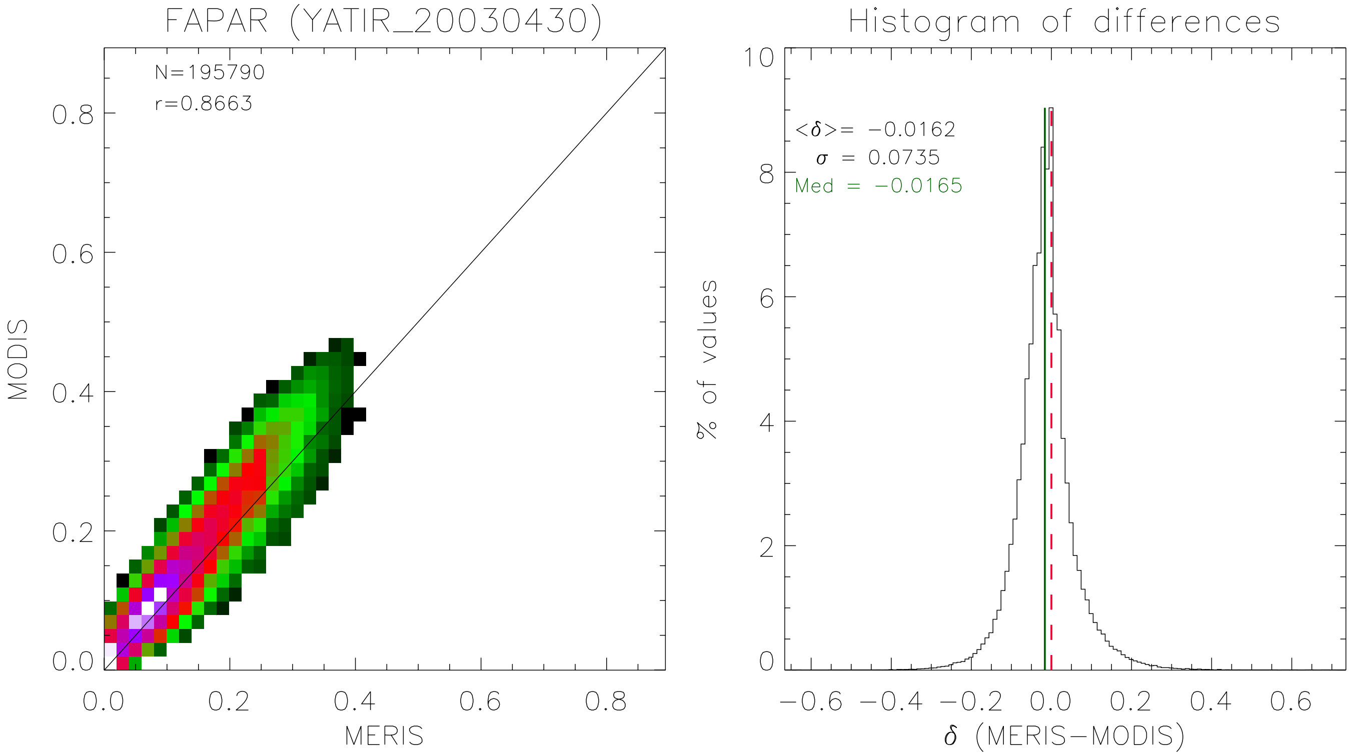

Figure 59: Scatter-plots and histogram of difference between FAPAR values remapped at 1.2 km derived from MERIS/MODIS. N indicates the number of pixels, r the correlation, <δ> the mean of differences, σ the standard deviation and med the median value of the differences over **YATIR** (2003/04/30).

16. ANNEX C: Results of comparison between monthly FAPAR derived from MERIS, SeaWiFS and MODIS over Europe

January 2003

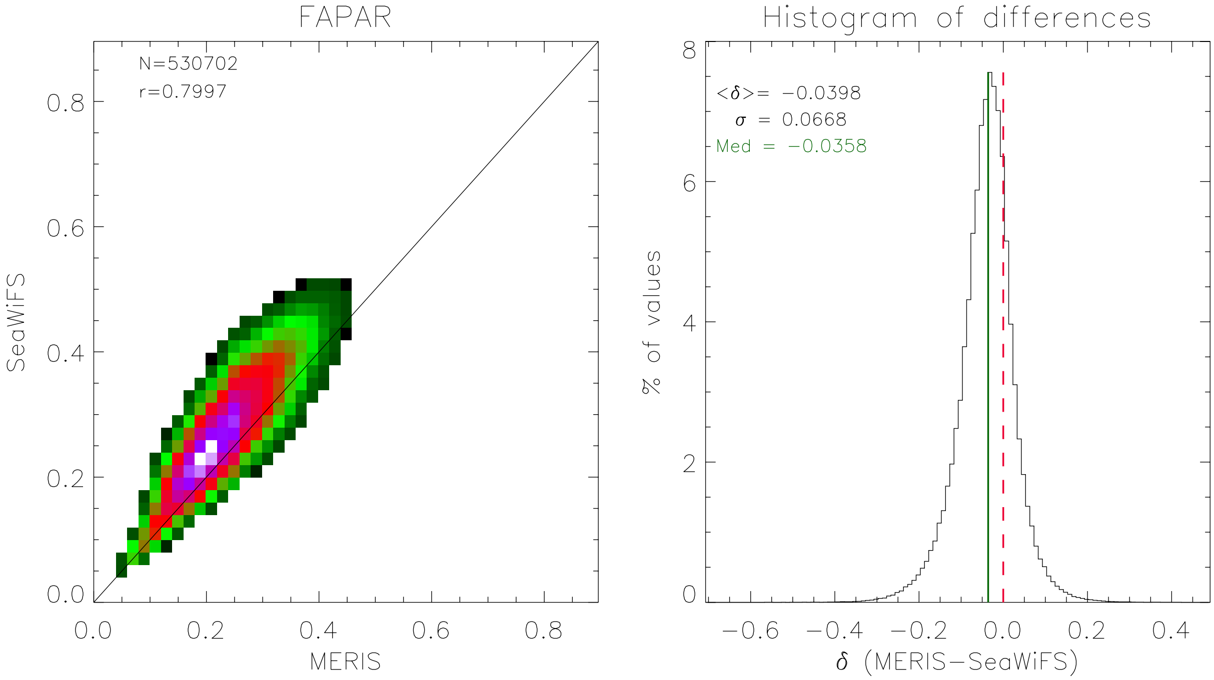

Figure 60: Scatter-plots and histogram of difference between FAPAR values remapped or aggregated at 2.0 km from SeaWiFS (y-axis) and MERIS (x-axis) over Europe in **January** 2003. N indicates the number of pixels, r the correlation, <δ> the mean of differences, σ the standard deviation and med the median value of the differences.

February 2003

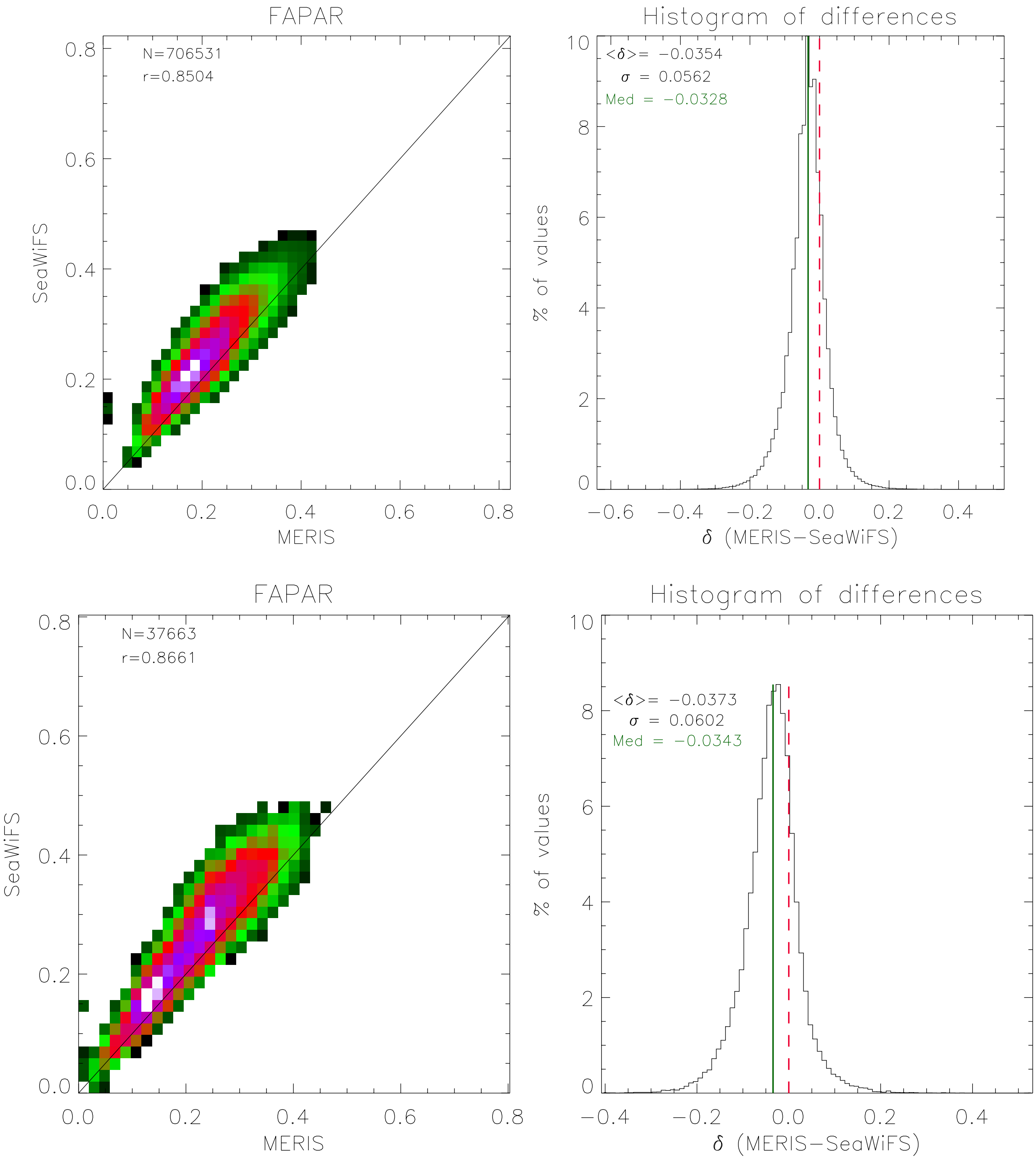

Figure 61: Scatter-plots and histogram of difference between FAPAR values remapped or aggregated at 2.0 km from SeaWiFS (y-axis) and MERIS (x-axis) over Europe in **February** 2003. N indicates the number of pixels, r the correlation, <δ> the mean of differences, σ the standard deviation and med the median value of the differences.

March 2003

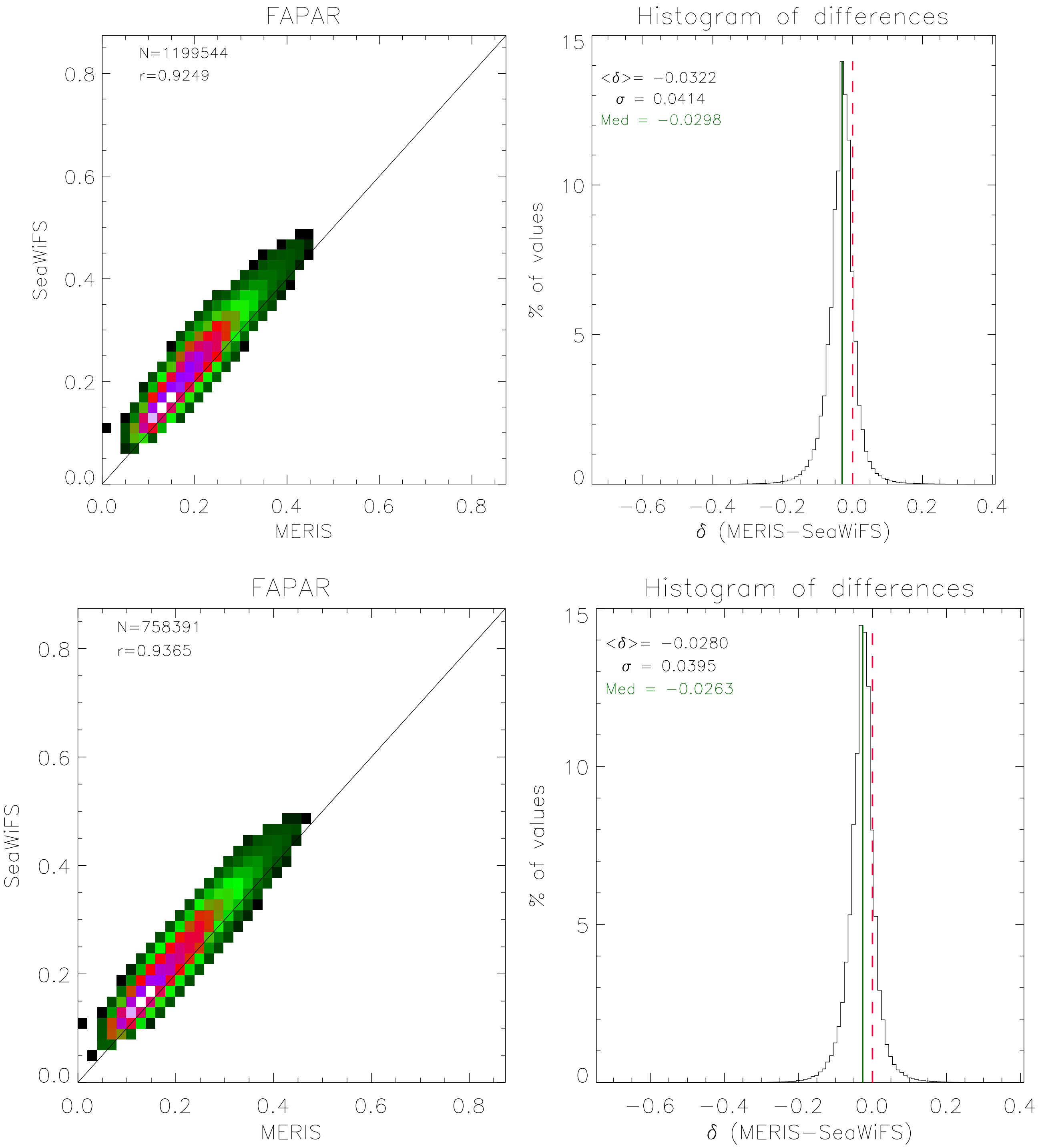

Figure 62: Scatter-plots and histogram of difference between FAPAR values remapped or aggregated at 2.0 km from SeaWiFS (y-axis) and MERIS (x-axis) over Europe in **March** 2003. N indicates the number of pixels, r the correlation, <δ> the mean of differences, σ the standard deviation and med the median value of the differences.

April 2003

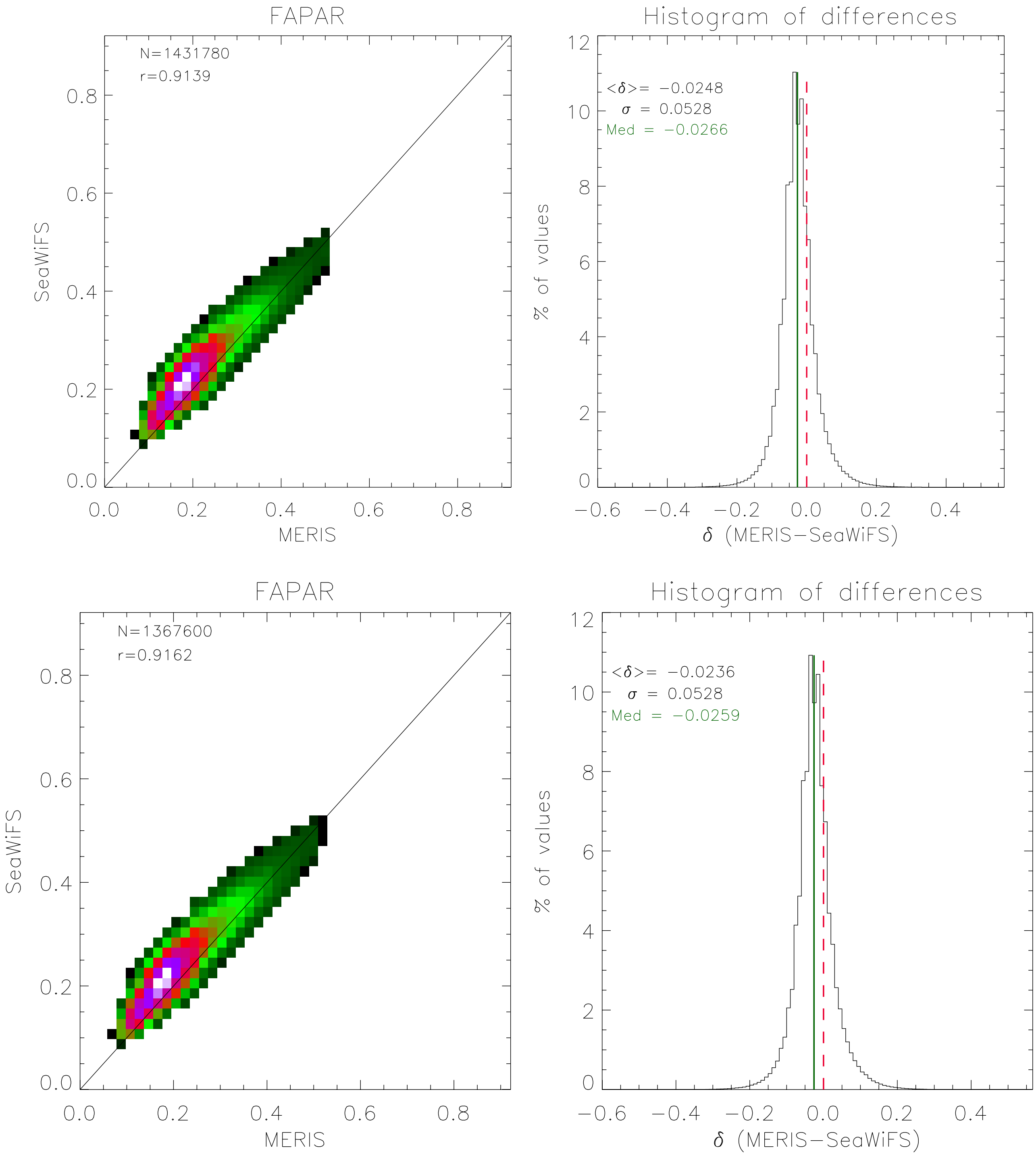

Figure 63: Scatter-plots and histogram of difference between FAPAR values remapped or aggregated at 2.0 km from SeaWiFS (y-axis) and MERIS (x-axis) over Europe in **April** 2003. N indicates the number of pixels, r the correlation, <δ> the mean of differences, σ the standard deviation and med the median value of the differences.

May 2003

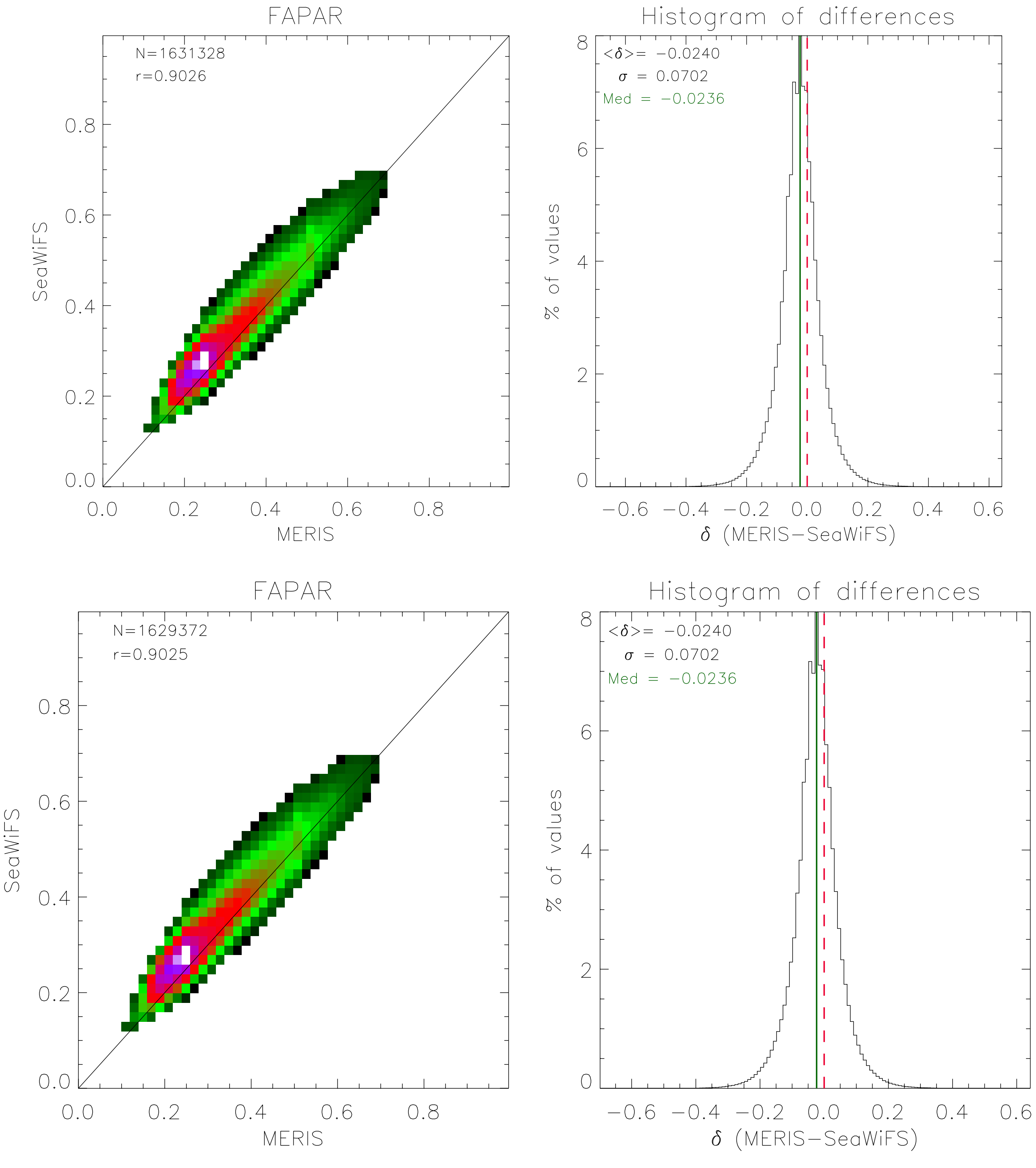

Figure 64: Scatter-plots and histogram of difference between FAPAR values remapped or aggregated at 2.0 km from SeaWiFS (y-axis) and MERIS (x-axis) over Europe in **May** 2003. N indicates the number of pixels, r the correlation, <δ> the mean of differences, σ the standard deviation and med the median value of the differences.

June 2003

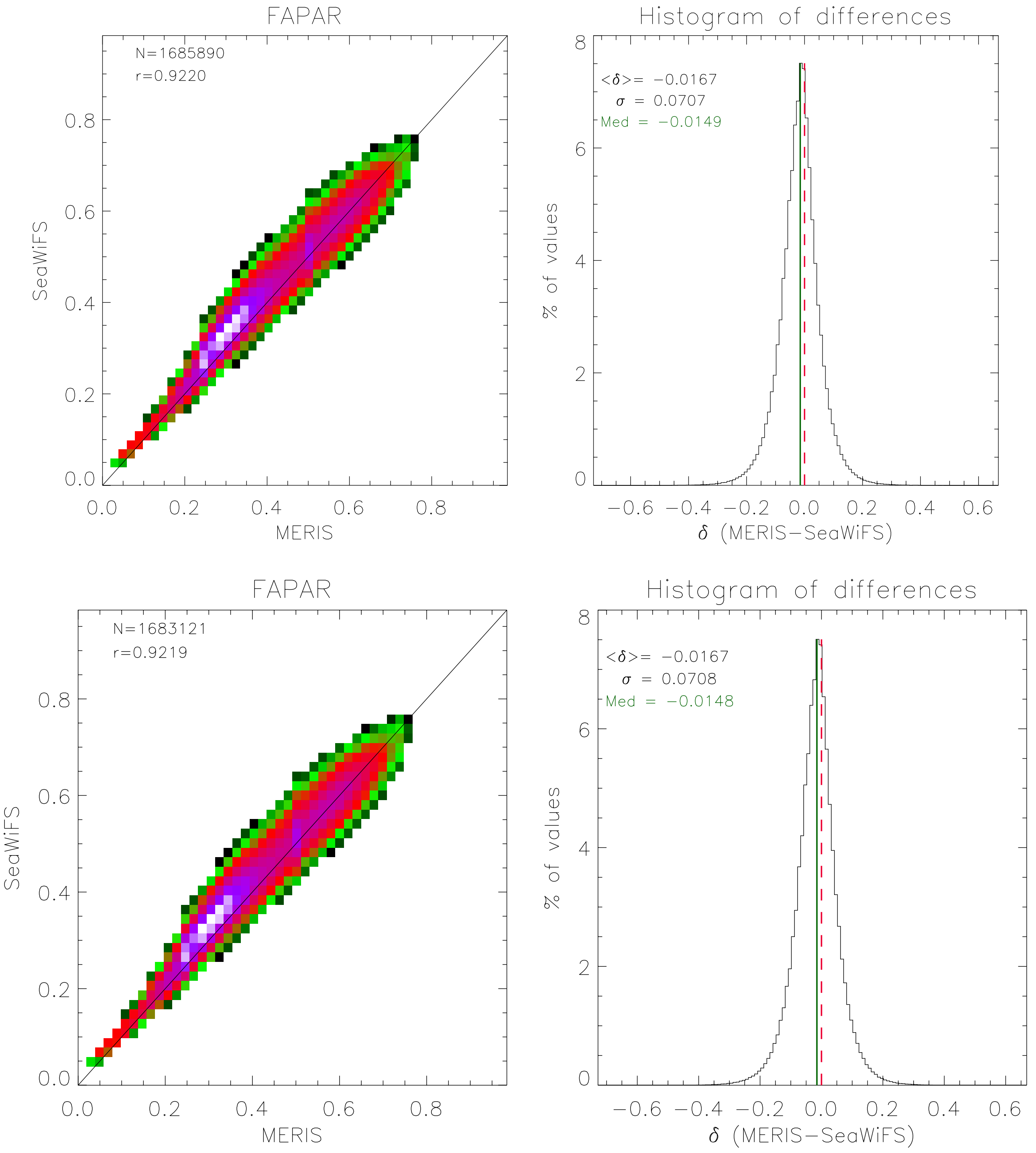

Figure 65: Scatter-plots and histogram of difference between FAPAR values remapped or aggregated at 2.0 km from SeaWiFS (y-axis) and MERIS (x-axis) over Europe in **June** 2003. N indicates the number of pixels, r the correlation, <δ> the mean of differences, σ the standard deviation and med the median value of the differences.

July 2003

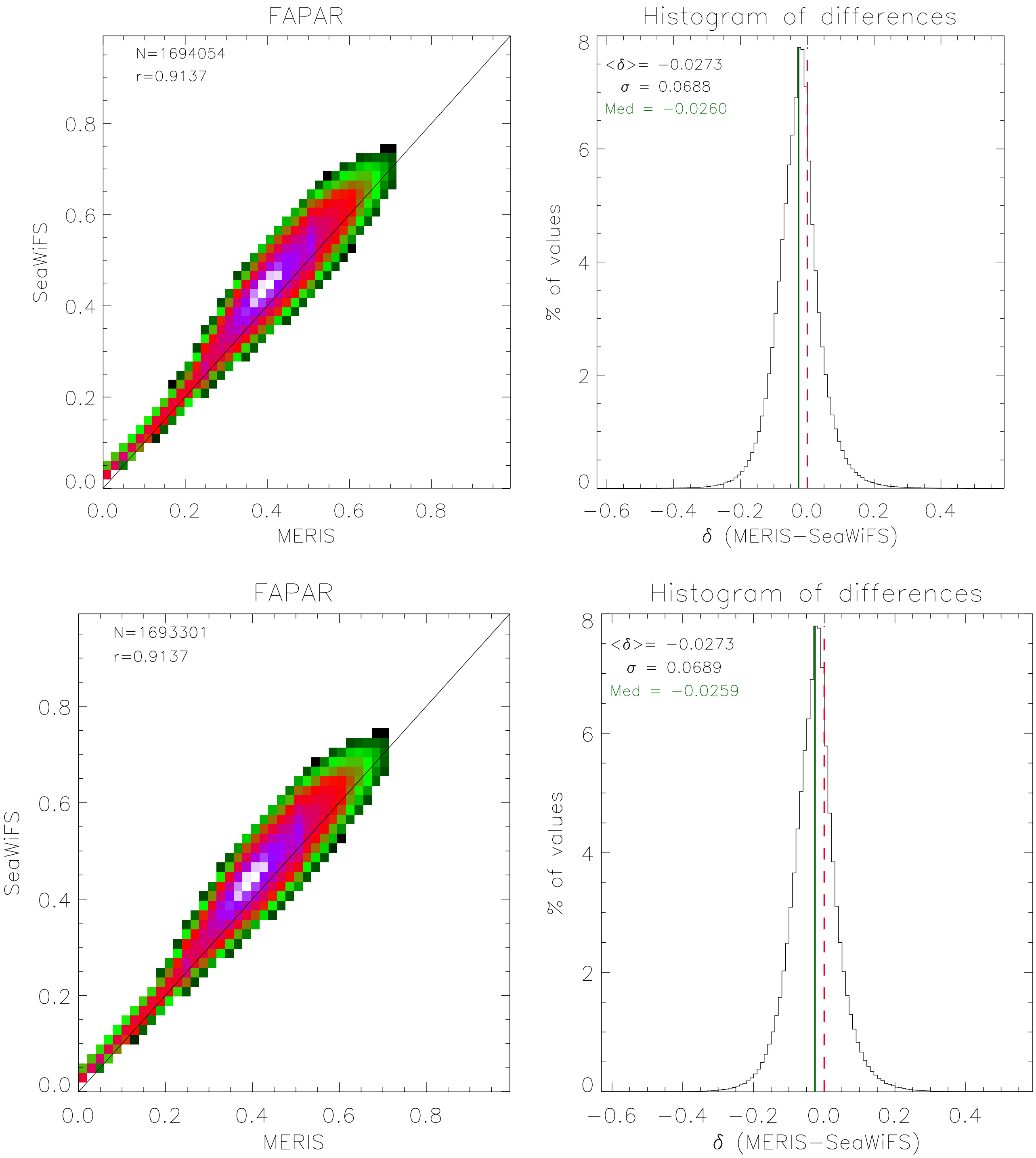

Figure 66: Scatter-plots and histogram of difference between FAPAR values remapped or aggregated at 2.0 km from SeaWiFS (y-axis) and MERIS (x-axis) over Europe in **July** 2003. N indicates the number of pixels, r the correlation, <δ> the mean of differences, σ the standard deviation and med the median value of the differences.

August 2003

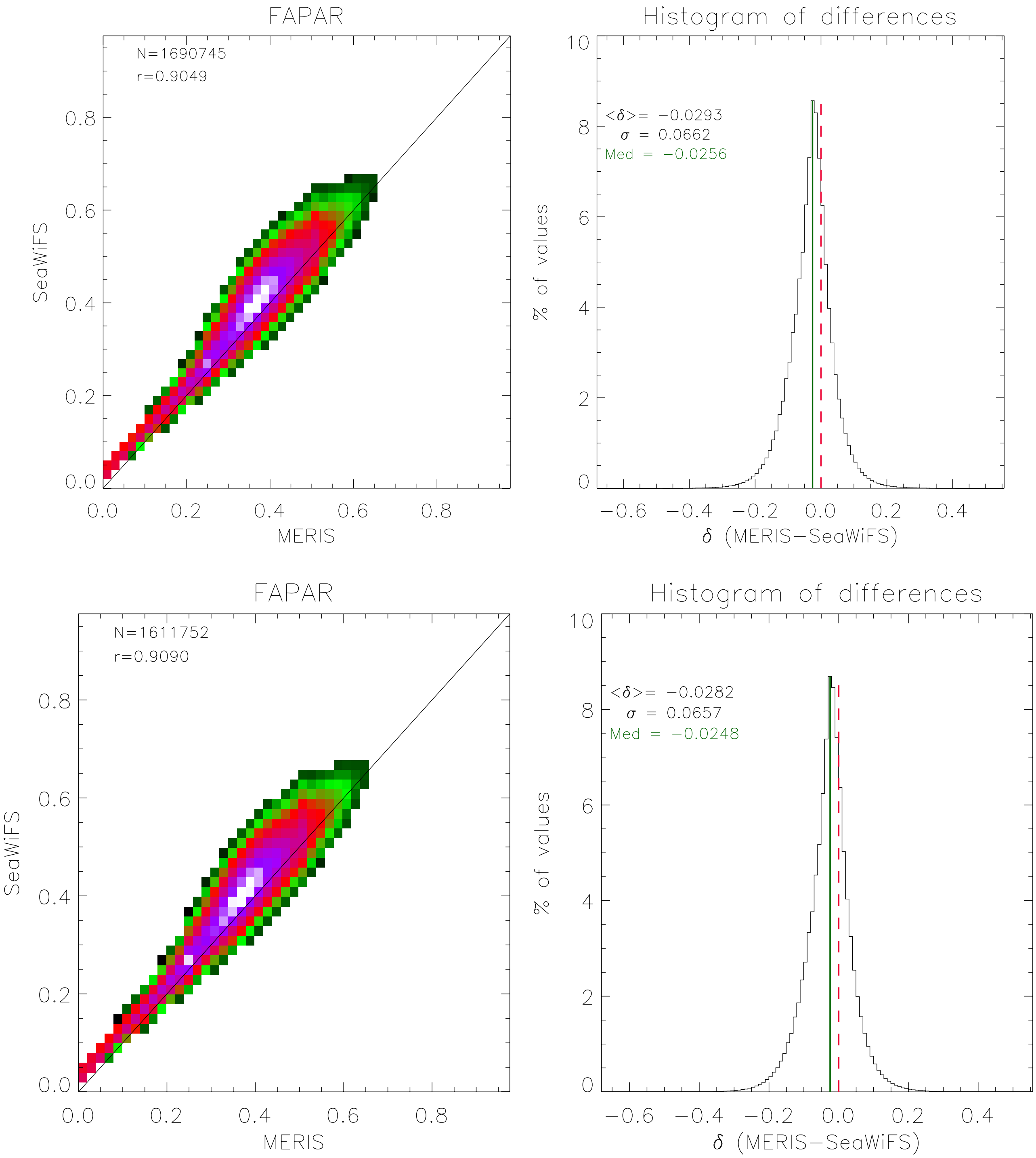

Figure 67: Scatter-plots and histogram of difference between FAPAR values remapped or aggregated at 2.0 km from SeaWiFS (y-axis) and MERIS (x-axis) over Europe in **August** 2003. N indicates the number of pixels, r the correlation, <δ> the mean of differences, σ the standard deviation and med the median value of the differences.

September 2003

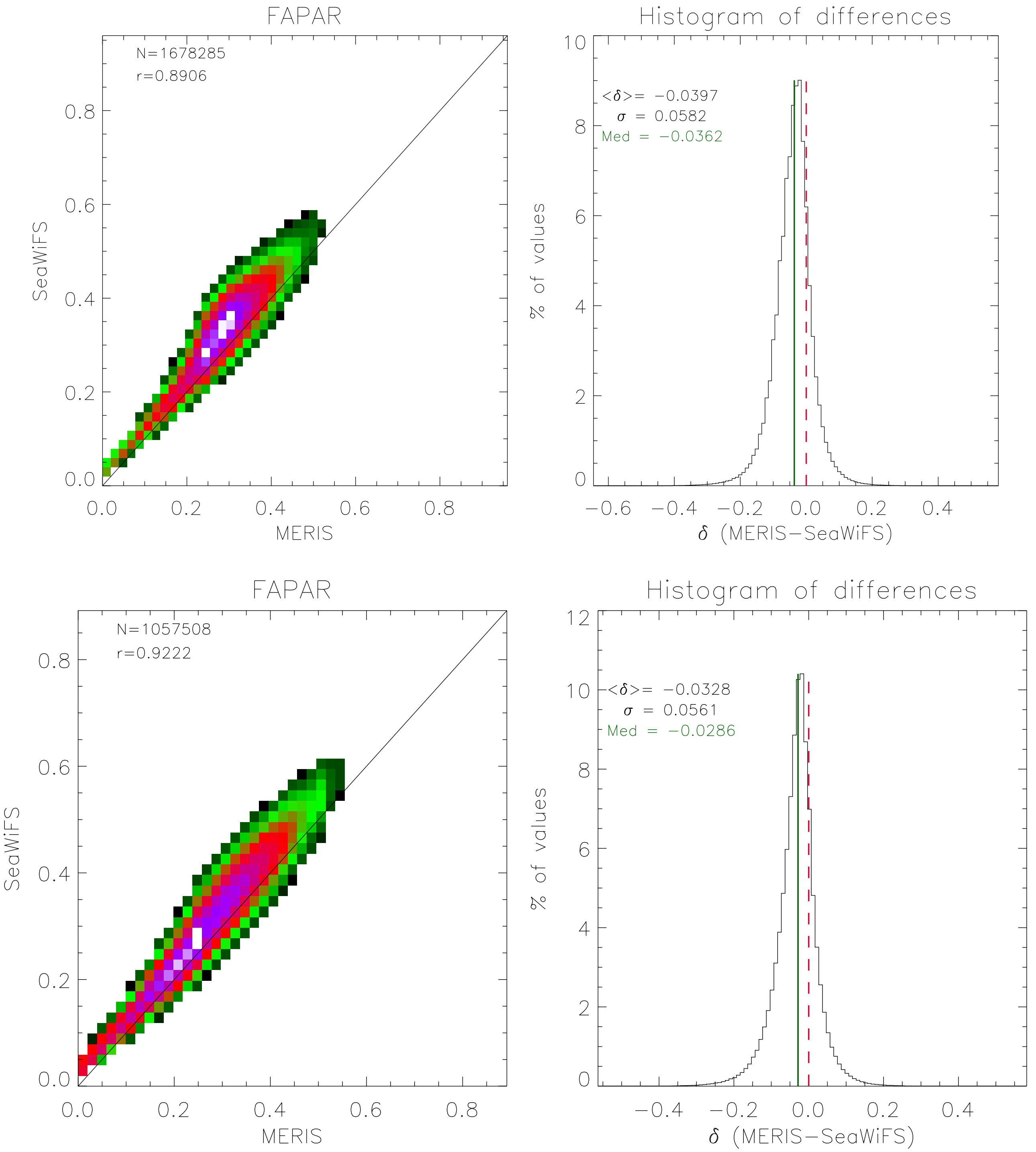

Figure 68: Scatter-plots and histogram of difference between FAPAR values remapped or aggregated at 2.0 km from SeaWiFS (y-axis) and MERIS (x-axis) over Europe in **September** 2003. N indicates the number of pixels, r the correlation, <δ> the mean of differences, σ the standard deviation and med the median value of the differences.

October 2003

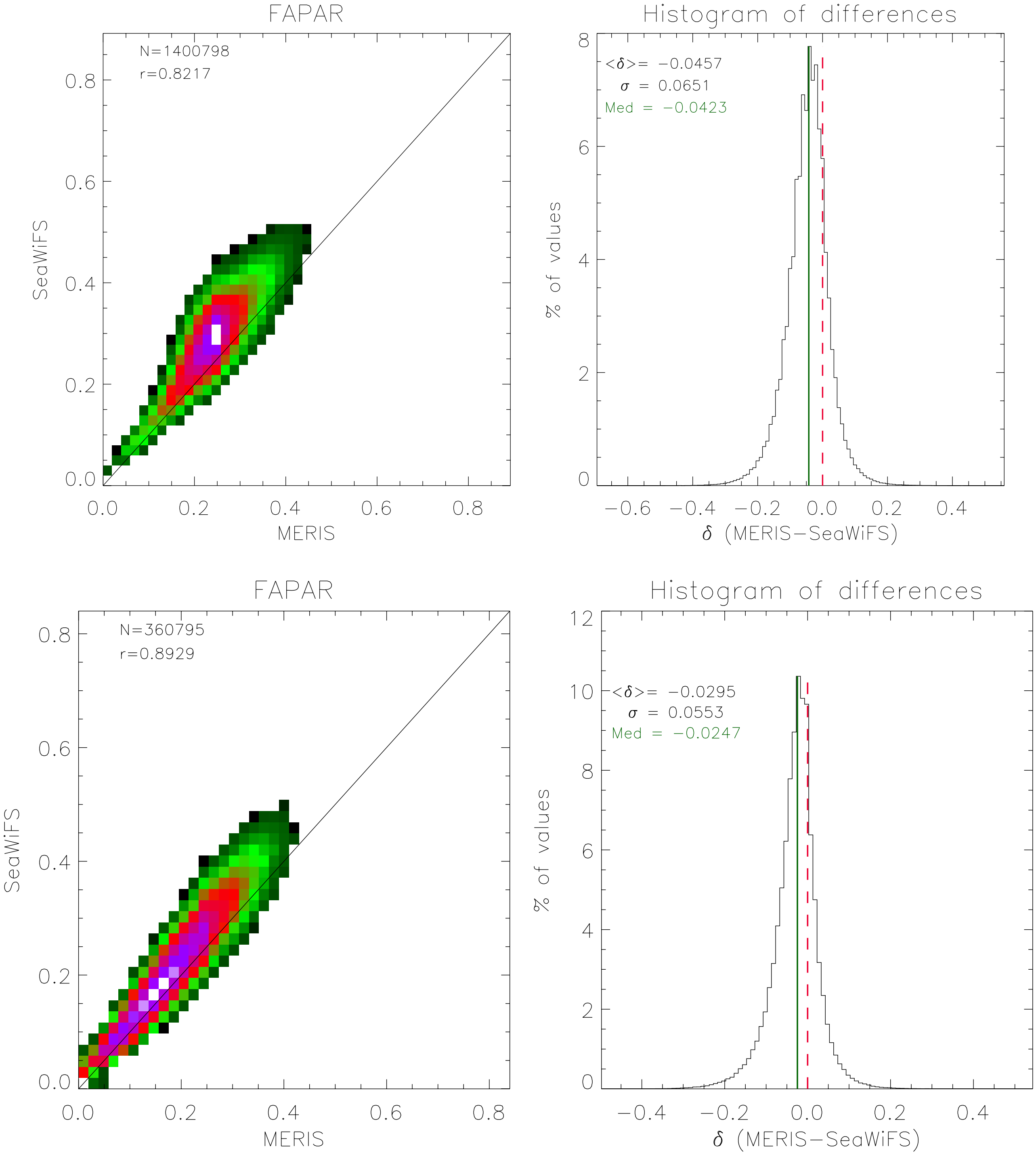

Figure 69: Scatter-plots and histogram of difference between FAPAR values remapped or aggregated at 2.0 km from SeaWiFS (y-axis) and MERIS (x-axis) over Europe in **October** 2003. N indicates the number of pixels, r the correlation, <δ> the mean of differences, σ the standard deviation and med the median value of the differences.

November 2003

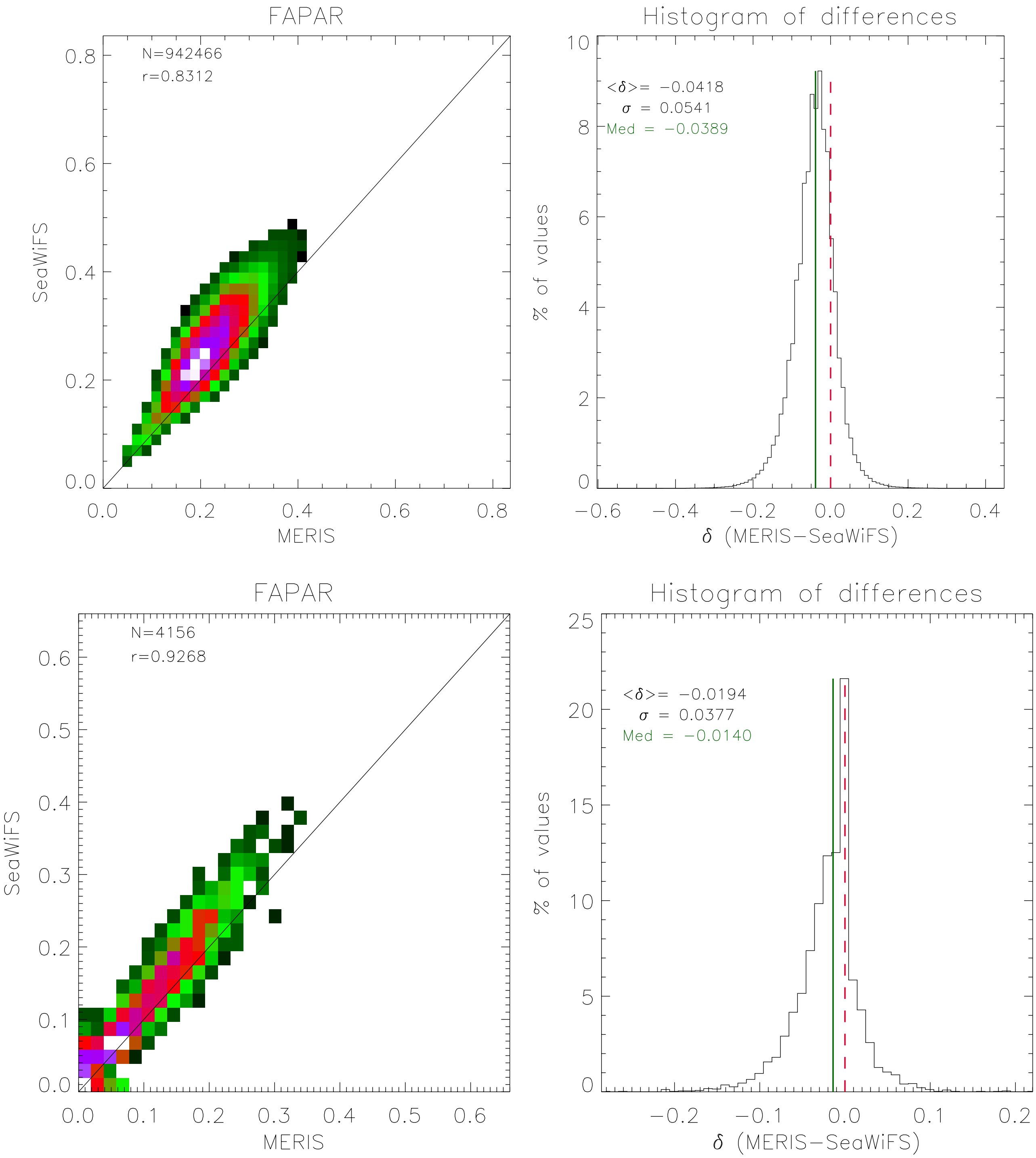

Figure 70: Scatter-plots and histogram of difference between FAPAR values remapped or aggregated at 2.0 km from SeaWiFS (y-axis) and MERIS (x-axis) over Europe in **November** 2003. N indicates the number of pixels, r the correlation, <δ> the mean of differences, σ the standard deviation and med the median value of the differences.

December 2003

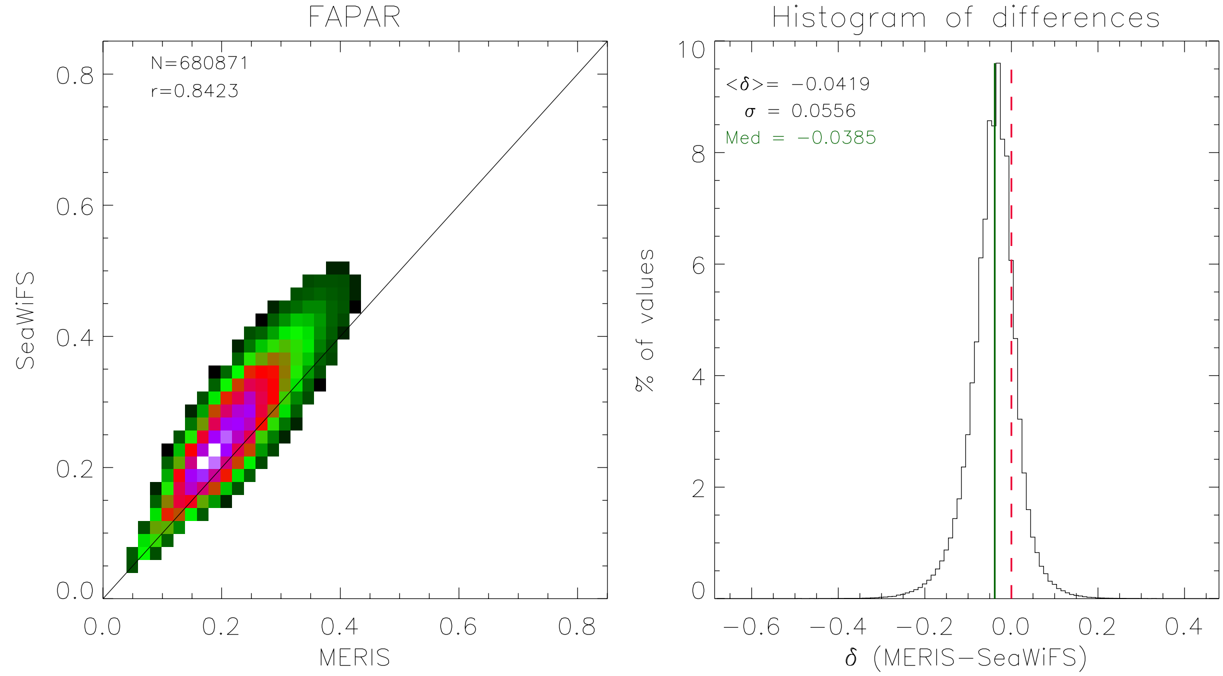

Figure 71: Scatter-plots and histogram of difference between FAPAR values remapped or aggregated at 2.0 km from SeaWiFS (y-axis) and MERIS (x-axis) over Europe in **December** 2003. N indicates the number of pixels, r the correlation, <δ> the mean of differences, σ the standard deviation and med the median value of the differences.

17. ANNEX D: Results of comparison between monthly FAPAR derived from MERIS/SeaWiFS over CarboEurope-IP sites.

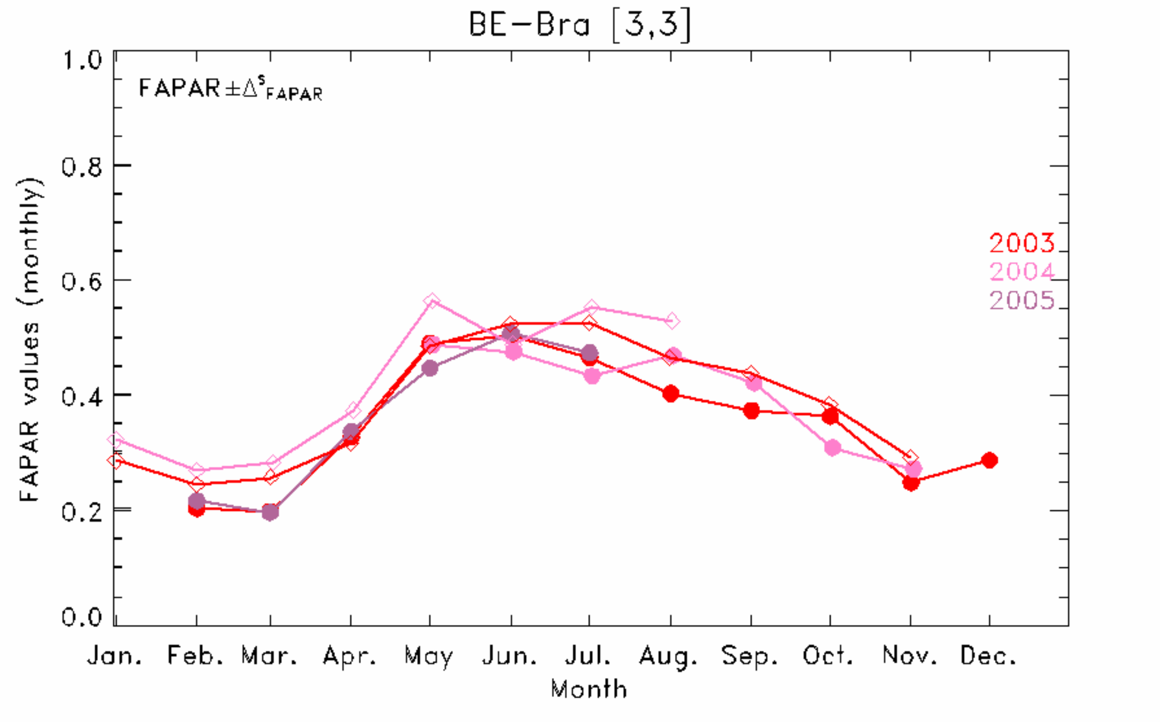

Figure 72: Time-series of monthly FAPAR are plotted over Braschaat (BE) derived from MERIS (SeaWiFS) from 2003 to 2005 (Aug.2004).

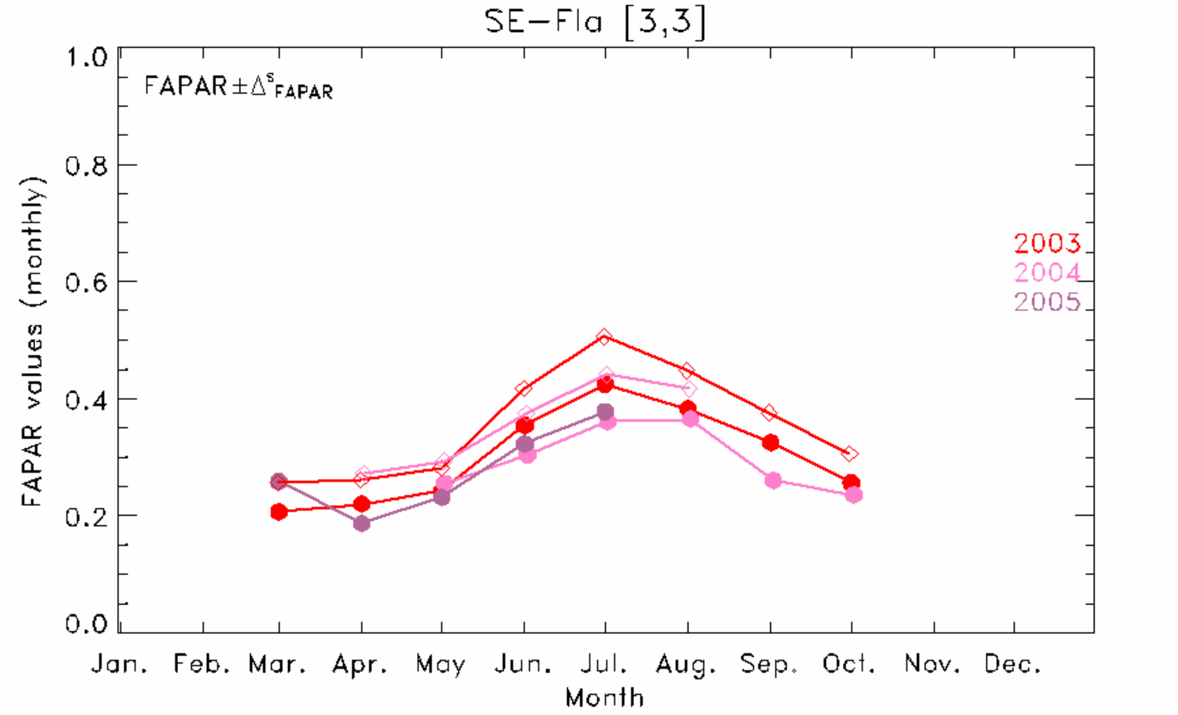

Figure 73**:** Time-series of monthly FAPAR are plotted over Flakaliden (SE) derived from MERIS (SeaWiFS) from 2003 to 2005 (Aug. 2004).

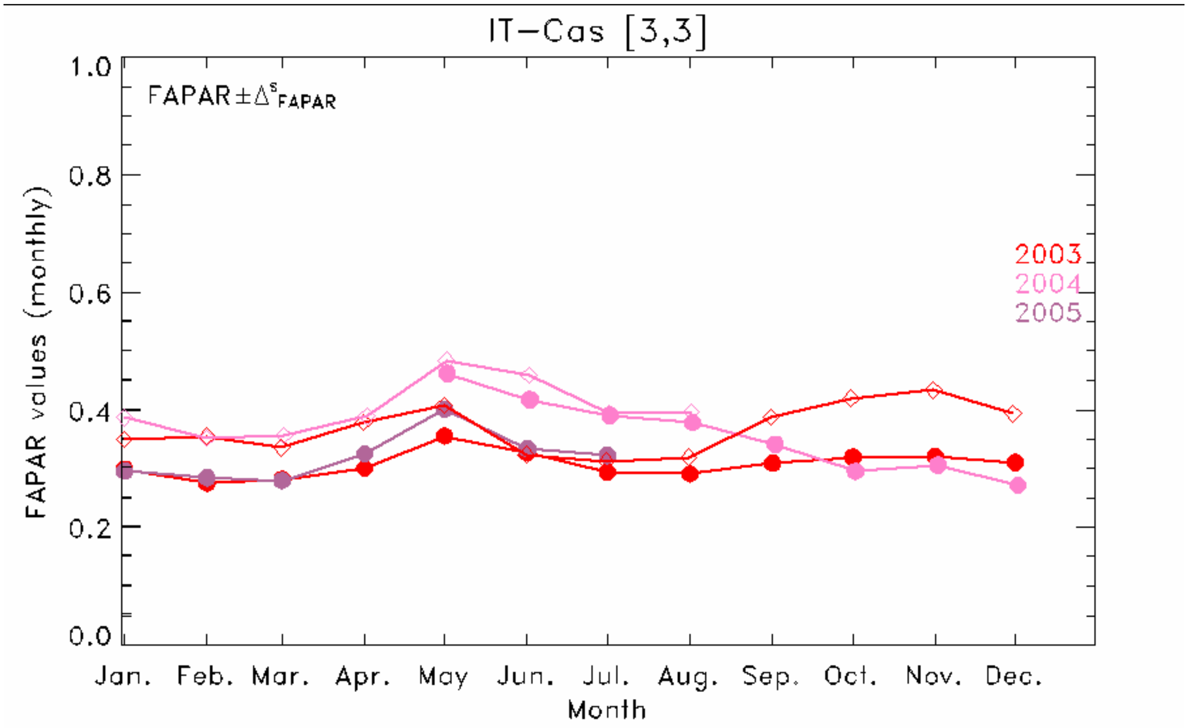

Figure 74**:** Time-series of monthly FAPAR are plotted over Castelporziano (IT) derived from MERIS (SeaWiFS) from 2003 to 2005 (Aug. 2004).

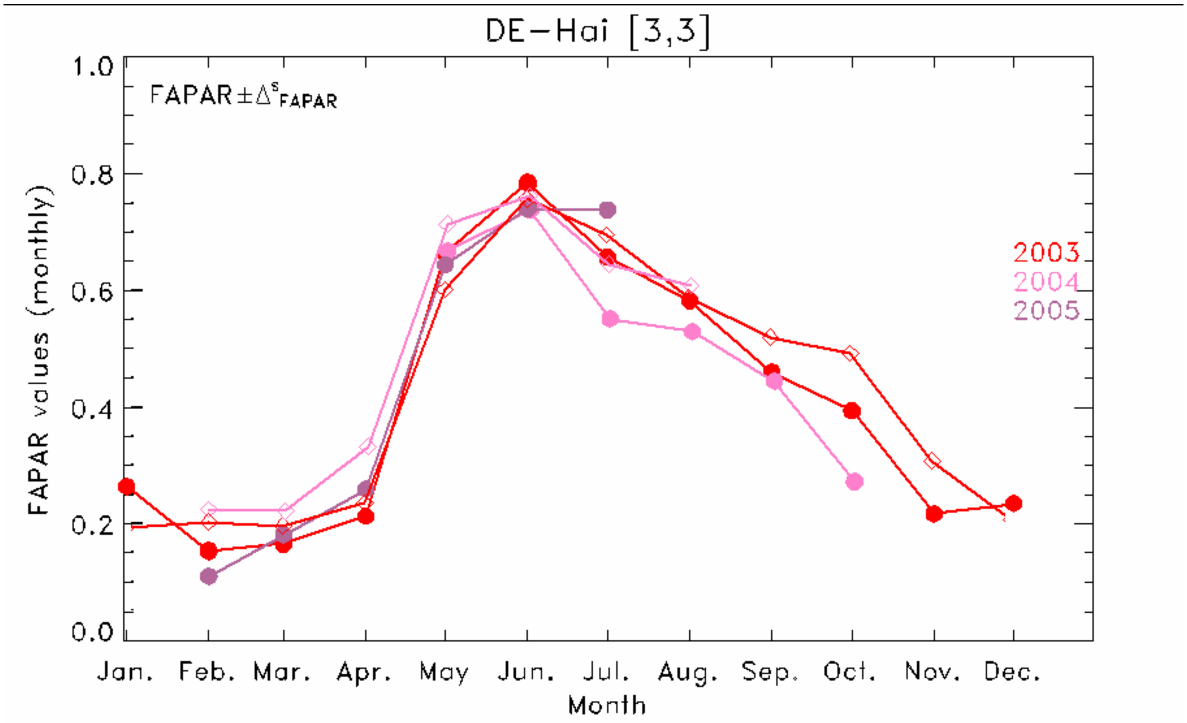

Figure 75: Time-series of monthly FAPAR are plotted over Hainich (DE) derived from MERIS (SeaWiFS) from 2003 to 2005 (Aug. 2004).

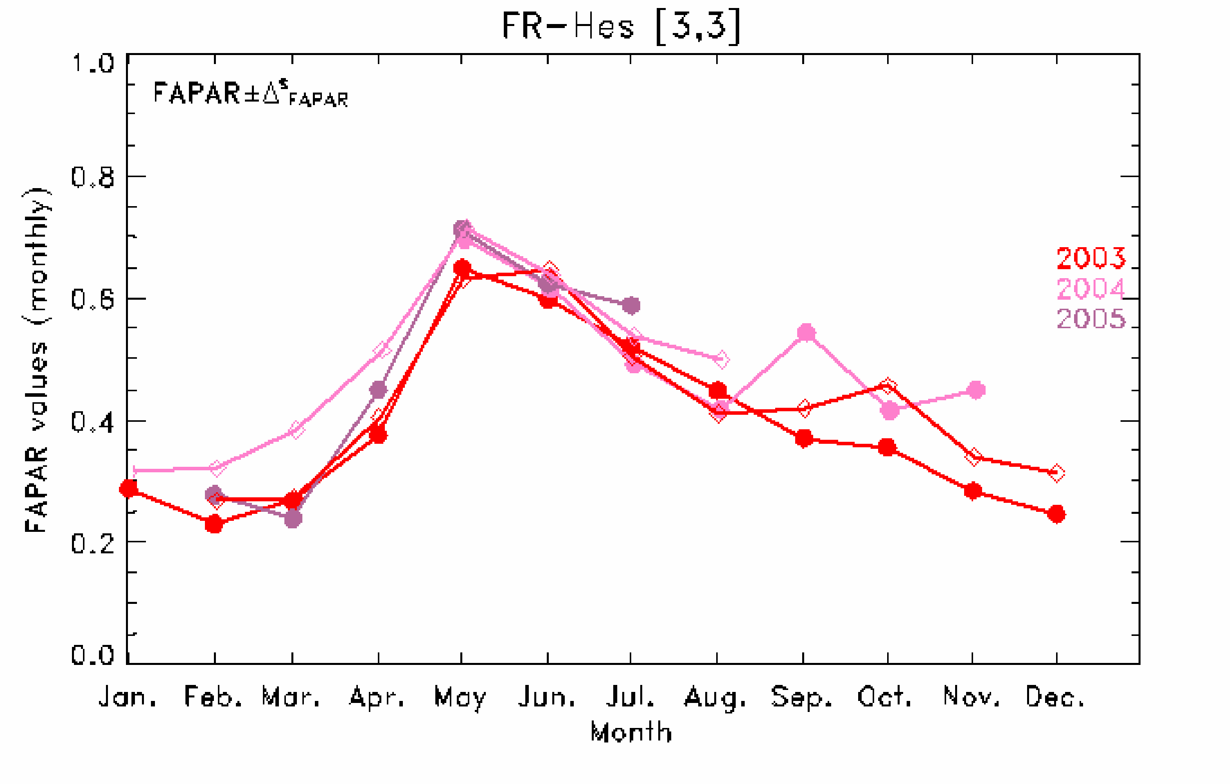

Figure 76**:** Time-series of monthly FAPAR are plotted over Hesse (FR) derived from MERIS (SeaWiFS) from 2003 to 2005 (Aug. 2004).

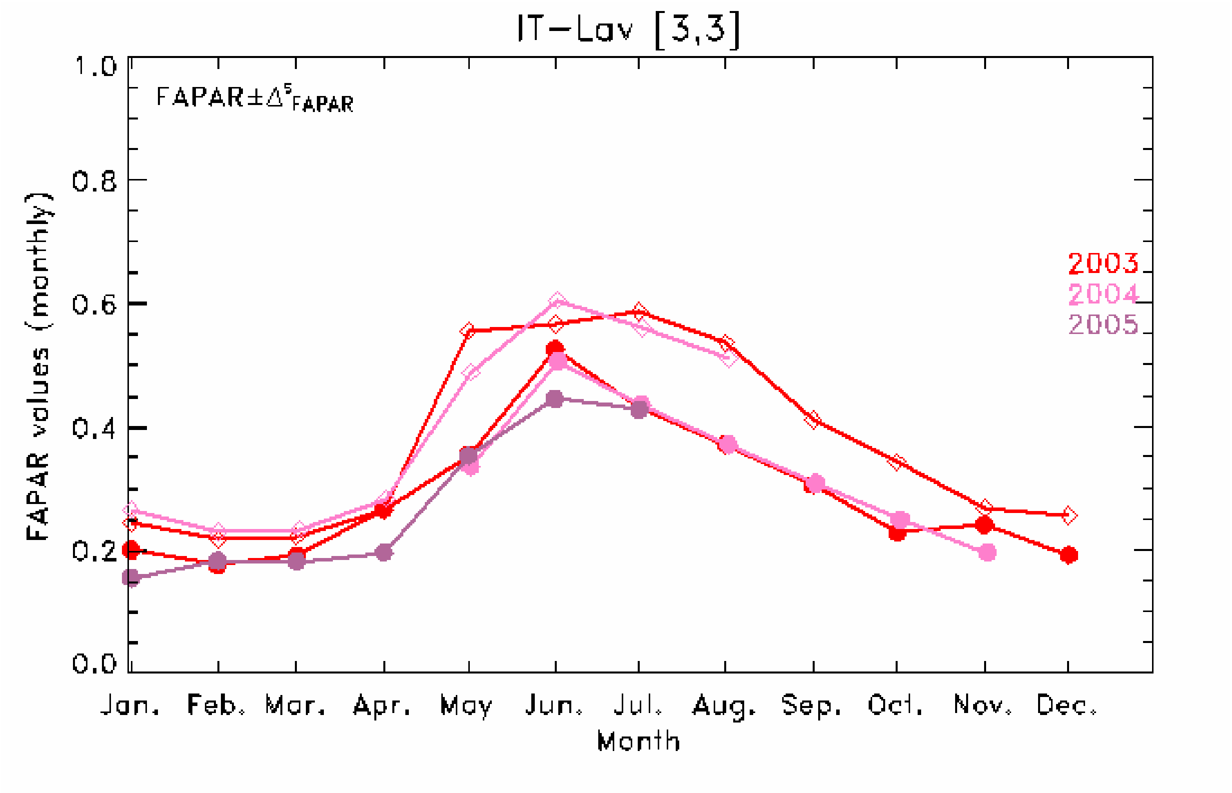

Figure 77**:** Time-series of monthly FAPAR are plotted over Lavarone (IT) derived from MERIS (SeaWiFS) from 2003 to 2005 (Aug. 2004).

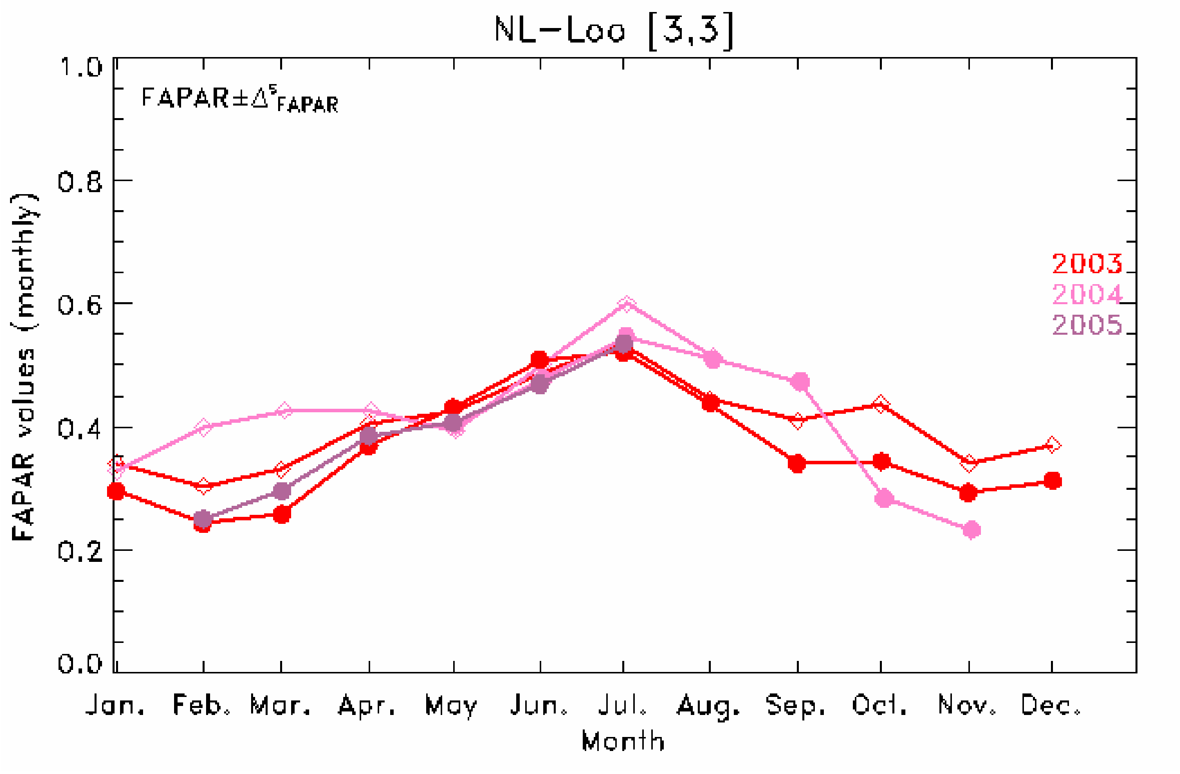

Figure 78**:** Time-series of monthly FAPAR are plotted over Loobos (NL) derived from MERIS (SeaWiFS) from 2003 to 2005 (Aug. 2004).

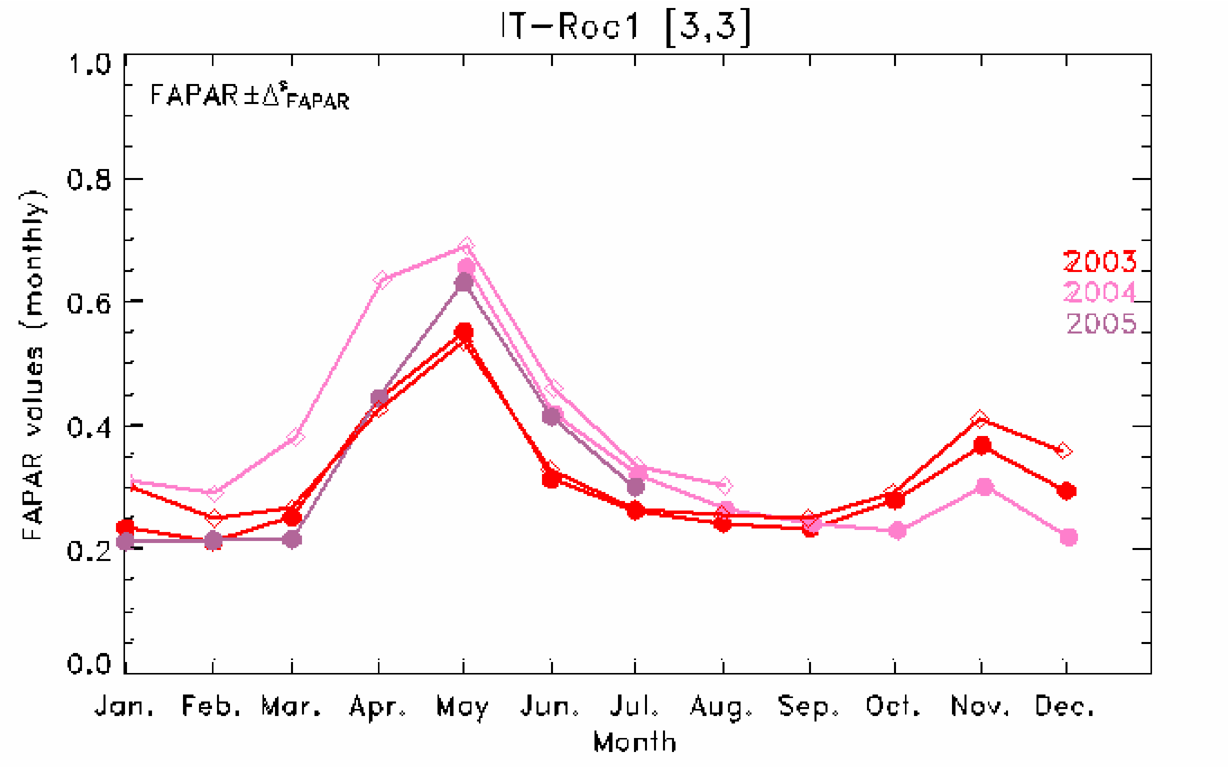

Figure 79: Time-series of monthly FAPAR are plotted over Roccampespani (IT) derived from MERIS (SeaWiFS) from 2003 to 2005 (Aug. 2004).

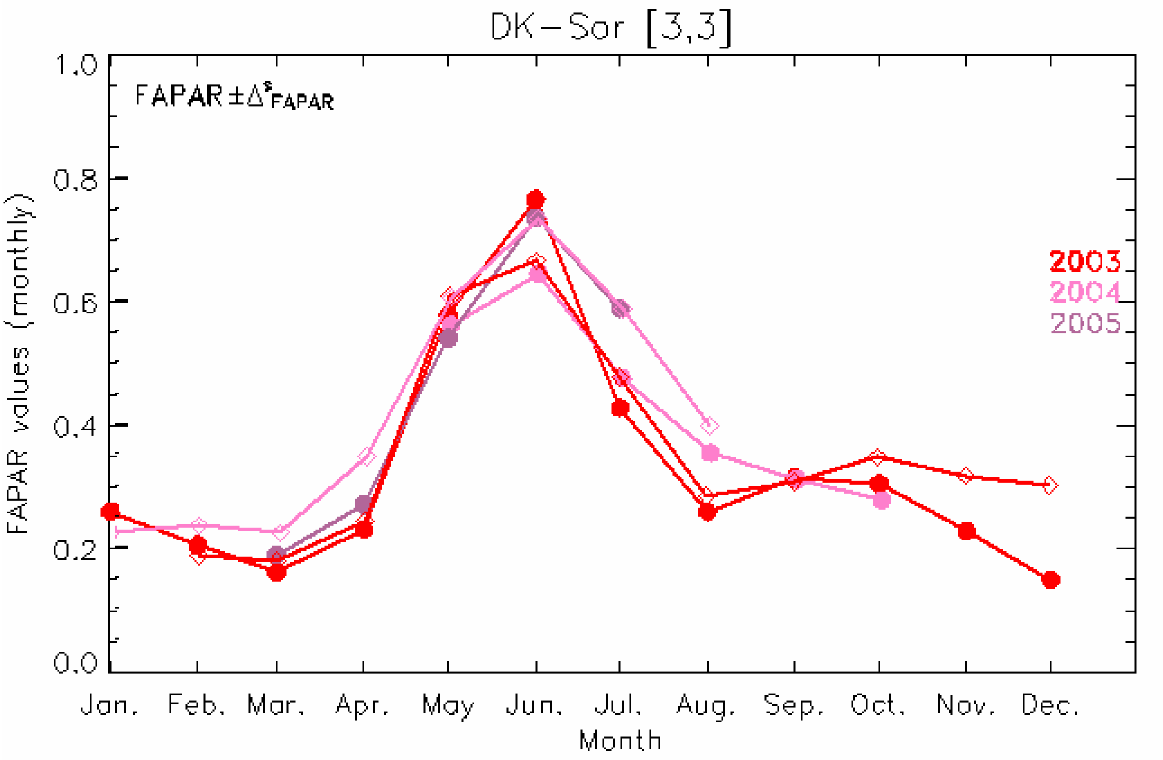

Figure 80: Time-series of monthly FAPAR are plotted over Soroe (DK) derived from MERIS (SeaWiFS) from 2003 to 2005 (Aug. 2004).

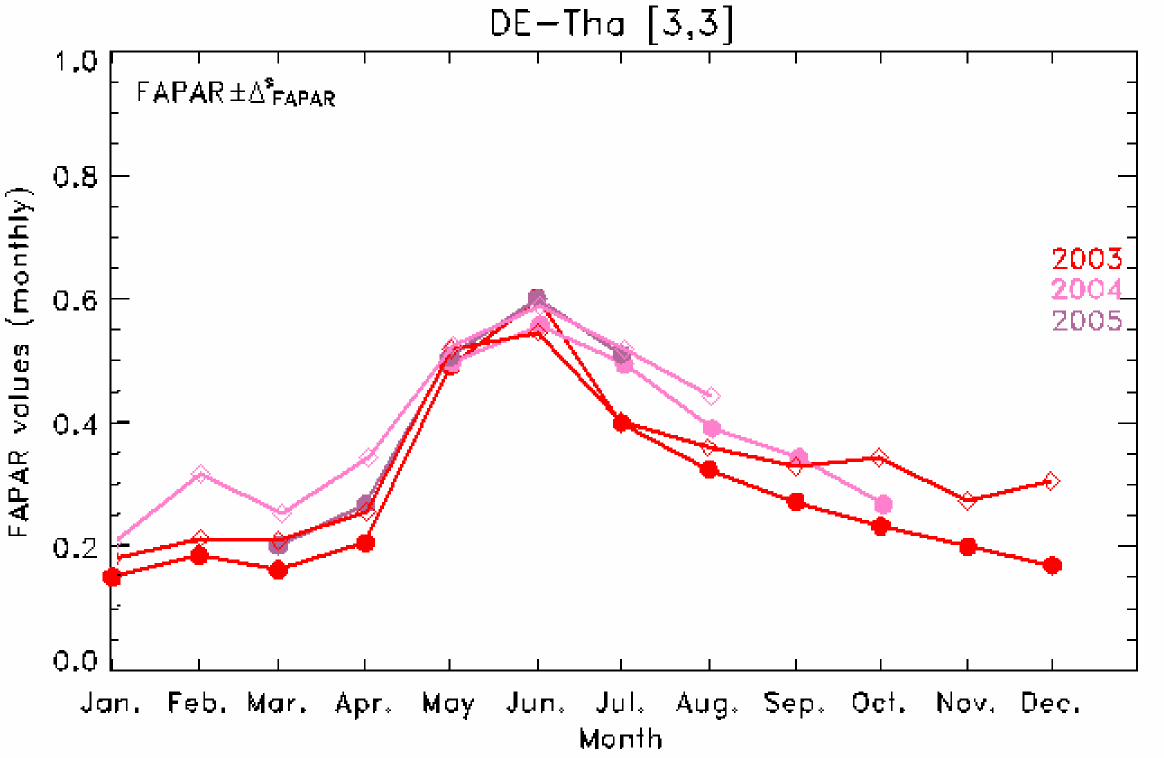

Figure 81: Time-series of monthly FAPAR are plotted over Tharandt (DE) derived from MERIS (SeaWiFS) from 2003 to

2005 (Aug. 2004).

18. Annex E: Remote sensing data

a. MERIS data

i. The daily MERIS Level 2 data at the reduce resolution have been initially provided by Brockmann Consult in the Space Oblique Mercator (SOM) projection in the PDS format.

The following files correspond to specific daily data which have been used in the comparison over common geographical regions listed in Table 7.

```
MER_RR_2PNACR20020507_085646_00000090X000_00408_00963_0000_STATION_271_0303_corr.N1.hdf
MER_RR_2PNACR20020619_094843_00000084X000_00501_01579_0000_AAOT_0303_corr.N1.hdf
MER_RR_2PNACR20020725_173748_00000084X000_00041_02099_0000_BOREAS_0303_corr.N1.hdf
MER_RR_2PNACR20020731_075157_00000087X000_00121_02179_0000_ISRAEL_0303_corr.N1.hdf
MER_RR_2PNACR20020816_092321_00000089X000_00351_02409_0000_STATION_114_0303_corr.N1.hdf
MER_RR_2PNACR20020821_100630_00000087X000_00423_02481_0000_GEESTHACHT_0303_corr.N1.hdf
MER_RR_2PNACR20020822_093511_00000089X000_00437_02495_0000_GEESTHACHT_0303_corr.N1.hdf
MER_RR_2PNACR20020903_100942_00000084X000_00108_02667_0000_OUAGADOUGOU_0303_corr.N1.hdf
MER_RR_2PNACR20021001_102041_00000089X000_00008_03068_0000_AERONET_0303_corr.N1.hdf
MER_RR_2PNACR20021213_102619_00000090X000_00051_04113_0000_AERONET_0303_corr.N1.hdf
MER_RR__2PQBCG20021227_180927_000003272012_00256_04318_0001_MARICOPA.N1.hdf
MER_RR__2PQBCG20021228_173815_000003292012_00270_04332_0001_MARICOPA.N1.hdf
MER_RR__2PQBCG20021231_174355_000003292012_00313_04375_0001_MARICOPA.N1.hdf
MER_RR__2PQBCG20030101_171242_000003322012_00327_04389_0001_JORNADA.N1.hdf
MER_RR__2PQBCG20030103_174935_000003292012_00356_04418_0001_JORDANA.N1.hdf
MER_RR__2PQBCG20030103_174935_000003292012_00356_04418_0001_JORNADA.N1.hdf
MER_RR__2PQBCG20030103_174935_000003292012_00356_04418_0001_MARICOPA.N1.hdf
MER_RR__2PQBCG20030208_185526_000002732013_00371_04934_0001_CASCADES.N1.hdf
MER_RR__2PQBCG20030208_185526_000002732013_00371_04934_0001_METOLIUS.N1.hdf
MER_RR__2PQBCG20030211_190107_000002732013_00414_04977_0001_CASCADES.N1.hdf
MER_RR__2PQBCG20030211_190107_000002732013_00414_04977_0001_METOLIUS.N1.hdf
MER_RR__2PQBCG20030406_172655_000003292015_00184_05749_0001_JORNADA.N1.hdf
MER_RR__2PQBCG20030409_172823_000002562015_00227_05792_0001_BOREASSSA.N1.hdf
MER_RR__2PQBCG20030409_173236_000003292015_00227_05792_0001_JORNADA.N1.hdf
MER_RR__2PQBCG20030410_170124_000003322015_00241_05806_0001_JORNADA.N1.hdf
MER_RR__2PQBCG20030413_170704_000003322015_00284_05849_0001_JORNADA.N1.hdf
```

ii. The MERIS Level 2 data over Europe for the entire year 2003 at the reduce resolution have been processed by Grid-On Demand service (ESRIN) using the executable code to remap data into rectangular grid at 1.2 km and the JRC-time composite to produce monthly composite. These data have been exploited to make the comparison with SeaWiFS products over the CarboEurope-IP sites (see Table 8) and the comparison over EU-25.

iii. The data for comparing the MGVI with the ground-estimation and other sensors FAPAR over EOS validation sites have been downloaded by using the MERCI system (http://brockmann-consult.de/merci/welcome.do), or have been delivered by Brockmann's consult.

b. SeaWiFS data

Both daily and monthly FAPAR SeaWiFS products came from the JRC-FAPAR database. The processing chain has been published in [15].

c. MODIS data

MODIS Level 1 data, i.e. TOA data have been downloaded from EOS Data Gateway at http://edg.larc.nasa.gov/. The MOD21km data include the three spectral bands of interest as well as the illumination and geometries conditions at about 1km of resolution.

The data in the following files have been used:

```
./STATION271/:
MOD02HKM.A2002127.1825.004.2002272033730.hdf
MOD02HKM.A2002127.1025.004.2002272015543.hdf
MOD02HKM.A2002127.1020.004.2002272014400.hdf
MOD02HKM.A2002127.0845.004.2002272021157.hdf

./STATION114/:
MOD021KM.A2002228.1045.003.2002239212053.hdf
MOD021KM.A2002228.0905.003.2002235015832.hdf


/METOLIUS/and /MARICOPA/:
MOD021KM.A2003003.1930.004.2003004035807.hdf
MOD021KM.A2003003.1925.004.2003004035739.hdf
MOD021KM.A2003003.1750.004.2003004034521.hdf
MOD021KM.A2003003.1745.004.2003004024834.hdf
MOD021KM.A2002365.1900.004.2003001034455.hdf
MOD021KM.A2002365.1855.004.2003001034437.hdf
MOD021KM.A2002365.1720.004.2003001013042.hdf
MOD021KM.A2002365.1715.004.2003001012412.hdf
MOD021KM.A2002362.2000.004.2002363073355.hdf



MOD021KM.A2003100.1830.004.2003101030317.hdf
MOD021KM.A2003100.1655.004.2003101002537.hdf
MOD021KM.A2003100.1650.004.2003101002536.hdf
MOD021KM.A2003099.1925.004.2003100034716.hdf
MOD021KM.A2003099.1920.004.2003100034400.hdf
MOD021KM.A2003099.1750.004.2003100063511.hdf
MOD021KM.A2003099.1745.004.2003100063500.hdf
MOD021KM.A2003099.1740.004.2003100063522.hdf
MOD021KM.A2003099.1615.004.2003100062126.hdf
MOD021KM.A2003099.1610.004.2003100071145.hdf
MOD021KM.A2003099.1605.004.2003100071028.hdf
MOD021KM.A2003096.1900.004.2003103130653.hdf
MOD021KM.A2003096.1855.004.2003103130703.hdf
MOD021KM.A2003096.1720.004.2003097023821.hdf
MOD021KM.A2003096.1715.004.2003097023802.hdf
MOD021KM.A2003003.1925.004.2003004035739.hdf
MOD021KM.A2003003.1750.004.2003004034521.hdf
MOD021KM.A2003003.1745.004.2003004024834.hdf
MOD021KM.A2003003.1615.004.2003004023206.hdf
MOD021KM.A2003003.1610.004.2003004015800.hdf
MOD021KM.A2003001.1805.004.2003002034347.hdf
MOD021KM.A2003001.1800.004.2003002034341.hdf
MOD021KM.A2003001.1625.004.2003002011047.hdf
MOD021KM.A2003001.1620.004.2003002011035.hdf

./ISRAEL/:
MOD02HKM.A2002212.0910.003.2002213021244.hdf
MOD021KM.A2002212.0910.004.2003216115840.hdf
```

```
MOD021KM.A2002127.1825.004.2002272033730.hdf
MOD021KM.A2002127.1025.004.2002272015543.hdf
MOD021KM.A2002127.1020.004.2002272014400.hdf
MOD021KM.A2002127.0845.004.2002272021157.hdf


./OUAGADOUGOU/:
MOD021KM.A2002246.1045.004.2003122210314.hdf
MOD021KM.A2002246.1040.004.2003122210312.hdf


MOD021KM.A2002362.1830.004.2002363070028.hdf
MOD021KM.A2002362.1825.004.2002363065750.hdf
MOD021KM.A2002362.1820.004.2002363063827.hdf
MOD021KM.A2002361.1925.004.2002362045819.hdf
MOD021KM.A2002361.1920.004.2002362045726.hdf
MOD021KM.A2002361.1915.004.2002362035557.hdf
MOD021KM.A2002361.1745.004.2002362032910.hdf
MOD021KM.A2002361.1740.004.2002362032650.hdf


./JORNADA/:
MOD021KM.A2003100.1835.004.2003101030354.hdf

MOD021KM.A2002212.0910.003.2002213021244.hdf

./GEESTHACHT.234/:
MOD021KM.A2002234.1010.004.2003225025401.hdf
MOD021KM.A2002234.0830.004.2003225002845.hdf

./GEESTHACHT.233/:
MOD021KM.A2002233.1105.004.2003224005637.hdf
MOD021KM.A2002233.0925.004.2003223230905.hdf

./CASCADES/:
MOD021KM.A2003042.1935.004.2003043035848.hdf
MOD021KM.A2003042.1930.004.2003043035831.hdf
MOD021KM.A2003042.1925.004.2003043035836.hdf
MOD021KM.A2003042.1755.004.2003043031601.hdf
MOD021KM.A2003042.1750.004.2003043031545.hdf
MOD021KM.A2003039.1900.004.2003040031931.hdf
MOD021KM.A2003039.1855.004.2003040031943.hdf

./BOREASSSA/:
MOD021KM.A2003099.1925.004.2003100034716.hdf
MOD021KM.A2003099.1920.004.2003100034400.hdf
MOD021KM.A2003099.1750.004.2003100063511.hdf
MOD021KM.A2003099.1745.004.2003100063500.hdf
MOD021KM.A2003099.1740.004.2003100063522.hdf
MOD021KM.A2003099.1615.004.2003100062126.hdf
MOD021KM.A2003099.1610.004.2003100071145.hdf
MOD021KM.A2003099.1605.004.2003100071028.hdf
```

```
./BOREAS/:
MOD021KM.A2002206.1935.004.2003219002240.hdf
MOD021KM.A2002206.1800.004.2003218230546.hdf
MOD021KM.A2002206.1755.004.2003218223037.hdf
MOD021KM.A2002206.1620.004.2003218213917.hdf
MOD021KM.A2002206.1615.004.2003218213856.hdf

./AERONET.347/:
MOD02HKM.A2002347.1230.004.2002353000136.hdf
MOD02HKM.A2002347.1055.004.2002347232658.hdf
MOD02HKM.A2002347.1050.004.2002347232745.hdf
MOD021KM.A2002347.1230.004.2002353000136.hdf
MOD021KM.A2002347.1055.004.2002347232658.hdf
MOD021KM.A2002347.1050.004.2002347232745.hdf
```

```
./AERONET.274/:
MOD02HKM.A2002274.1100.004.2003117141522.hdf
MOD02HKM.A2002274.1055.004.2003117141513.hdf
MOD02HKM.A2002274.0920.004.2003117120957.hdf
MOD021KM.A2002274.1100.004.2003117141522.hdf
MOD021KM.A2002274.1055.004.2003117141513.hdf
MOD021KM.A2002274.0920.004.2003117120957.hdf

./AAOT/:
MOD02HKM.A2002170.1010.004.2003116181604.hdf
MOD02HKM.A2002170.1005.004.2003116181800.hdf
MOD021KM.A2002170.1010.004.2003116181604.hdf
MOD021KM.A2002170.1005.004.2003116181800.hdf
```

The data used for the EOS validation site concern one year of data and they have been saved on DVDs (available on demand).

d. MISR data

The data used for the validation site Bonville concern one year of data and they have been saved on DVDs (available on demand).

e. MOS data

MOS Level 1B data, i.e. TOA radiances have been downloaded from DLR portal at http://eoweb.dlr.de:8080/servlets/template/welcome/entryPage.vm.

The MOS data include the three spectral bands of interest as well as the illumination and geometries conditions at about 500 m of resolution.

The data over some EOS sites have been used and the files are:

Bonville (i.e. Agro):

```
LEV00275_IP3B13.228
LEV00276_IP3B11.257
LEV00276_IP3B12.257
LEV00276_IP3B13.065
LEV00276_IP3B13.137
LEV00276_IP3B13.281
LEV00276_IP3B13.305
LEV00276_IP3B14.089
LEV00276_IP3B14.113
LEV00276_IP3B14.353
LEV00277_IP3B12.286
LEV00277_IP3B12.358
LEV00277_IP3B13.022
LEV00277_IP3B13.238
LEV00277_IP3B13.310
LEV00277_IP3B13.358
LEV00277_IP3B14.022
LEV00277_IP3B14.118
LEV00277_IP3B15.094
LEV00278_IP3B13.051
LEV00278_IP3B13.243
LEV00278_IP3B14.003
LEV00278_IP3B14.027
LEV00278_IP3B14.051
LEV00278_IP3B14.075
LEV00278_IP3B14.123
LEV00278_IP3B14.147
LEV00278_IP3B14.219
LEV00278_IP3B14.243
LEV00278_IP3B14.291
LEV00278_IP3B14.315
LEV00278_IP3B15.003
LEV00278_IP3B15.147
LEV00278_IP3B15.315
```

Dahra:

```
LEV00010_IP3B36.032
LEV00010_IP3B36.128
LEV00010_IP3B37.248
LEV00011_IP3B36.037
LEV00011_IP3B36.061
LEV00011_IP3B37.061
LEV00011_IP3B37.277
LEV00011_IP3B38.133
LEV00011_IP3B38.277
LEV00012_IP3B35.258
LEV00012_IP3B36.018
LEV00012_IP3B37.018
LEV00012_IP3B37.090
LEV00012_IP3B37.114
LEV00012_IP3B37.282
LEV00012_IP3B38.090
LEV00012_IP3B38.282
```

Braschaat:

```
LEV00018_IP3B15.231
LEV00018_IP3B15.279
LEV00018_IP3B17.024
LEV00018_IP3B17.048
LEV00018_IP3B17.096
LEV00018_IP3B17.255
LEV00018_IP3B17.351
LEV00018_IP3B36.120
LEV00019_IP3B12.029
LEV00019_IP3B12.236
LEV00019_IP3B13.029
LEV00019_IP3B13.284
LEV00019_IP3B14.149
LEV00019_IP3B15.077
LEV00019_IP3B15.149
LEV00019_IP3B15.260
LEV00019_IP3B15.356
LEV00019_IP3B16.005
```

```
LEV00019_IP3B16.077
LEV00019_IP3B16.260
LEV00019_IP3B17.101
LEV00019_IP3B17.125
LEV00020_IP3B13.241
LEV00020_IP3B14.241
LEV00020_IP3B15.082
LEV00020_IP3B15.154
LEV00020_IP3B15.265
LEV00020_IP3B16.082
LEV00020_IP3B16.265
LEV00020_IP3B16.289
LEV00020_IP3B16.337
LEV00020_IP3B16.361
LEV00020_IP3B17.010
LEV00020_IP3B17.034
LEV00020_IP3B17.106
LEV00020_IP3B17.289
LEV00020_IP3B18.010
LEV00020_IP3B18.106
LEV00021_IP3B15.159
LEV00021_IP3B15.270
LEV00021_IP3B16.015
LEV00021_IP3B16.039
LEV00021_IP3B16.087
LEV00021_IP3B17.111
LEV00021_IP3B17.246
LEV00021_IP3B39.135
```

Harv:

```
LEV00290_IP3B10.172
LEV00290_IP3B11.004
LEV00290_IP3B12.028
LEV00290_IP3B12.052
LEV00290_IP3B12.220
LEV00290_IP3B12.268
LEV00290_IP3B9.148
LEV00291_IP3B10.177
LEV00291_IP3B10.273
LEV00291_IP3B11.009
LEV00291_IP3B11.033
LEV00291_IP3B11.105
LEV00291_IP3B11.177
LEV00291_IP3B11.225
LEV00291_IP3B11.249
LEV00291_IP3B11.273
LEV00291_IP3B12.225
LEV00291_IP3B12.249
LEV00291_IP3B9.297
LEV00292_IP3B10.134
LEV00292_IP3B10.254
LEV00292_IP3B11.014
LEV00292_IP3B11.038
LEV00292_IP3B11.086
LEV00292_IP3B11.110
LEV00292_IP3B11.182
LEV00292_IP3B11.230
LEV00292_IP3B11.278
LEV00292_IP3B12.038
LEV00293_IP3B10.259
LEV00293_IP3B10.283
LEV00293_IP3B11.067
LEV00293_IP3B11.139
LEV00293_IP3B12.187
LEV00293_IP3B12.307
```

Konz:

```
./2000:
LEV00268_IP3B12.049
LEV00268_IP3B13.073
LEV00268_IP3B13.145
LEV00268_IP3B13.217
LEV00268_IP3B13.241
LEV00268_IP3B13.313
LEV00268_IP3B13.337
LEV00268_IP3B14.097
LEV00269_IP3B13.054
LEV00269_IP3B13.078
LEV00269_IP3B13.270
LEV00269_IP3B14.006
LEV00269_IP3B14.054
LEV00269_IP3B14.102
LEV00269_IP3B14.126
LEV00269_IP3B14.150
LEV00269_IP3B14.222
LEV00269_IP3B14.294
LEV00269_IP3B14.366
LEV00269_IP3B15.030
LEV00269_IP3B15.246
LEV00269_IP3B15.318
LEV00269_IP3B15.366
LEV00270_IP3B13.011
LEV00270_IP3B13.035
LEV00270_IP3B13.059
LEV00270_IP3B13.083
LEV00270_IP3B13.131
LEV00270_IP3B13.275
LEV00270_IP3B13.323
LEV00270_IP3B13.347
LEV00270_IP3B14.035
LEV00270_IP3B14.227
LEV00270_IP3B14.251
LEV00270_IP3B15.227

./2001:
LEV00268_IP3B12.139
LEV00268_IP3B13.019
LEV00268_IP3B13.259
LEV00268_IP3B13.331
LEV00268_IP3B14.187
LEV00268_IP3B14.211
LEV00268_IP3B14.307
LEV00268_IP3B14.355
LEV00269_IP3B12.336
LEV00269_IP3B13.072
LEV00269_IP3B13.144
LEV00269_IP3B13.168
LEV00269_IP3B13.264
LEV00269_IP3B13.312
LEV00269_IP3B13.336
LEV00269_IP3B13.360
LEV00269_IP3B14.024
LEV00269_IP3B14.048
LEV00269_IP3B14.120
LEV00269_IP3B14.216
LEV00269_IP3B15.096
LEV00270_IP3B13.005
LEV00270_IP3B13.029
LEV00270_IP3B14.101
LEV00270_IP3B14.125
LEV00270_IP3B14.149
LEV00270_IP3B14.173
LEV00270_IP3B14.245
LEV00270_IP3B14.269
LEV00270_IP3B14.317
LEV00270_IP3B14.341
LEV00270_IP3B14.365
LEV00270_IP3B15.149
LEV00270_IP3B15.197
LEV00270_IP3B15.317
LEV00271_IP3B15.346

./2002:
```

LEV00268_IP3B12.158
LEV00268_IP3B13.038
LEV00268_IP3B13.230
LEV00268_IP3B13.302
LEV00269_IP3B12.211
LEV00269_IP3B12.259
LEV00269_IP3B13.067
LEV00269_IP3B13.115
LEV00269_IP3B13.139
LEV00269_IP3B13.163
LEV00269_IP3B13.235
LEV00269_IP3B13.259
LEV00269_IP3B14.019
LEV00269_IP3B14.091
LEV00269_IP3B14.163
LEV00269_IP3B14.187
LEV00269_IP3B15.043
LEV00270_IP3B12.120
LEV00270_IP3B12.216
LEV00270_IP3B13.048
LEV00270_IP3B13.120
LEV00270_IP3B13.216
LEV00270_IP3B13.240
LEV00270_IP3B13.288
LEV00270_IP3B14.072
LEV00270_IP3B14.096
LEV00270_IP3B15.096
LEV00271_IP3B14.029
LEV00271_IP3B14.053
LEV00271_IP3B14.296

EUROPEAN COMMISSION
DIRECTORATE-GENERAL
Joint Research Centre

The mission of the JRC is to provide customer-driven scientific and technical support for the conception, development, implementation and monitoring of EU policies. As a service of the European Commission, the JRC functions as a reference centre of science and technology for the Union. Close to the policy-making process, it serves the common interest of the Member States, while being independent of special interests, whether private or national.